山形大学

YAMAGATA UNIVERSITY

Doctoral Thesis

First measurement of transverse spin asymmetry on the polarised Drell-Yan

偏極ドレル・ヤン過程による横スピン非対称度の測定

Author:
Genki Nukazuka

Supervisor:
Dr. Takahiro Iwata

A thesis submitted in fulfilment of the requirements
for the degree of Doctor of Philosophy

in the

Graduate School of Science and Engineering (Science)
Yamagata University

December, 2017

Abstract

Since the proposal of and the discovery of the quark, the structure of the nucleon at the level of the parton has been studied both theoretically and experimentally based on the framework of Quantum ChromoDynamics (QCD), but many questions are not yet solved. One of the issues is the spin structure of the nucleon. The nucleon spin $1/2$ should be described with the following formula: $1/2 = \Delta\Sigma/2 + \Delta G + L$, where $\Delta\Sigma$, ΔG, L are contributions of quark spin, gluon spin, and orbital angular momentum of quarks and gluons, respectively. In naïve models, $\Delta\Sigma$ is the only contribution. However, the report by EMC in 1998, raises the "Proton spin crisis", $\Delta\Sigma$ was consistent with zero. Many theoretical and experimental investigations have been carried out on this crisis, but a perfect explanation is not yet obtained.

The structure of the nucleon at leading twist can be described with eight parton distribution functions (PDFs). Five of them which survive after integration over a transverse momentum of the parton k_T are called transverse momentum dependent (TMD) PDFs. Sivers distribution, which is one of the TMD-PDFs, describes a correlation between k_T and the transverse component of the nucleon's spin. If a value of the Sivers distribution is 0, this suggests that an orbital angular momentum of the parton does not exist. Hence measurement of the Sivers distribution relates with an existence of L. Since it is a naïve time reversal odd function, the sign obtained via Drell-Yan (DY) process and one via Semi-Inclusive Deep Inelastic Scattering (SIDIS) are expected to be opposite. Confirmation of this prediction is a crucial test for the TMD approach in QCD. However, the measurement via the DY process has not been performed due to technical difficulties.

COMPASS (Common Muon Proton Apparatus for Structure and Spectroscopy) collaboration, which consists of more than 200 physicists from 13 countries, researches the nucleon structure and the hadron spectroscopy with high-intensity muon and hadron beams. The beams provided by the Super Proton Synchrotron in CERN and a fixed target were utilised for the study. In this thesis, asymmetries of a $\mu^+\mu^-$ pair (dimuon) related to azimuth and zenith angles are extracted from measurement of a polarised DY process, $\pi^- + \mathrm{p}^\uparrow \rightarrow \mu^+ + \mu^- + X$. The polarised DY process is caused with a pion beam with a momentum of $190\,\mathrm{GeV}/c$ and solid ammonia as a transversely polarised proton target. Since the asymmetries are understood as a convolution of (TMD-) PDFs of the target nucleon and (TMD-)PDF of the beam pion, TMD-PDF of a nucleon can be accessed from the extracted asymmetries. The COMPASS spectrometer measures angular distribution of the dimuon emitted from the process. An optimisation of the polarised target and introductions of a hadron absorber, a new station of a drift chamber and a vertex detector based on a scintillation fibre tracker were applied for the measurement.

Six-month data taking was performed in 2016, and about $750\,\mathrm{TB}$ of data was collected. Reconstruction of particle tracks and interaction points was performed with the data. After some event selections, the asymmetries were extracted using the Extended Unbinned Maximum Likelihood method as a function of a kinematic variable, Bjorken x of the target particle and the beam pion, Feynman's x, a transverse momentum of a virtual photon and an invariant mass of the dimuon. The asymmetries integrated over all the kinematic variables were also calculated. The value of the asymmetry related to the Sivers distribution of the target nucleon was about 0.06. The result is compatible with theoretical predictions assuming the sign reversal of the Sivers distribution.

概要

　クォークの提唱・実験的発見以来，核子のパートンレベルでの内部構造は QCD 非摂動領域の問題として理論・実験の両面から精力的に研究されているが，多くの未解決問題を残している。なかでも核子スピンの成り立ち ── すなわち核子のスピン構造: $1/2 = \Delta\Sigma/2 + \Delta G + L$ におけるクォークスピン寄与 $\Delta\Sigma$，グルーオンスピン寄与 ΔG，クォーク・グルーオンの軌道回転の寄与 L ── は最も基本的な問題のひとつだが，1988 年の EMC による報告に端を発した「陽子スピンの危機 (Proton spin crisis)」から 30 年余り経過した現在でも完全な理解には至っていない。

　核子の構造は Leading-twist において 8 つのパートン分布関数 (PDFs) で記述される。このうち 5 つはパートンの横方向運動量 k_T に依存する関数 (TMD-PDFs) である。Sivers 関数は k_T と核子スピンの横方向成分の相関を記述する TMD-PDFs のひとつであり，値の有無はパートンの軌道角運動の存在に関わる。ゆえに Sivers 関数の測定は L の有無につながる。また，Sivers 関数は時間反転奇であるため，準包括的深非弾性散乱とドレル・ヤン (DY) 過程で測定した Sivers 関数の符号は反転すると理論的に予言されている。核子構造を TMD-PDFs で理解する理論的な枠組みはこの予言の確認なくして確立されないが，技術的な難しさのため DY 過程による Sivers 関数の測定は未だ行われていなかった。

　COMPASS (Common Muon Proton Apparatus for Structure and Spectroscopy) は 13 カ国から 200 人以上の研究者が参加する国際共同プロジェクトで，実験による核子構造とハドロンスペクトロスコピーの研究を行っている。CERN の Super Proton Synchrotron から提供されるミューオン・ハドロンビームと固定標的を使用し，全長 60 m のスペクトロメータで散乱・生成粒子をとらえる。本論文では運動量 $190\,\mathrm{GeV}/c$ の π^- ビームと，ビームに対して横偏極した陽子標的による偏極 DY 過程 $\pi^- + \mathrm{p}^\uparrow \to \mu^+ + \mu^- + X'$ による $\mu^+\mu^-$ 粒子対 (dimuon) 角度分布を COMPASS スペクトロメータ測定し，方位角・天頂角に関する非対称度を求めた。この非対称度は標的核子の (TMD-) PDF とビーム π^- の (TMD-) PDF の畳込み積分に比例するという解釈が与えられており，核子の TMD-PDF の情報が得られる。スペクトロメータは基本的に従来と同じだが，本測定のため偏極標的の最適化を行い，シンチレーションファイバートラッカの vertex detector，新ドリフトチェンバー，ハドロンアブソーバを新たに導入した。

　2016 年に 6 ヶ月間のデータ収集を行い約 $750\,\mathrm{TB}$ のデータを収集した。このデータから粒子の飛跡，反応点の再構成を行い，偏極 DY 過程による dimuon 事象を選択した。このデータに対して Extended Unbinned Maximum Likelihood 法を用いて非対称度を抽出した。非対称度は標的核子・ビーム粒子の Bjorken x，Feynman x，仮想光子の横運動量，dimuon 不変質量いずれかの変数に対して得た。これらの変数を全て積分したときの非対称度も求めた。核子の Sivers 関数に関わる非対称度の値は約 0.06 で，統計誤差と測定誤差を考慮すると標準偏差の範囲で 0 と矛盾しない結果が得られた。これは符号反転を適用した理論予測と誤差の範囲で一致するものであった。

Contents

List of Abbreviations

AGS	**A**lternating **G**radient **S**ynchrotron
ATLAS	**A T**oroidal **LHC A**pparatuA Toroidal LHC ApparatuS
BNL	**B**rookhaven **N**ational **L**aboratory
CDF	The **C**ollider **D**etector at **F**ermilab
CERN	**C**onseil **E**uropéen pour la **R**echerche **N**ucléaire
CHEOPS	**CH**arm **E**xperiment with **O**mni-Purpose **S**etup
COMPASS	**C**ommon **M**uon and **P**roton **A**pparatus for **S**tructure and **S**pectroscopy
CMS	The **C**ompact **M**uon **S**olenoid
EMC	**E**uropean **M**uon **C**ollaboration
FNAL	**F**ermi **N**ational **A**ccelerator **L**aboratory
HMC	**H**adron **M**uon **C**ollaboration
LHC	**L**arge **H**adron **C**ollider
NMC	**N**ew **M**uon **C**ollaboration
PS	**P**roton **S**ynchrotron
RHIC	**R**elativistic **H**eavy **I**on **C**ollider
SLAC	**S**tanford **L**inear **A**ccelerator **C**enter
SMC	**S**pim **M**uon **C**ollaboration
SPS	**S**uper **P**roton **S**ynchrotron
TGEANT	**T**otal **G**eometry **AN**d **T**racking

両親に捧ぐ

Chapter 1

Introduction

According to the Quantum ChromoDynamics (QCD) factorisation [1], hadron interaction at high energy can be divided into a "hard" and a "soft" parts. The hard part describes interaction at a short distance while the soft part describes interaction at a long distance expressed as a distribution of partons in the hadron and a fragmentation of a parton into the hadron. Thanks to the asymptotic freedom [2, 3], the hard part can be calculated perturbatively while the parton distribution and the fragmentation need to be determined to reconstruct experimental results. A cross-section of an inclusive process at high energy can be expanded with a power series of (M/Q), where M is a mass of a hadron and Q is a momentum transfer in the process. A contribution by $(M/Q)^{t-2}$ is called a contribution by "twist-t". In a high energy process with large Q ($Q \gg M$), the twist-two, which is called the leading-twist, is a dominant contribution.

To describe the nucleon structure at the leading-twist, eight parton distribution functions (PDFs) are needed. Three of them, the number density distribution f_1, the helicity distribution g_{1L}, and the transversity distribution h_1 survives after integration over an intrinsic transverse momentum of a parton $\mathbf{k_T}$. The remains, the Sivers distribution $f_{1T}^\perp$, the Boer-Mulders distribution $h_1^\perp$, the pretzelosity distribution $h_{1T}^\perp$, the worm gear distributions $h_{1L}^\perp$, and $g_{1T}^\perp$ are called transverse momentum dependent parton distribution functions (TMD-PDFs).

In this thesis, a study of the TMD-PDFs is carried out through a Drell-Yan (DY) process with a pion beam and a transversely polarised proton target at COMPASS: $\pi^- + \mathrm{p}^\uparrow \rightarrow \gamma^* + X \rightarrow \mu^- + \mu^+ + X$. Here, γ^* is a virtual photon and the superscript $\uparrow$ indicates a transverse polarisation, and X corresponds to many particles not detected. Despite many experiments for the TMD-PDFs via inelastic scattering in the past, the pion-induced polarised DY measurement can provide a crucial impact on the TMD approach for the structure of the nucleon. This theoretical motivation and background are introduced in Chapter 2 along with an overview of experiments. Chapter 3 offers a setup of the COMPASS spectrometer for the polarised DY measurement. A vital system for the measurement, a polarised target (PT), is introduced in Chapter 4, and results of the operation of the PT are discussed in the chapter. An analysis of the data and the results are shown in Chapter 5. Finally, Chapter 6 covers the conclusion.

Chapter 2

Overview of theory and experiments

Deep inelastic scattering (DIS) $\ell + N \to \ell' + X$ measurements take an important role in a study of the structure of the nucleon. Here, ℓ and ℓ' are beam and scattered leptons, N represents a nucleon target, and X indicates particles not detected. Structure functions can be measured via DIS measurement. In the QCD-quark-parton model [4, 5], the structure functions can be decomposed into a parton distribution function (PDF). Similarly to the PDF (will be called a number density distribution), a longitudinal or a transversal spin-dependent parton distribution describes spin-dependent structure function.

To investigate the spin-dependent nucleon structure, measurements of Semi-Inclusive DIS (SIDIS) process $\ell + N \to \ell' + h' + X$ with a longitudinally or transversely polarised nucleon had been performed, where h' is a hadron in the final state to be detected and often called the leading hadron. At the leading-twist, eight PDFs are needed to describe the structure of a nucleon. For the study of them, COMPASS measured the DY process $q + \bar{q} \to \ell + \bar{\ell}$ with negatively charged pions and a transversely polarised target, called the pion-induced polarised DY, where q represents a quark.

In this chapter, theoretical and experimental background for the pion-induced polarised DY are described.

2.1 Structure of the nucleon

Investigation of internal structure of the nucleon started in the 1960s at SLAC. Measurements of the form factors via elastic scattering of an electron off a nucleon gave information on charge and magnetic moment distributions of the nucleon. A measurement of DIS process shown in Fig. 2.1 enables us to study the parton-level structure of the nucleon. Before coming to the details, we define kinematic variables as follows:

- k, k': four-momentum of the incident and the scattered lepton

- E, E': incident and scattered lepton energy in the nucleon rest frame

- M: mass of the nucleon

- $q = k - k'$: momentum transfer from the incident lepton to the nucleon

- $Q^2 = -q^2 = -(k - k')^2$: photon virtuality

- $\nu = E - E'$: energy transfer from the incident lepton to the nucleon in the nucleon rest frame

- $x = \frac{Q^2}{2Pq} = \frac{Q^2}{2M\nu}$: a scaling variable so-called Bjorken x

- θ: a polar angle between a direction of the scattered lepton and the beam axis
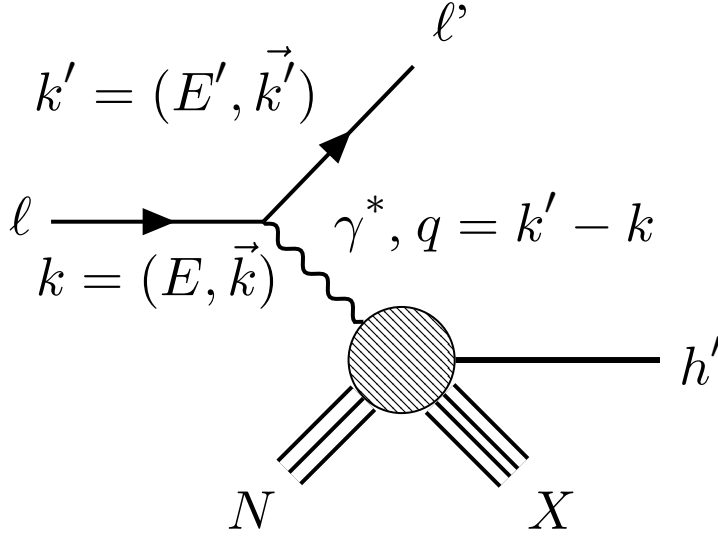
- Ω: a solid angle in which the scattered lepton is.

Figure 2.1: Feynman diagram of DIS. The N and X mean a target nucleon and many particles not detected, respectively. A scattered lepton ℓ' and a hadron h' in the final state are detected in the SIDIS process while only the scattered lepton ℓ' is detected in DIS.

The incoming lepton ℓ is scattered with the Bjorken variable x by a quark in the nucleon target N via a virtual photon γ^*. The Bjorken variable x in the QCD-parton model means a fraction of the parton's four-momentum to the parent hadron's four-momentum. The target nucleon is destroyed into many particles written as X. A differential cross-section of DIS for the scattered lepton in the solid angle Ω with energy E' is written as:

$$\frac{d^2\sigma}{d\Omega dE'} = \sigma_{\text{Mott}} \left[W_2(\nu, Q^2) + 2W_1(\nu, Q^2) \tan^2 \frac{\theta}{2} \right], \tag{2.1}$$

where σ_{Mott} is the cross-section of the Mott scattering, and W_1 and W_2 are the structure functions. By introducing the Bjorken variable x, the structure functions W_1 and W_2 can be described by the dimensionless structure functions F_1 and F_2 as follows:

$$F_1(x, Q^2) = Mc^2 W_1(\nu, Q^2)$$
$$F_2(x, Q^2) = \nu W_2(\nu, Q^2) \tag{2.2}$$

As a result of DIS experiments [6], a dependency of the cross-section of DIS on Q^2 was found to be very weak. It supports the Bjorken scaling [7] at the scaling limit ($Q^2 \to$ inf, $\nu \to$ inf and x fixed) and suggests that the nucleon consists of point-like particles, known as a parton. Furthermore, many experiments of DIS revealed a validation of the Callan-Gross relation [8]

$$F_2 = 2xF_1. \tag{2.3}$$

This suggests that the spin of the parton is 1/2. Fig. 2.2 shows the proton structure function F_2^p as a function of Q^2 available until 2016. As it is seen, the Bjorken scaling is slightly violated at very low x and high x. However a Q^2 evolution equation based on perturbative quantum chromodynamics (pQCD) [9–12] successfully explained it, and dependence of the structure function on $\ln(Q^2)$.
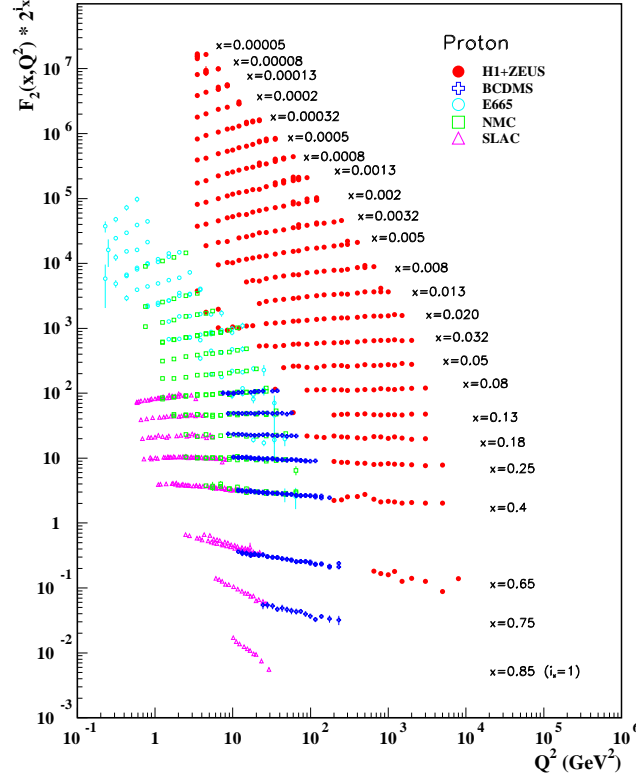
Figure 2.2: The proton structure function F_2^p as a function of Q^2 in bins of fixed x [13]. The data points are multiplied by 2^{i_x} for the purpose of plotting, where i_x is the number of the x bin, ranging from $i_x = 1$ ($x = 0.85$) to $i_x = 24$ ($x = 0.00005$).

In QCD-quark-parton model, the nucleon is composed of incoherent point-like particles, parton.

The structure functions are decomposed into the number density distribution $f_{1,q}(x)$, where the subscription q corresponds to a flavour of the parton. Here, the subscription 1 means that the PDF is introduced at the leading-twist in pQCD. For example, $f_{1,q}(x)dx$ is an expected number of a quark with flavour q and in a range of a momentum fraction from x to $x + dx$ in the nucleon. The dimensionless structure function $F_1(x)$ is described with the number density distribution:

$$F_1(x) = \frac{1}{2} \cdot \sum_q e_q^2 f_{1,q}(x), \tag{2.4}$$

where e_q is a charge of the parton and the flavour q is usually u, $\overline{\text{u}}$, d, $\overline{\text{d}}$, s, and $\overline{\text{s}}$. Theoretical extraction of the number density from experimental data has been performed. Fig. 2.3 shows the number density for each quark and gluon as a function of the x with $Q^2 = 10$ or 10^4 GeV^2.

2.1.1 Spin structure of nucleon

The nucleon spin 1/2 is decomposed into partons' contributions as follows [15]:

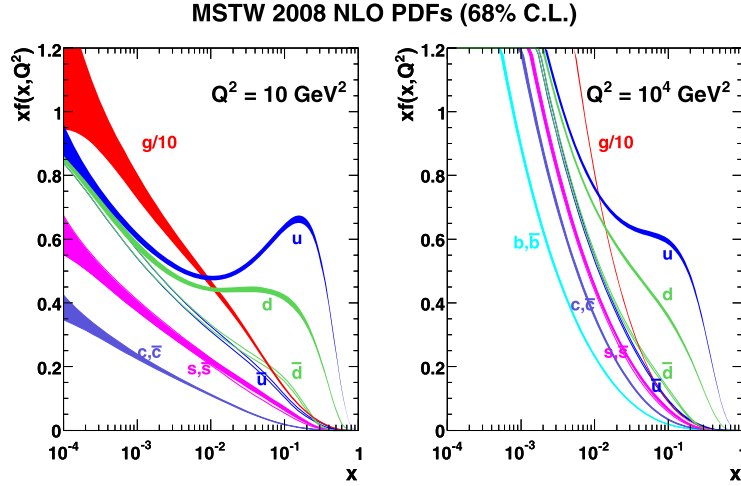$$\frac{1}{2} = \frac{1}{2}\Delta\Sigma + \Delta G + L, \tag{2.5}$$

Figure 2.3: PDF of proton as a function of x with fixed Q^2 of $10\,\mathrm{GeV}^2$ and $1000\,\mathrm{GeV}^2$. Plots were made with the MSTW2008nlo68cl dataset [14]. The gluon PDF is scaled by $1/10$.

where $\Delta\Sigma$, ΔG, and L are contributions of quark spin, gluon spin, and orbital angular momentum of partons, respectively. The quark spin contribution is decomposed into each flavour:

$$\Delta\Sigma = \sum_q \Delta f_{1,q}. \tag{2.6}$$

Usually, u, $\bar{\mathrm{u}}$, d, $\bar{\mathrm{d}}$, s, and $\bar{\mathrm{s}}$ are considered. Both contributions of the quark and gluon spin to the nucleon spin are given by the lowest moment of the longitudinal spin-dependent PDF, so-called the helicity distribution, in other words, an integration of the helicity distribution over the Bjorken x:

$$\Delta f_{1,q} = \int_0^1 dx\; g_{1L,q}(x)$$
$$\Delta G = \int_0^1 dx\; g_{1L,gluon}(x), \tag{2.7}$$

where g_{1L} is the helicity distribution of a parton of flavour q with a momentum fraction x in a longitudinally polarised nucleon [1]. In the case of gluon, it is written as $g_{1L,gluon}$. The notation L indicates a longitudinal polarisation of the nucleon. Here, the longitudinal direction is a direction of its motion while a transverse direction is perpendicular to its motion. The helicity distribution can be understood as a probability to find the number of longitudinally polarised partons in a longitudinally polarised nucleon:

$$g_{1L,q}(x) = \sum_q f_{1,q}^{\leftarrow}(x) - f_{1,q}^{\rightarrow}(x)$$

where $f_{1,q}^{\leftarrow}$, and $f_{1,q}^{\rightarrow}$ are the parton distribution function with longitudinal spin parallel or anti-parallel to the longitudinally polarised nucleon.

Analogous to the number density distribution, the helicity distributions are extracted in measurements of spin-dependent structure functions. E80 and E130 experiments at SLAC

---

[1]The helicity distribution is sometimes described as g_1, Δf, or Δq while the spin-dependent structure function is also written as g_1. In this thesis, so called Amsterdam notations is employed [16].
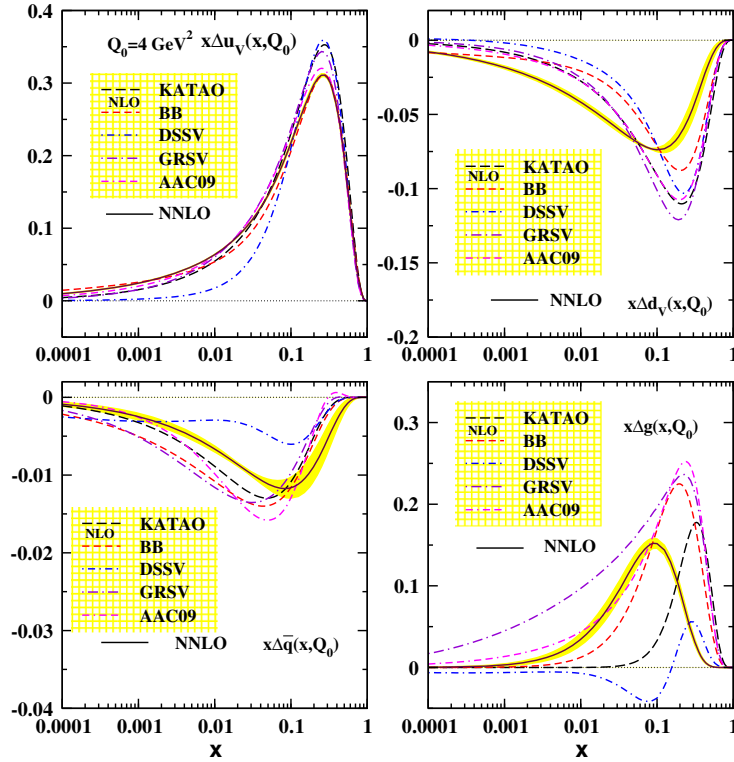
Figure 2.4: The helisity distribution function of a nucleon obtained with next-to-next-leading order calculation from a global analysis of spin-dependent structure functions [30]. The solid black line were obtained in the paper while the others are from previous studies based on the next-to-leading order. Q^2 is fixed to $4\,\mathrm{GeV}^2$.

are pioneers of the measurements via DIS with a polarised beam and a polarised target, so-called polarised DIS [17] [18]. In the same way as the unpolarised case, the spin-dependent structure function g_1 is understood as a sum of the helicity distribution of partons:

$$g_1(x) = \frac{1}{2} \sum_q e_q^2 g_{1L,q}(x). \tag{2.8}$$

The results from these experiments agreed to a simple picture for the spin structure of a nucleon: "the nucleon spin consists of (almost) only quark spin". In 1988, EMC experiment at CERN measured the spin-dependent structure function of the proton g_1^p and concluded that quark spins carry $1 \pm 12 \pm 24\,\%$ of proton spin [19]. This surprising report raised "Proton spin crisis" [20], and many groups started investigations via not only the DIS but also the SIDIS process. The SIDIS measurement requiring both the scattered lepton and at least one secondly hadron, typically a pion or a kaon, permits to separate the helicity distribution into flavours. The SMC experiment performed the first flavour separation for the helicity distribution via the polarised SIDIS measurements [21] [22]. The HERMES experiment at DESY [23, 24], the COMPASS experiment at CERN [25–27], the experiments at JLab [28, 29], and the RHIC at BNL have contributed for the investigation. Fig. 2.4 shows the helicity distribution functions of the valence u-quark, the valence d-quark, the anti-quark, and the gluon obtained from various global QCD analyses [30]. The solid black line was the latest result with next-to-next-leading order calculation while the other lines are obtained with next-to-leading order calculation. In the paper [30], the quark and gluon spin contribution $\Delta\Sigma$, ΔG to the nucleon spin were estimated to be about 0.29 and $0.33 - 0.51$, respectively.
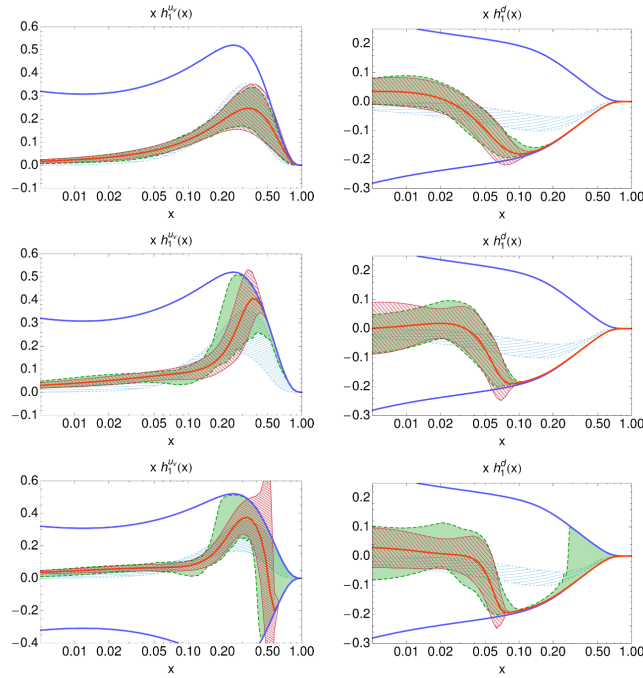
Figure 2.5: The transversity distribution at $Q^2 = 2.4 \, \text{GeV}^2$ of a nucleon extracted from the global analysis of the COMPASS and HERMES data [32]. The plots on the left and the right are distributions of the up and the down valence quark, respectively. Different scenarios are assumed for the top to the bottom row. The red lines and areas indicate the results of the best fit and their error in one standard deviation.

Analogous to the helicity distribution, the transversity distribution, which was introduced firstly in [31], is a probability of finding transversely polarised partons in a transversely polarised nucleon as expressed as follows

$$h_{1,q}(x) = \sum_q f_{1,q}^{\uparrow}(x) - f_{1,q}^{\downarrow}(x), \qquad (2.9)$$

where $f_1^{\uparrow}$ and $f_1^{\downarrow}$ are the number density distribution function with transverse spin parallel or anti-parallel to the transversely polarised nucleon. Note that there is no gluon transversity in the nucleon due to helicity conservation. Since the transversity distribution is chiral-odd while a corresponding observable should be chiral-even, the distribution can only be measured as a convolution with the other chiral-odd quantity, in other words, DIS cannot access to the transversity. SIDIS measurement can give a convolution of the transversity with a chiral-odd fragmentation function. Fig. 2.5 is the transversity distribution of the up and the down valence quarks in the nucleon obtained from a global analysis of the COMPASS, HERMES, and Belle data. The plots are presented after applying Q^2 evolution to $2.4 \, \text{GeV}^2$ after the global analysis.

2.2 Transverse-momentum-dependent parton distribution function

When a transverse momentum of the parton k_T is considered, five TMD-PDFs are needed to describe the nucleon structure in addition to the three PDFs introduced in Sec. 2.1. The three PDFs f_1, g_{1L}, and h_1 depend on k_T but survives after integration over k_T. Fig. 2.6 summarises the eight PDFs. The columns and the rows correspond to spin state of the nucleon

Figure 2.6: Summary of the PDFs at leading twist. The columns and rows correspond to a spin state of nucleon and parton. The notations U, L and T mean un-, longitudinal- and transversely-polarisation. The yellow and blue arrows are spin direction of nucleon and parton, respectively. The red arrows indicate consideration of a transverse momentum of a parton.

and the parton, respectively. The subscript 1 indicates that they are leading-twist quantities. The notation L and T show longitudinal or transverse polarised nucleon, $\perp$ means that the parton has a transverse momentum. TMD-PDFs vanish if they are integrated over k_T since they are an odd distribution of k_T.

2.2.1 The Sivers Distribution

Historically, the Sivers distribution function [33] was proposed to explain a sizeable single spin asymmetry (SSA) of a pion production on scattering experiments of a proton and a transversely polarised proton [34, 35]. The Sivers distribution $f_{1T}^{\perp}$ is related to the number density of unpolarised partons in a transversely polarised nucleon:

$$
\begin{aligned}
f_{1,q/N\uparrow}(x, \mathbf{k}_T) - f_{1,q/N\downarrow}(x, \mathbf{k}_T) &= f_{1,q/N\uparrow}(x, \mathbf{k}_T) - f_{1,q/N\uparrow}(x, -\mathbf{k}_T) \\
&= -2\frac{|\mathbf{k}_T|}{M}\sin(\phi_k - \phi_S)f_{1T}^{\perp}(x, \mathbf{k}_T^2), \quad (2.10)
\end{aligned}
$$

where $\mathbf{k}_T$ is a vector of the intrinsic transverse momentum of the parton and $f_{1,q/N\uparrow}(x, \mathbf{k}_T)$ is the number density of a parton q with a momentum fraction x and a transverse momentum k_T in the transversely polarised nucleon, $(\phi_k - \phi_S)$ is a relative azimuthal angle between the target spin and the transverse momentum of the parton. A value of the Sivers distribution relates to existence of orbital angular momentum of the parton. If the value is zero, it suggests that the orbital angular momentum of the parton does not exist.

The Sivers distribution and the Boer-Mulders distribution, which will be discussed in the
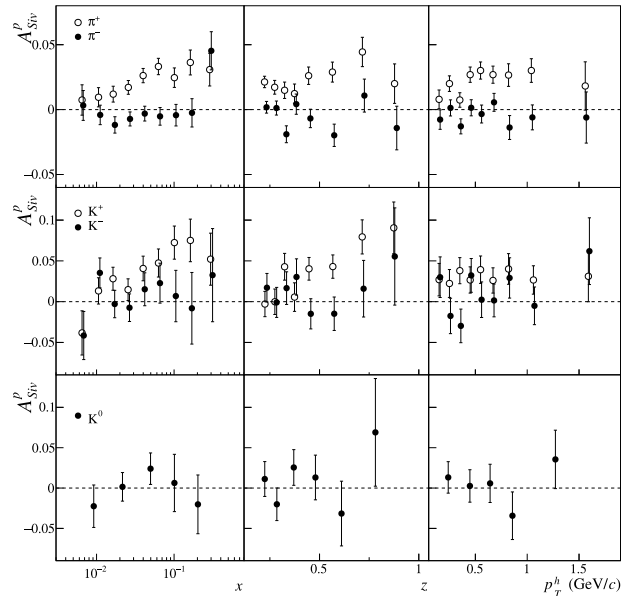
Figure 2.7: Asymmetries related to the Sivers distribution obtained via the SIDIS process with a transversely polarised target in COMPASS [38]. The top, middle and bottom plots are obtained by requiring a pion, charged kaon and neutral kaon as a function of x, z, and p_T^h, respectively.

next subsection, are known as a naïve time reversal odd distribution [2] while the other TMD-PDFs are even. Since they are T-odd, they were formerly considered to be zero by the time-reversal property of QCD [36]. According to a discussion by Collins [37], they can be nonzero because of a presence of a gauge-line operator contained by a non-local quark-quark correlator for the need of the colour-gauge invariance in the definition of TMD-PDFs. While ensuring the colour-gauge invariance of the correlator, this gauge-link operator makes them process dependent. In the SIDIS process, the T-odd distributions are associated with a final-state interaction through gluon exchange between the outgoing parton and the target spectator system. In the DY process, the T-odd distributions are associated with an initial-state interaction through gluon exchange between the incoming parton and the target spectator system. As a result, the sign of the T-odd distributions measured via the DY process is opposite to that via the SIDIS process. Although an experimental confirmation of this non-universality of the T-odd distributions is a crucial test for a QCD TMD approach, the measurement via DY had not been performed.

Measurements related to the Sivers distribution had been performed by COMPASS [38], HERMES [39], and JLab-Hall A [40] via SIDIS. In the measurements, an effect of the Sivers distribution appears in asymmetry of an azimuthal angle of a leading hadron in the final state. Fig. 2.7 shows asymmetry related to the Sivers distribution obtained via the SIDIS process of a muon by a transversely polarised proton target. Global analysis had been carried out to extract the Sivers distribution by several groups [41–44]. The extracted Sivers distribution of u, d, $\overline{u}$, and $\overline{d}$ by [44] are presented in Fig. 2.8. The red lines and grey bars represent the extracted Sivers distributions and their error, respectively. The plots on the left and the right correspond to the Sivers distribution as a function of the Bjorken variable x and k_T. The blue lines indicate the upper limit of the Sivers distribution.

---

[2]Naïve time reversal odd distribution means an odd function under an operation reversing a direction of time, but the initial and the final states remain the same. A T-odd distribution does not mean that time reversal is violated.
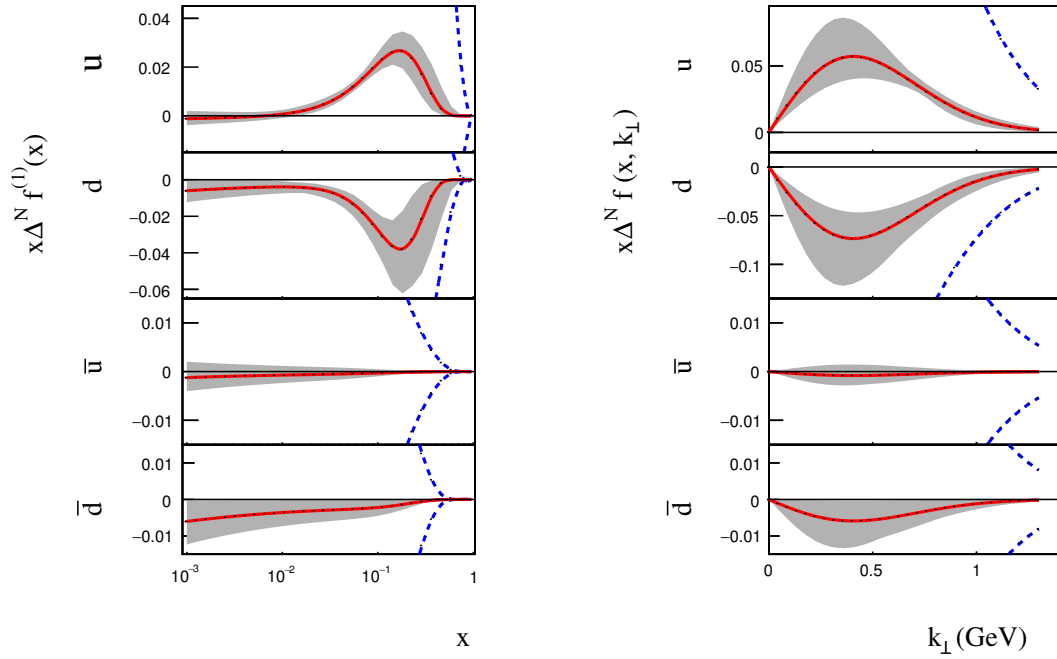
Figure 2.8: Extracted Sivers distributions for u, d, $\overline{\text{u}}$, and $\overline{\text{d}}$ at $Q^2 = 2.4$ GeV^2 [44]. Plots on the left shows the Sivers distribution as a function of x while the right are as a function of k_T with $x = 0.1$. The symbol $\Delta^N f^{(1)}$ means the Sivers distribution of the quark in the nucleon, and the $k_\perp$ is the intrinsic transvers momentum of the quark. The red line and the gray areas correspond to the best fit and error in 95 % confidential level. The blue dashed lines mean the positivity bound of the Sivers distribution.

2.2.2 The Boer-Mulders Distribution

Similarly to the Sivers distribution, the Boer-Mulders distribution [16] describes a correlation between the transverse spin of a parton and the k_T in an unpolarised parent hadron:

$$f_{1,q\uparrow/N}(x, \mathbf{k}_T) - f_{1,q\downarrow/N}(x, \mathbf{k}_T) = \frac{|\mathbf{k}_\perp|}{M} \sin(\phi_k - \phi_s) h_1^\perp(x, \mathbf{k}_T^2), \qquad (2.11)$$

where $f_{1,q^{\uparrow(\downarrow)}/N}$ represents the number density function of a parton q with a transverse spin to up (down), and $(\phi_k - \phi_s)$ is a relative azimuthal angle between the parton spin ant its transverse momentum. According to Boer:

> This is simply how one sees the proton in high energy scattering processes. I like to compare it to an X-ray picture of myself which displays what I look like when viewed by X-rays. The X-rays are not part of me, but their interaction with me does produce a picture of me, even if it looks different from the more familiar ones in the visible light spectrum. [45].

The Boer-Mulders distribution originates from initial or final state interactions between the stuck parton and the spectator of the parent hadron, which are important to ensure the gauge invariance of the TMD-PDFs. The distribution was proposed to explain property of a parameter ν in an angular distribution on the DY process. DY process and measurements of an angular distribution will be described in Sec. 2.3.1.

The Boer-Mulders distribution has been extracted [46, 47] from pd and pp DY process of E866 collaboration at FNAL [48, 49] as Fig. 2.9 shows. The solid and dashed lines represent
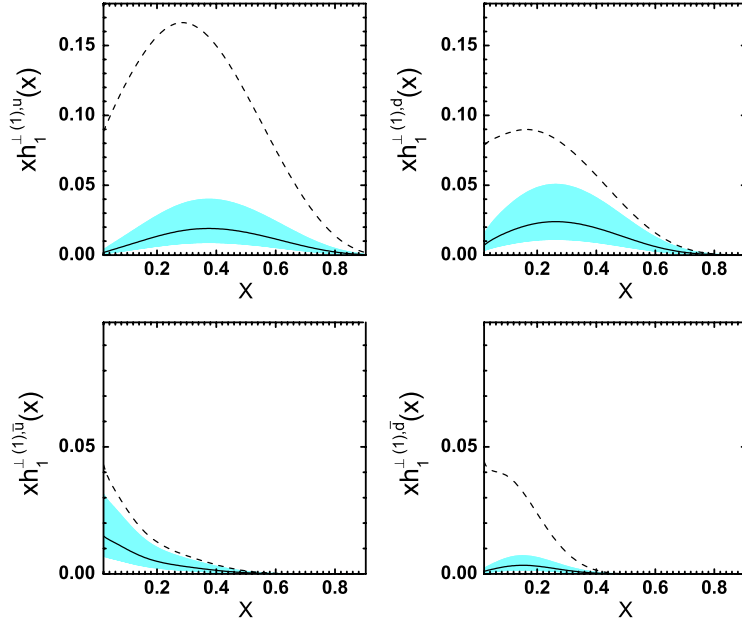
Figure 2.9: First momentus of the Boer-Mulders functions for u, $\overline{\text{u}}$, d, and $\overline{\text{d}}$ for $Q^2 = 1$ GeV^2 extracted from DY data [47].

the extracted distributions and upper limits, respectively. For this extraction, the scale dependence of the Boer-Mulders functions are assumed to behave the same as the number density distribution.

Extraction of the Boer-Mulders distribution from unpolarised SIDIS measurements was also performed [50]. The observable used for the extraction is related with the Boer-Mulders distribution and a function at twist-4, called Cahn effect [51, 52]. Sign of the extracted Boer-Mulders distributions were the same as theoretical expectations, but the result was not sufficient for a quantitative discussion mainly because of the poorly known Canh effect.

2.3 The Drell-Yan process

Production of a massive lepton pair in hadron-hadron collisions, nowadays knows as the DY process, was proposed in [53]. A parton-level Feynman diagram of the DY process $q + \bar{q} \rightarrow \gamma^*/Z \rightarrow l + \bar{l}$ at the leading-twist is illustrated in Fig. 2.10a. The virtual photon or a Z boson is produced by annihilation of a quark and anti-quark pair and decays into a lepton and anti-lepton pair. The lepton pair is called dilepton, especially in the case of a muon and anti-muon, dimuon. The first measurement of the DY process was carried out in AGS at BNL [54].

For discussions, let us introduce two frames, the target rest (TR) frame and the Collins-Soper (CS) frame [55] as drawn in Fig. 2.12 and Fig. 2.11, respectively. In the TR frame, three-momentum of the target nucleon is taken to be zero vector. The z-axis is parallel to the beam momentum in a lab frame. The x-z plane is defined by the beam and the virtual photon momenta. The x-axis is parallel to a transverse component of a dilepton momentum q_T in the x-z plane. The y-axis completes a right-handed frame. The CS frame is one of a rest frame of the virtual photon and commonly used to discuss an angular distribution of the dilepton produced via the DY process. In the CS frame, the z-axis takes a bisector of $\vec{P}_\pi$ and $-\vec{P}_N$. The y-axis takes to a cross product of momenta of the beam and the target. The x-axis completes a right-handed frame. Table 2.1 summarises kinematic variables in the DY process.
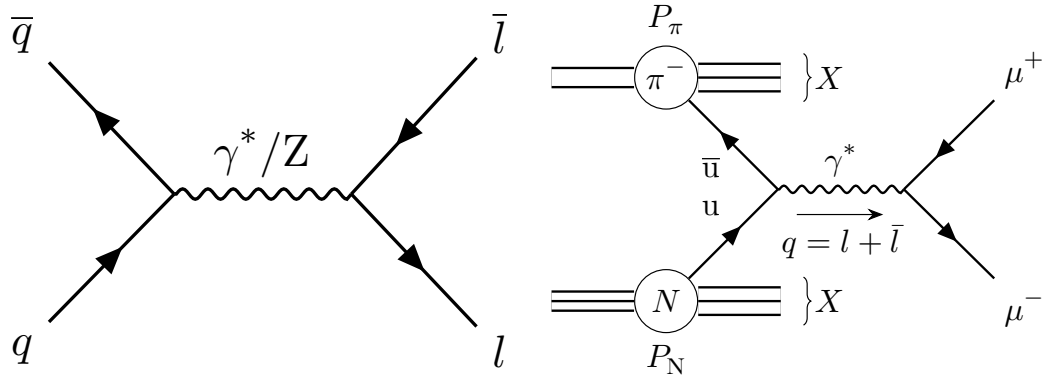
(a) Parton-level Feynman diagram of the DY process at the leading twist.

(b) Feynman diagram of the polarised DY process measured at COMPASS.

Figure 2.10: The left figure illustrates a Feynman diagram of the Drell-Yan process at parton level at the leading twist. A virtual photon or Z boson produced by an annihilation of a quark and anti-quark pair decays into a lepton and anti-lepton pair.
The right figure illustrates a Feynman diagram of the polarised DY process measured at COMPASS. Since the COMPASS spectrometer has an acecptance in valence region of the beam pion and the target proton, annihilation of u and $\bar{u}$ is mainly measured. Only muon and anti-muon pairs are detected by the spectrometer.

Table 2.1: Difinition of kinematic variables and angles. The subscription CS and TF denote that the variable is defined in the CS frame and TR frame, respectively.

|	
P_π, P_N	four-momenta of the beam pion and the target nucleon
$l, \bar{l}$	four-momenta of the lepton and antilepton
$q \equiv l + \bar{l}$	four-momenta of the virtual photon
$Q^2 = q^2$	photon virtuality
$M^2_{\mu\mu} = Q^2$	invariant mass squared of the virtual photon, often called dimuon mass
$x_\pi = q^2/(2P_\pi \cdot q)$	Bjorken x of the beam pion
$x_N = q^2/(2P_N \cdot q)$	Bjorken x of the target nucleon
$x_F = x_\pi - x_N$	Feynman variable
q_T	transverse component of the virtual photon momentum in the TR frame
S_T	transverse component of the target polarisation vector in the TR frame
ϕ_S	angle between q_T and S_T in TR frame
ϕ_{CS}	angle between the hadron plane and the dilepton plane in the CS frame
θ_{CS}	angle between the z-axis and momentum of a positively charged lepton in the dilepton plane in CS
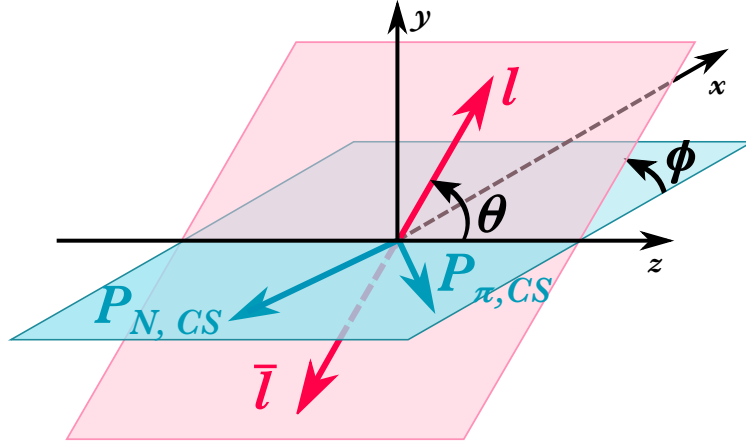
Figure 2.11: Sketch of the DY process in the CS frame. The blue and red planes respresent a plane defined by dilepton and by the beam and the target hadron.
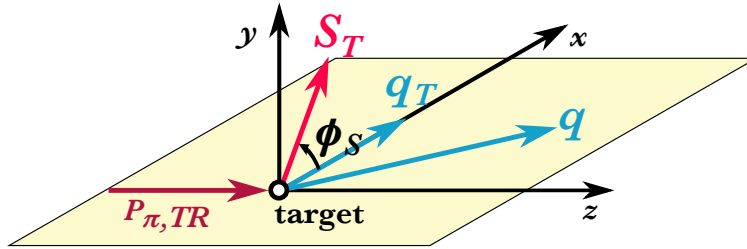

Figure 2.12: Sketch of the DY process in the TR frame. The yellow plane is defined by the beam hadron and the virtual photon.

In the case of the polarised DY measurement at COMPASS, which is the theme of this thesis, a negatively charged pion beam with a momentum of $190\,\mathrm{GeV}/c$ and a transversely polarised proton target are used, and a dimuon is detected as Fig. 2.10b: $\pi^- + \mathrm{p}^\uparrow \to \mu^- + \mu^+ + X$, where the notation $\uparrow$ means transverse polarisation and X represents many particles not detected. Since a cross-section of the $q\bar{q}$ annihilation to γ^* is proportional to a square of the quark charge, the cross-section of $\mathrm{d\bar{d}}$ is suppressed by factor four with respect to one of u $\bar{\mathrm{u}}$. Measurable Bjorken x of the beam and the target are in a valence region as will be shown in Fig. 5.9. Therefore annihilation of a valence u in the target nucleon and an $\bar{\mathrm{u}}$ in the beam pion is dominant in the measurement.

2.3.1 Angular Distribution

The following equation gives a cross-section of the DY process with unpolarised hadrons in the CS frame:

$$\frac{1}{\sigma}\frac{d\sigma}{d\Omega} = \frac{3}{4\pi}\frac{1}{\lambda+3}\left(1 + \lambda\cos^2\theta_{\mathrm{CS}} + \mu\sin 2\theta_{\mathrm{CS}}\cos\phi_{\mathrm{CS}} + \frac{\nu}{2}\sin^2\theta_{\mathrm{CS}}\cos 2\phi_{\mathrm{CS}}\right), \quad (2.12)$$

where θ_{CS} and ϕ_{CS} are angles defined in the CS frame. If the virtual parton has no transverse momentum, the coefficients λ, μ, and ν are determined by the nature of a spin-half particle:

$$\lambda = 1, \ \mu = \nu = 0. \quad (2.13)$$

Based on perturbative QCD [56], a relation, so-called Lam-Tung (LT) relation, $1 - \lambda - 2\nu = 0$ holds. A general positivity constraints for the angular distributions of dilepton require other
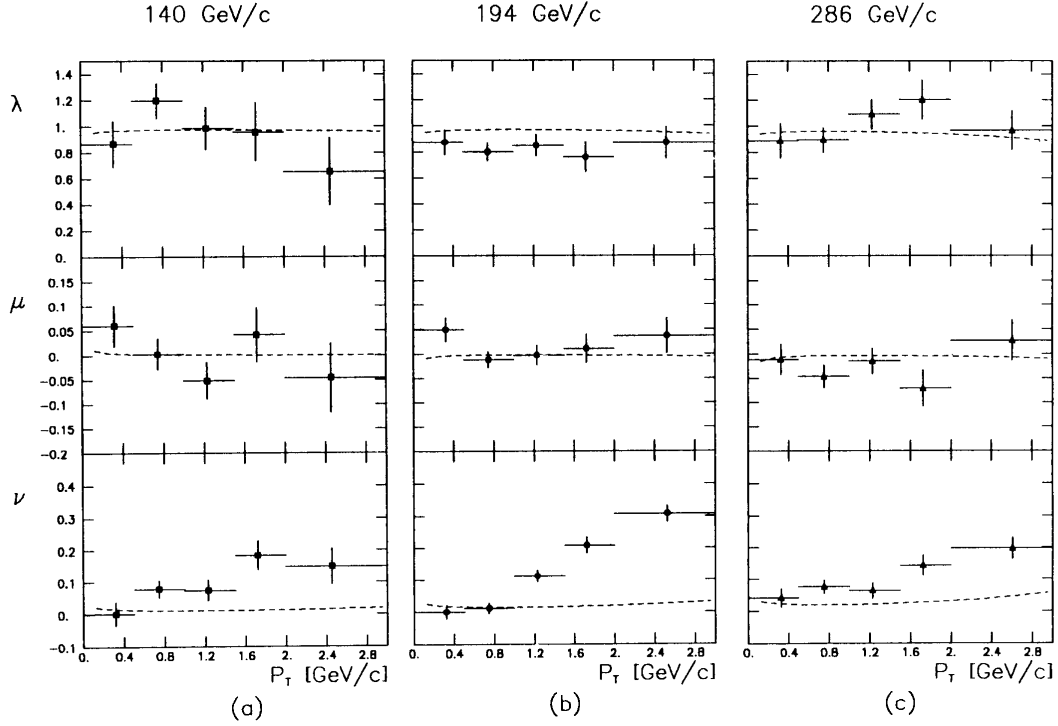
Figure 2.13: Angular distribution of dimuons on the DY process as a function of q_T measured by NA10 [58]. (a), (b) and (c) are measurements with different beam momenta, 140, 194 and 286 GeV/c, respectively. If the Lam-Tung relation holds, data plots in the bottom column are on the dashed line.

relations to the coefficients [57]

$$|\lambda| \le 1, \ |\nu| \le 1 + \lambda, \ \mu^2 \le \frac{(1-\lambda)(1+\lambda-\nu)}{4}. \tag{2.14}$$

The NA10 experiment at CERN was the first experiment that measured angular distribution of dileptons from the pion-induced DY process [58]. The measured λ, μ, and ν as a function of q_T with different beam momenta 140, 194 and 286 GeV/c are shown in Fig. 2.13. The row corresponds to λ, μ, or ν, and the column corresponds to the beam momenta. If the LT relation holds, data points for ν will be on the dashed line. Therefore a break of the LT relation was observed.

Experiments which measured the angular distribution on the DY process are summarised in Table 2.2. In the pion-induced DY, the LT is violated as presented above. In the proton-induced DY, the LT is satisfied for the proton target [49] while it seems to be violated with the deuteron target [48]. On the pp collision, the LT is held [59] while violated on the p$\overline{\mathrm{p}}$ collision [60, 61]. A reasonable explanation of a contribution of the higher-twist (HT) with $q\bar{q}$ and qg is given for the collider experiments [62]. However, it does not explain the results from the fixed target experiments.

Table 2.2: A list of experiments which reported dimuon angular distribution on the DY process. The "Year" column shows the time when the results was published. The superscript ↑ indicates a transveselly polarisation. The symbols H, D, and W represent hydrogen, deuterium, and tungsten, respectively. This thesis is about the experiment performed by COMPASS written on the bottom row.

Year	Experiment	Type	Beam	Target or beam	Beam momentum (GeV)	$\sqrt{s}$ (GeV)
1988	NA10 [58]	fixed	π^+	W	140	16.2
		fixed	π^-	W	194	19.1
		fixed	π^-	W	286	23.2
		fixed	π^-	D	286	23.2
1989	E615 [63]	fixed	π^-	W	80	12.3
		fixed	π^-	W	252	21.8
2007	E866 [48]	fixed	p	D	800	38.8
2009	[49]	fixed	p	H	800	38.8
2011	CDF [59]	collider	p	$\overline{\text{p}}$	980	1960
2015	CMS [60]	collider	p	p	3500	7000
2016	ATLAS [61]	collider	p	p	3500	7000
2016	STAR [64]	collider	$\text{p}^\uparrow$	p	250	500
2017	COMPASS [65] (this thesis)	fixed	π^-	$\text{p}^\uparrow$	190	18.9

2.3.2 Angular Distribution of the polarised DY process

S. Arnold, *et al.* [66] calculated the general form of angular distribution of the DY process. In the case of an unpolarised beam and a transversely polarised target, it is simplified:

$$\frac{d\sigma}{d^4qd\Omega} = \frac{\alpha_{em}^2}{Fq^2}\hat{\sigma}_U \left[\left\{ 1 + D_{[\sin 2\theta_{\text{CS}}]}A_U^{\cos\phi_{\text{CS}}}\cos\phi_{\text{CS}} + D_{[\sin^2\theta_{\text{CS}}]}A_U^{\cos 2\phi_{\text{CS}}}\cos 2\phi_{\text{CS}} \right\} \right.$$
$$+ |\boldsymbol{S}_T| \left\{ \left(D_{[1]}A_T^{\sin\phi_{\text{S}}} + D_{[\cos^2\theta_{\text{CS}}]}\tilde{A}_T^{\sin\phi_{\text{S}}} \right) \sin\phi_{\text{S}} \right.$$
$$+ D_{[\sin 2\theta_{\text{CS}}]} \left(A_T^{\sin(\phi_{\text{CS}}+\phi_{\text{S}})}\sin(\phi_{\text{CS}}+\phi_{\text{S}}) + A_T^{\sin(\phi_{\text{CS}}-\phi_{\text{S}})}\sin(\phi_{\text{CS}}-\phi_{\text{S}}) \right)$$
$$\left. \left. + D_{[\sin^2\theta_{\text{CS}}]} \left(A_T^{\sin(2\phi_{\text{CS}}+\phi_{\text{S}})}\sin(2\phi_{\text{CS}}+\phi_{\text{S}}) + A_T^{\sin(2\phi_{\text{CS}}-\phi_{\text{S}})}\sin(2\phi_{\text{CS}}-\phi_{\text{S}}) \right) \right\} \right],$$
$$(2.15)$$

where α_{em} is the coupling constant of the electromagnetic interaction, the solid angle Ω is the orientation of the lepton, $F = 4\sqrt{(P_\pi \cdot P_N)^2 - M_\pi^2 M_N^2}$ represents a flux of the incoming hadrons, the subscriptions U and T denote un- and transversely polarised states of the target hadron, respectively. $|\boldsymbol{S}_T|$ is the target polarisation. The asymmetries are depend on $P_\pi \cdot q$, $P_N \cdot q$, and q^2. The four asymmetries which depend on the target polarisation are called the transverse spin asymmetries (TSAs). The terms A_{pol}^f corresponds the asymmetry related to the modulation term f. The depolarisation factor $D_{[g]}$ is given by

$$D_{[g(\theta_{\text{CS}})]} = \frac{g(\theta_{\text{CS}})}{1 + A_U^1 \cos^2\theta_{\text{CS}}}, \quad (2.16)$$

where the A_U^1 is the same as λ introduced in Eq. (2.12). $\hat{\sigma}_U$, which survives after integration over the azimuthal angles ϕ and ϕ_{CS}, is given by

$$\hat{\sigma}_U = (F_U^1 + F_U^2)(1 + A_U^1 \cos^2 \theta_{\mathrm{CS}}). \tag{2.17}$$

The asymmetries A_{pol}^f in the CS frame are given as follows:

$$A_U^1 = \frac{F_U^1 - F_U^2}{F_U^1 + F_U^2}$$

$$A_U^{\cos\phi_{\mathrm{CS}}} = \frac{F_U^{\cos\phi_{\mathrm{CS}}}}{F_U^1 + F_U^2} \qquad\qquad A_U^{\cos 2\phi_{\mathrm{CS}}} = \frac{F_U^{\cos 2\phi_{\mathrm{CS}}}}{F_U^1 + F_U^2}$$

$$A_T^{\sin\phi_{\mathrm{S}}} = \frac{F_T^1 + F_T^2}{F_U^1 + F_U^2} \qquad\qquad \tilde{A}_T^{\sin\phi_{\mathrm{S}}} = \frac{F_T^1 - F_T^2}{F_U^1 + F_U^2}$$

$$A_T^{\sin(\phi_{\mathrm{CS}}+\phi_{\mathrm{S}})} = \frac{F_T^{\sin\phi_{\mathrm{CS}}} + F_T^{\cos\phi_{\mathrm{CS}}}}{2(F_U^1 + F_U^2)} \qquad A_T^{\sin(\phi_{\mathrm{CS}}-\phi_{\mathrm{S}})} = \frac{F_T^{\sin\phi_{\mathrm{CS}}} - F_T^{\cos\phi_{\mathrm{CS}}}}{2(F_U^1 + F_U^2)}$$

$$A_T^{\sin(2\phi_{\mathrm{CS}}+\phi_{\mathrm{S}})} = \frac{F_T^{\sin 2\phi_{\mathrm{CS}}} + F_T^{\cos 2\phi_{\mathrm{CS}}}}{2(F_U^1 + F_U^2)} \qquad A_T^{\sin(2\phi_{\mathrm{CS}}-\phi_{\mathrm{S}})} = \frac{F_T^{\sin 2\phi_{\mathrm{CS}}} - F_T^{\cos 2\phi_{\mathrm{CS}}}}{2(F_U^1 + F_U^2)}, \tag{2.18}$$

where the functions F_{pol}^1 and F_{pol}^2 are structure functions at the leading-twist and twist-3, respectively. $A_U^{\cos\phi_{\mathrm{CS}}}$ and $A_U^{\cos 2\phi_{\mathrm{CS}}}$ are the same as μ and ν in Eq. (2.12), respectively. Under the leading-twist approximation, the structure function F_U^2 becomes zero. Therefore, $A_U^1 = \lambda = 1$. While the measured lambda in the pion-induced DY experiments was found to be different from one, down to about 0.5. Detailed treatment of the parameter lambda in asymmetry analysis will be discussed in Chapter 5.

2.3.3 Asymmetries in the leading-twist QCD-quark-parton model

According to the factorisation theorem, the structure functions of the DY process at high energies (s, $Q^2 \gg M_\pi^2, M_{\mathrm{N}}^2$) and small transverse momentum of the virtual photon ($q_T \gg q$) can be expressed as a convolution of TMD-PDFs of the beam and the target hadrons [66] in intrinsic-transverse-momentum space as

$$\mathcal{C}[w(\mathbf{k}_{T,\pi}, \mathbf{k}_{T,\mathrm{N}}) f_1 \bar{f}_2] \equiv \frac{1}{N_c} \sum_q e_q^2 \int d^2 \mathbf{k}_{T,\pi} d^2 \mathbf{k}_{T,\mathrm{N}} \delta^{(2)}(\mathbf{q}_T - \mathbf{k}_{T,\pi} - \mathbf{k}_{T,\mathrm{N}})$$
$$\times w(\mathbf{k}_{T,\pi}, \mathbf{k}_{T,\mathrm{N}}) \left[f_{1,q}(x_a, \mathbf{k}_{T,\pi}^2) f_{2,\bar{q}}(x_b, \mathbf{k}_{T,\mathrm{N}}^2) + f_{1,\bar{q}}(x_a, \mathbf{k}_{T,\pi}^2) f_{2,q}(x_b, \mathbf{k}_{T,\mathrm{N}}^2) \right], \tag{2.19}$$

where $N_c = 3$ is the number of colours. In the leading-twist QCD-quark-parton model, since F^2 is zero, Eq. (2.15) is simplified to:

$$\frac{d\sigma}{d^4 q d\Omega} = \frac{\alpha_{em}^2}{F q^2} \hat{\sigma}_U \left[\left\{ 1 + D_{[\sin^2 \theta_{\mathrm{CS}}]} A_U^{\cos 2\phi_{\mathrm{CS}}} \cos 2\phi_{\mathrm{CS}} \right\} \right.$$
$$+ |\boldsymbol{S}_T| \left\{ A_T^{\sin\phi_{\mathrm{S}}} \sin\phi_{\mathrm{S}} \right.$$
$$\left. \left. + D_{[\sin^2 \theta_{\mathrm{CS}}]} \left(A_T^{\sin(2\phi_{\mathrm{CS}}+\phi_{\mathrm{S}})} \sin(2\phi_{\mathrm{CS}} + \phi_{\mathrm{S}}) + A_T^{\sin(2\phi_{\mathrm{CS}}-\phi_{\mathrm{S}})} \sin(2\phi_{\mathrm{CS}} - \phi_{\mathrm{S}}) \right) \right\} \right], \tag{2.20}$$

where

$$\hat{\sigma}_U = F_U^1 (1 + \cos^2 \theta_{\mathrm{CS}}) \tag{2.21}$$

$$D_{[f(\theta_{\mathrm{CS}})]} = \frac{f(\theta_{\mathrm{CS}})}{1 + \cos^2 \theta_{\mathrm{CS}}}. \tag{2.22}$$

The asymmetries at the leading-twist are given as ratios of corresponding structure functions to the unpolarised structure function

$$F_U^1 = \mathcal{C}[f_a, \bar{f}_a] \tag{2.23}$$

as

$$A_U^{\cos 2\phi_{CS}} = \mathcal{C} \left[\left\{ 2(\mathbf{h} \cdot \mathbf{k}_{aT})(\mathbf{h} \cdot \mathbf{k}_{T,\mathrm{N}}) - \mathbf{k}_{aT} \cdot \mathbf{k}_{T,\mathrm{N}} \right\} h_1^\perp \bar{h}_1^\perp \right] \Big/ M_a M_b F_U^1, \tag{2.24}$$

$$A_T^{\sin \phi_S} = \tilde{A}_T^{\sin \phi_S} = \mathcal{C} \left[\mathbf{h} \cdot \mathbf{k}_{T,\mathrm{N}} f_1 \bar{f}_{1T}^\perp \right] \Big/ M_b F_U^1, \tag{2.25}$$

$$A_T^{\sin(2\phi_{CS}+\phi_S)}$$
$$= -\mathcal{C} \left[\left\{ 2 \left(\mathbf{h} \cdot \mathbf{k}_{T,\mathrm{N}} \right) \left[2 \left(\mathbf{h} \cdot \mathbf{k}_{aT} \right) \left(\mathbf{h} \cdot \mathbf{k}_{T,\mathrm{N}} \right) - \mathbf{k}_{aT} \cdot \mathbf{h}_{bf} \right] - \mathbf{k}_{T,\mathrm{N}}^2 \left(\mathbf{h} \cdot \mathbf{k}_{aT} \right) \right\} h_1^\perp \bar{h}_{1T}^\perp \right] \Big/ 4 M_a M_b^2 F_U^1, \tag{2.26}$$

$$A_T^{\sin(2\phi_{CS}-\phi_S)} = -\mathcal{C} \left[\mathbf{h} \cdot \mathbf{k}_{aT} h_1^\perp \bar{h}_1 \right] \Big/ 2 M_a F_U^1, \tag{2.27}$$

where $\mathbf{h} = \mathbf{q}_T / q_T$. Hence the asymmetries in Eqs. (2.24) to (2.27) enable to access:

$A_U^{\cos 2\phi_{\mathrm{CS}}}$	the Boer-Mulders distributions of the beam pion and the target nucleon
$A_T^{\sin \phi_{\mathrm{S}}}$	the number density distribution of the beam pion and the Sivers distribution of the target nucleon
$A_T^{\sin(2\phi_{\mathrm{CS}}+\phi_{\mathrm{S}})}$	the Boer-Mulders distribution of the beam pion and the Pretzelosity distribution of the target nucleon
$A_T^{\sin(2\phi_{\mathrm{CS}}-\phi_{\mathrm{S}})}$	the Boer-Mulders distribution of the beam pion and the Transversity distribution of the target nucleon.

Measurement of TMD-PDFs in the DY process is free from the hadron fragmentations, which are one of the essential components in the SIDIS process. This is a great advantage with respect to measurement via the SIDIS process. In the general expression in Eq. (2.15), the remaining asymmetries can be understood as higher-twist PDFs.

A transverse single-spin asymmetry measurement at RHIC

Recently, measurement of the transverse single spin asymmetry (TSSA) of weak boson production $p + p^\uparrow \to W^\pm / Z^0 + X$ from collision of a proton and a transversely polarised proton with $\sqrt{s} = 500$ GeV was reported by STAR collaboration at RHIC [64]. Transverse SSA (TSSA) defined as $(\sigma_\uparrow - \sigma_\downarrow)/(\sigma_\uparrow + \sigma_\downarrow)$ of decay of the produced weak boson $W^\pm \to l^\pm + \nu$ or $Z^0 \to {}^+ + l^-$ was measured. Here, $\sigma_{\uparrow(\downarrow)}$ indicates a cross-section with a positively(negatively) polarised beam. The obtained TSSA is presented in Fig. 2.14. A combined fit of the theoretical prediction without TMD evolution to W^+ and W^- asymmetries shown in the plot gave a $\chi^2/\mathrm{NDF} = 7.4/6$ assuming a sign change in the Sivers distribution and a $\chi^2/\mathrm{NDF} = 19.6/6$ otherwise, where NDF represents a number of degree of freedom. The theoretical prediction with the sign change in the Sivers distribution describes the obtained TSSA better than that without the sign change.
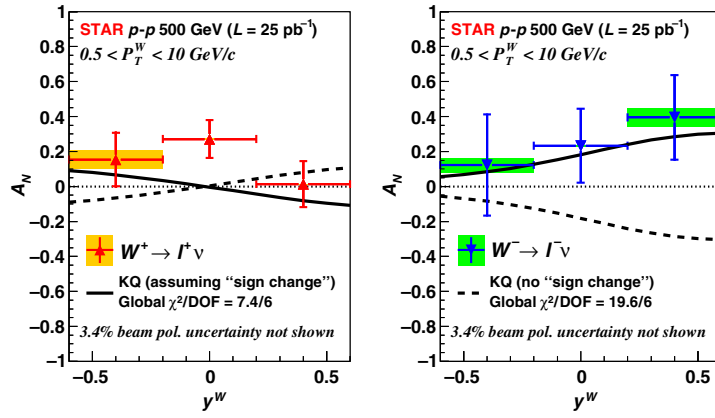
Figure 2.14: Amplitude of transverse single-spin asymmetry as a function of a weak boson rapidity y^w along with theoritical prediction with the non-TMD-evelved KQ model [64]. The left and right plots are for W^+ and W^- production, respectively. The solid and dashed lines are suuming or exclusing the sign change prediction in the Sivers distribituion.

Chapter 3

The COMPASS experiment

The COMPASS collaboration inherits two projects: HMC for study of the nucleon structure and CHEOPS for study of hadronic structure, a semi-leptonic decay of charmed baryons and a search for exotic baryon states. The COMPASS spectrometer is in the north area of CERN, and a beam is provided by SPS. A PT or various nuclear targets are used depending on the physics goals. Details of the PT will be discussed in Chapter 4.

This chapter offers introductions of the COMPASS collaboration, the COMPASS spectrometer, and data reconstruction. New equipment and specific upgrades of detectors are described minutely.

3.1   Overview

The COMPASS collaboration studies structure of the nucleon and hadron spectroscopy using a beam from SPS at CERN. The study of the nucleon structure using a muon beam is called the muon program. The first proposal, which is referred as phase-I, was approved in 1997, and the data taking was started in 2002. In the phase-I, gluon polarisation measurement, SIDIS measurement with a transversely polarised target and hadron spectroscopy were performed. The COMPASS phase-II was started in 2012 for measurements of Deeply Virtual Compton Scattering, Primakoff effect, polarisability of a pion, and the polarised DY processes. Table 3.1 summarises the measurements carried out at COMPASS.

A pilot run for the DY measurement with an unpolarised ammonia target was carried out for about three weeks in 2014, and DY measurement with PT was performed in 2015. Stable DY measurement lasted for about four months was performed with a negatively charged pion beam with a momentum of $190 \,\mathrm{GeV}/c$. The choice of the momentum was for having enough large cross-section of the DY process and the Bjorken variables of the beam and the target in a valence region at the same time. Fig. 3.1 shows estimation of correlation between the Bjorken variables of the beam and the target with several values of the centre of mass energy squared estimated in the proposal of the COMPASS-II experiment [67]. The highest intensity of the hadron beam in history of the COMPASS was used due to a small cross-section of the DY process.

Fig. 3.2 illustrates a side view of the COMPASS setup for the DY measurement. The setup is basically same as one for the SIDIS measurements.

The COMPASS spectrometer is divided into two parts depending on their angle coverage: Large Angle Spectrometer (LAS) and Small Angle Spectrometer (SAS). The LAS locates downstream of the PT and covers the large angle from 35 mrad to 180 mrad while the SAS follows the LAS and covers the small angle from 18 mrad to 35 mrad. Both of the LAS and SAS have a spectrometer magnet, many tracking planes, an electromagnetic calorimeter, a hadronic calorimeter, and a muon identification system. Only the LAS has a Ring Imaging Cherenkov (RICH) detector for particle identification. A review of the standard setup of the COMPASS spectrometer is given by [68, 69].

Essential upgrades for the DY measurement were made for the PT, a hadron absorber, new station of scintillation fibre tracker (SciFi) and new station of a drift chamber (DC). Since the

Table 3.1: History of runs in COMPASS mainly for muon programs. A notation h in the beam column means a hadron beam mainly composed of pions.

Year	Physics	Beam (GeVc)	Target	PT config.
2002	SIDIS	$\mu^{\pm}$, 160	^{6}LiD	long. and trans.
2003	SIDIS	$\mu^{\pm}$, 160	^{6}LiD	long. and trans.
2004	SIDIS	$\mu^{\pm}$, 160	^{6}LiD	long. and trans.
2005		*Shutdown*		
2006	SIDIS	$\mu^{\pm}$, 160	^{6}LiD	long.
2007	SIDIS	$\mu^{\pm}$, 160	NH_3	long. and trans.
2008		*Hadron spectroscopy*		
2009		*Hadron spectroscopy*		
2010	SIDIS	μ^{+}, 160	NH_3	trans.
2011	SIDIS	μ^{+}, 200	NH_3	long.
2012	DVCS pilot run	$\mu^{\pm}$, 160	Liq. H_2	unpol.
2013		*Shutdown*		
2014	DY pilot run	h^{-}, 190	NH_3	unpol
2015	DY	h^{-}, 190	NH_3	trans.
2016	DVCS	$\mu^{\pm}$, 160	Liq. H_2	unpol.
2017	DVCS	$\mu^{\pm}$, 160	Liq. H_2	unpol.
2018	DY	h^{-}, 190	NH_3	trans.
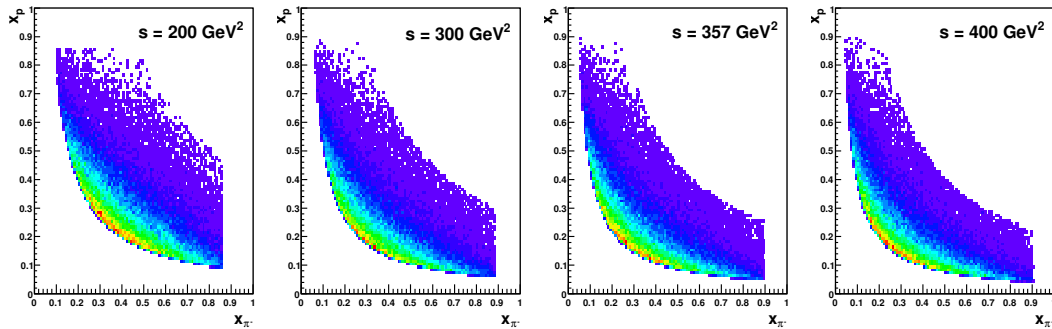
Figure 3.1: Correlations between x_{π^-} and x_p of the DY process $\pi^- + p \rightarrow \mu^+ + \mu^- + X$ in the dimuon mass range from $4\,\mathrm{GeV}/c^2$ to $9\,\mathrm{GeV}/c^2$ [67]. The values of centre of mass energy squared of 200, 300, 357 and $400\,\mathrm{GeV}^2$ correspond to the beam momenta of 106, 160, 190 and $213\,\mathrm{GeV}/c$, respectively.

Table 3.2: Relative composition of the hadron beam [69]. About 97 % of the beam is π^- in the DY measurement.

Momentum	Positive beams			Negative beams		
(GeV/c)	π^+	K^+	p	π^-	K^-	$\bar{p}$
100	0.618	0.015	0.367	0.958	0.018	0.024
160	0.360	0.017	0.623	0.966	0.023	0.011
190	0.240	0.014	0.746	0.968	0.024	0.008
200	0.205	0.012	0.783	0.969	0.024	0.007

high-intensity hadron beam gives a vast amount of secondary particles, the hadron absorber was newly built. To compensate deterioration of tracking precision by the hadron absorber, new SciFi station was installed between parts of the absorber. The new station of DC helps tracking in the LAS since the performance of some detectors were expected to be worse due to ageing. The trigger system was tuned for the measurement and optimised using feedback from the pilot run in 2014. In addition to above upgrades, some upgrades were applied to some detectors.

3.2 Beam

SPS is the second largest accelerator in CERN accelerator complex shown in Fig. 3.3. Protons are injected from PS and can be accelerated up to 450 GeV/c. SPS slowly extracts the proton beam with a momentum of 400 GeV/c during a period of 9.6 sec once in a cycle about 30 to 50 sec. The extracted beam impinges on a production target (T6) at the beginning of the M2 beamline to produce secondary particles. The production target is made of beryllium with 80 mm wide, about 2 mm high, and 500 mm thick for the DY measurement. Many secondary particles are produced and transported to the COMPASS experiment through the M2 beamline. A conceptual layout and components of the beamline are shown in Fig. 3.4 and Fig. 3.5. A series of six high-gradient quadrupole magnets next to the production target collects pions and kaons, and a collimator selects a momentum band up to ± 10 %. The pions and kaons fly a tunnel with being focused and defocused by quadrupole magnets. If a muon beam is requested, a hadron absorber made of beryllium is installed the end of the tunnel to stop all hadrons with minimum perturbation of muons, with about 3 GeV/c^2 energy loss. Collimators following the absorber clean and select momentum of the accepted particles. Finally, the particles are bent onto a horizontal axis and provided to an experimental hall of the COMPASS. In 2015 run, a negative hadron beam with an average intensity 6×10^7/s and a spill length about 6 s was used. The beam was inclined by approximately 1.6 mrad in the horizontal direction considering a vertical magnetic field of the PT dipole magnet. Normally, a hadron beam with an intensity of 1×10^6 s^{-1} is used in COMPASS. The intensity about 10^8 s^{-1} introduces a high-background rate to the detectors and more heat to the PT. It is a challenging attempt for COMPASS.

The hadron beam is composed of some types of particles, and the composition depends on the beam momentum. Table 3.2 summarises composition of the hadron beam for a few typical beam momenta. Two CErenkov Differential counter with Achromatic Ring focus (CEDAR) detectors were installed in the M2 beamline for particle identification of the hadron beam with momentum up to 300 GeV/c [72]. The detector consists of a vessel filled with helium gas, lenses, correctors, diaphragm, condensers and photomultiplier tubes (PMTs) as shown in Fig. 3.6. Since momentum of the beam was selected, the speed of the particle depends on its type. Therefore some particles emit the Cerenkov radiation in the vessel and the other not.
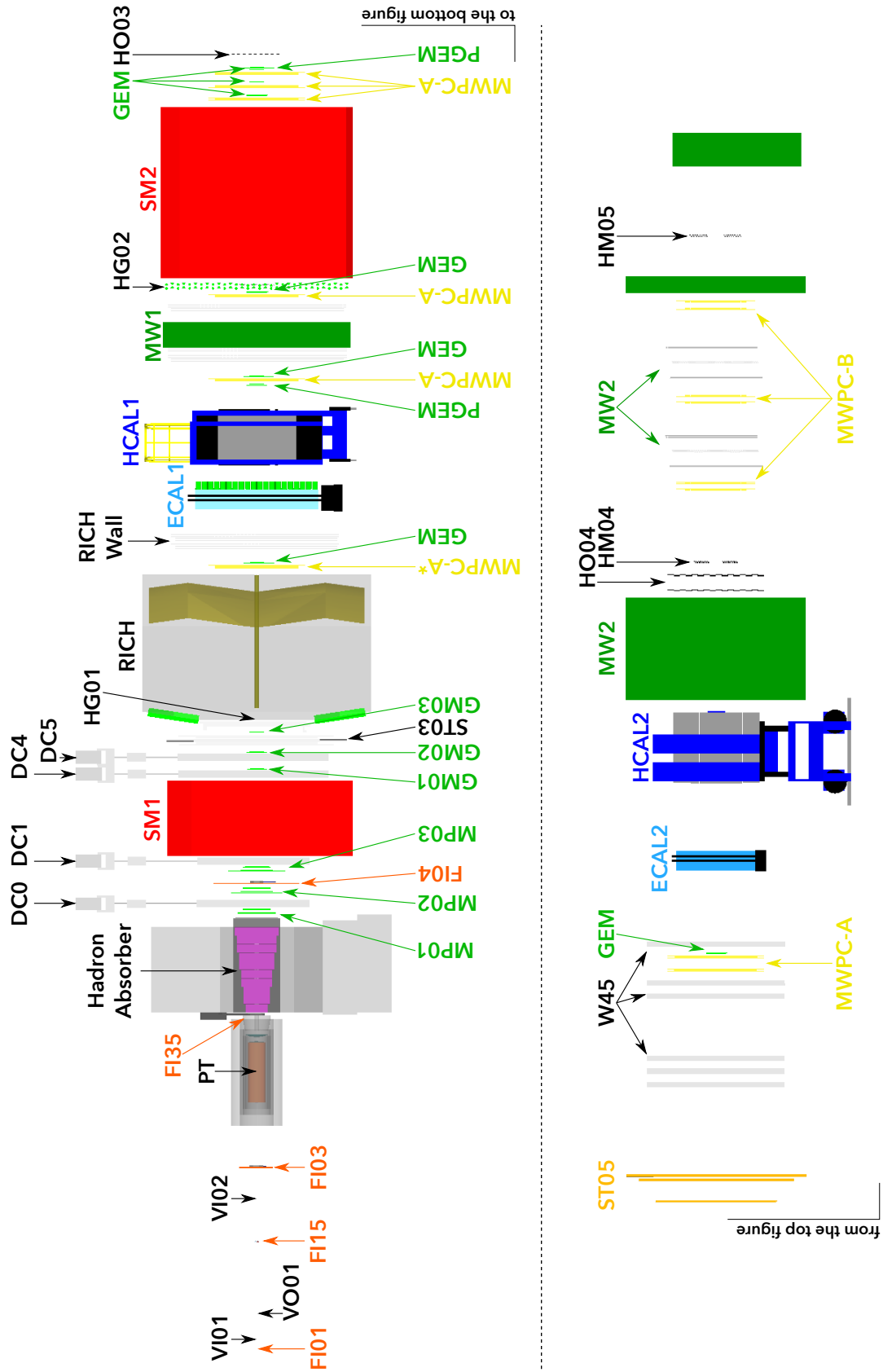
Figure 3.2: Side view of the COMPASS setup for the DY measurement in 2015. The set up is divided into two and drawn on the top for the first half and the bottom for the last half. FI01, VI01 and VI02 are not drawn but indicated their position roughly. A beam goes from left to right.
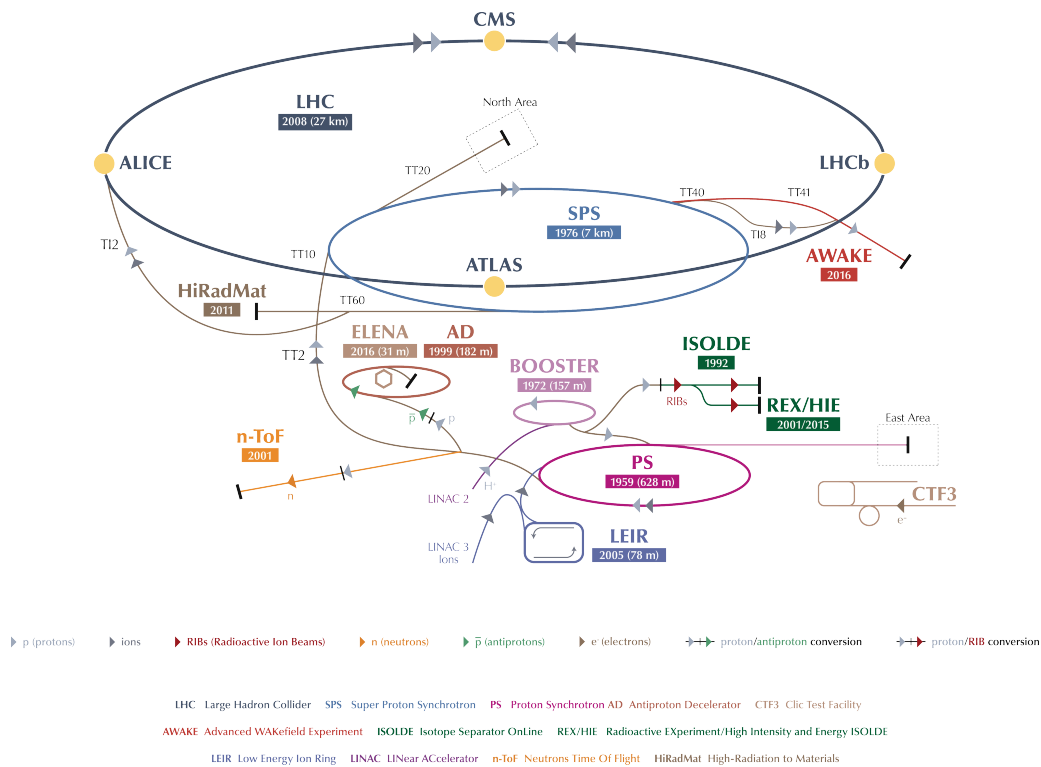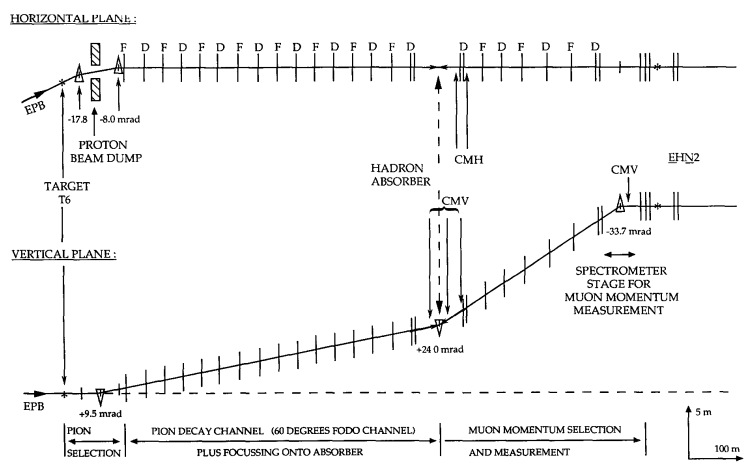
Figure 3.3: The CERN accelerator complex [70].

Figure 3.4: Conceptual layout of the SPS M2 beam line in horizontal and vertical projections [71].
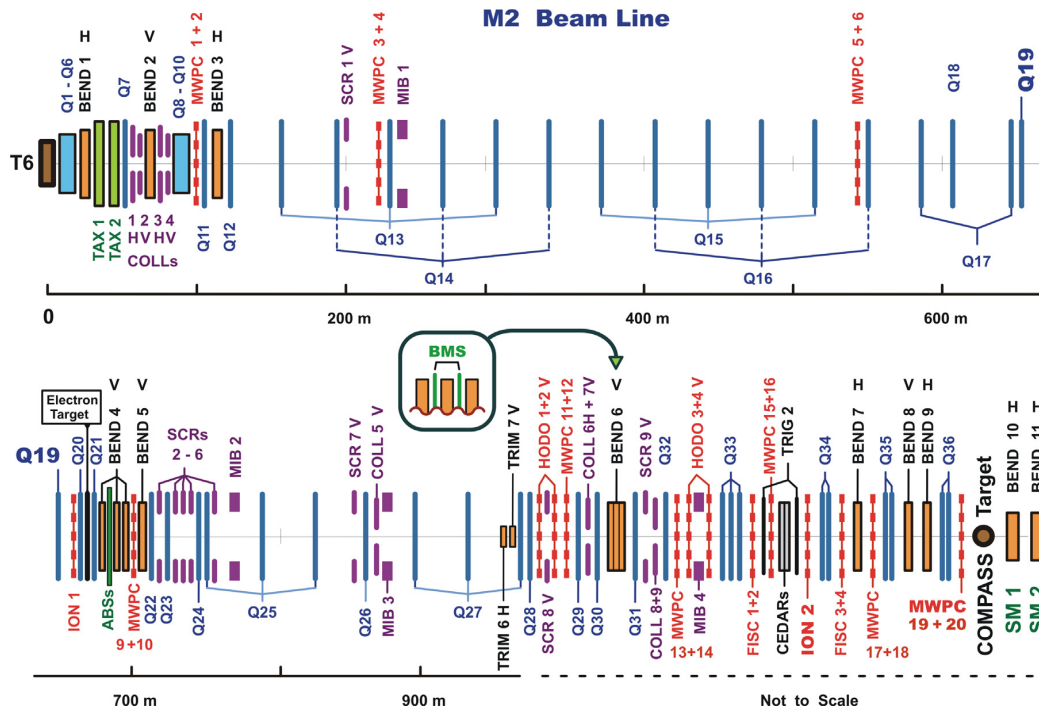
Figure 3.5: The CERN M2 beam line [69].

An angle of the radiation depends on relative speed to the speed of light in a material, in other words, the type of the particle in this case. The lenses and the corrector lead the Cerenkov light on the diaphragm, and if the focus of the light matches to the hole in the diaphragm, PMTs can detect it. One can select a type of particles to be detected by adjusting the pressure of the helium gas.

3.3   Hadron absorber

Many secondary particles as a result of the high-intensity hadron beam affect the detectors downstream the PT. Such detectors are part of the LAS where most of the muons produced in the DY process belong. A hadron absorber with weight of about 23 t was newly installed the spectrometer just downstream the PT to save these detectors.
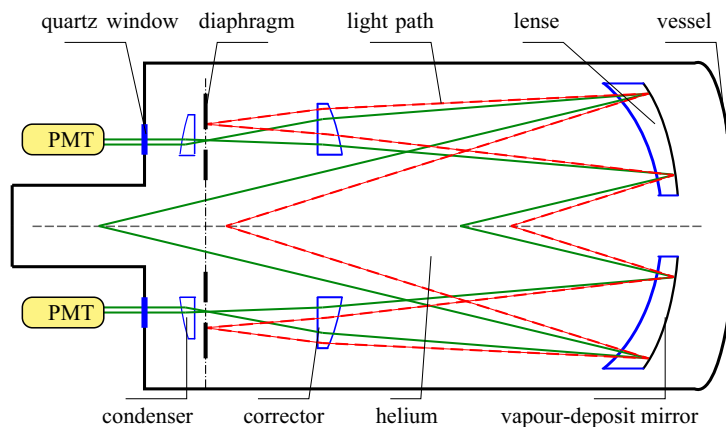
Figure 3.6: A conceptual view of the CEDAR.
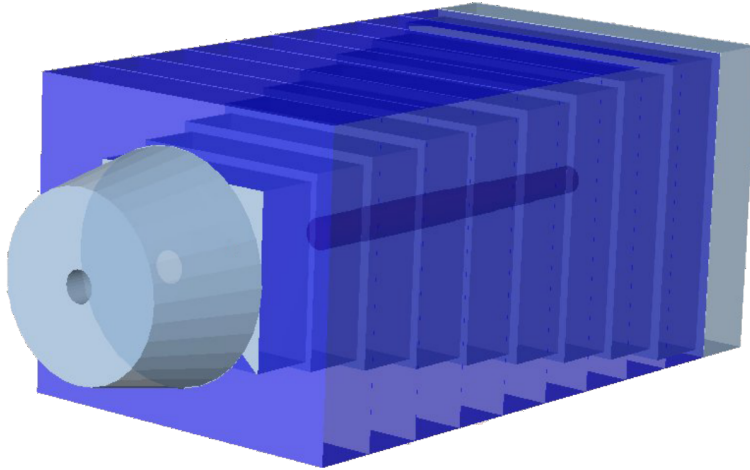
Figure 3.7: A schematic view of the hadron absorber.

The absorber consists of a main part with 120 cm wide, 110 cm high, and 220 cm long, circular truncated cone part (so-called nose), and an additional lithium absorber as shown in Fig. 3.7. Concrete blocks with 20 cm thick surround the main part, and whole structure sits on a concrete platform.

The main part consists of ten blocks with a thickness of 20 cm. The block is composed of a crown to hold a tungsten plug or additional aluminium target, an alumina block, and a stainless steel frame. A rectangular crown made of INOX/aluminium of 8.75^2 cm^2 to 10.25^2 cm^2 with a hole of 8.8 cm to 10 cm in diameter in its centre is placed in the centre of each block except the most downstream part. Nothing is filled in the hole of the crown in the first and the third block from the upstream side to avoid back-scattering of the secondary particles. An aluminium cylinder with 9.5 cm in diameter and 7 cm long was installed to the hole of the second block as an unpolarised target. A tungsten plugs with 20 cm long, and up to 9.5 cm in diameter are installed to the hole in the others. A tungsten of 120 cm long corresponds to about 10.6 in a pion interaction length. Alumina part with a rectangular dimension of from 64×52 cm^2 to 112×102 cm^2 surrounds the crown. A stainless steel frame with outer dimension 120 cm $\times$ 110 cm holds the alumina part. Additional to the ten blocks, three stainless steel plates with 20 cm thick in total were attached on the downstream surface of the main part. Spaces between the plates are adjustable.

A circular truncated cone, which is so-called nose part, made of aluminium is attached to the upstream surface of the main part with 6.37 cm apart for a vertex detector, which will be described in Sec. 3.5.1. A height of the nose is 29.5 cm, and diameters are 55 cm for the narrower side and 65.6 cm for the wider. There is a hole with 10 cm in diameter in the centre of it. This part is inserted to the downstream side of magnets for the PT.

As a result of the pilot run 2014, lower efficiency and wider residuals in only DC0, which is introduced in Sec. 3.5.1, were reported. DC0 is an essential detector for the DY measurement since it covers the large angle. One source of a local background that is not observed in downstream detectors can be gamma rays from a neutron capture at the downstream part of the hadron absorber. Pair production by such gamma rays can affect only the detector which is very close to the hadron absorber. Spallation neutrons are produced by stopping the hadron beam in the absorber. They thermalise and are captured predominately in high atomic number material. Installation of an additional absorber for the neutron was proposed. ^{6}Li was employed for the purpose owing to its high cross-section in the reaction, n + ^{6}Li $\rightarrow$ $^4_2$He + $^3_1$H + 4.7 MeV, of about 940 b.

A new thin lithium absorber and polyethene plate with 1 cm thick were installed for shielding. The lithium absorber consists of four silicon rubber sheets containing Li_2CO_3 and a

Table 3.3: Composition of the Li_2CO_3 sheet and mass ratio of elements. The mass ratio is calculated using a mass ratio of Li_2CO_3 to Si, 30 : 70.

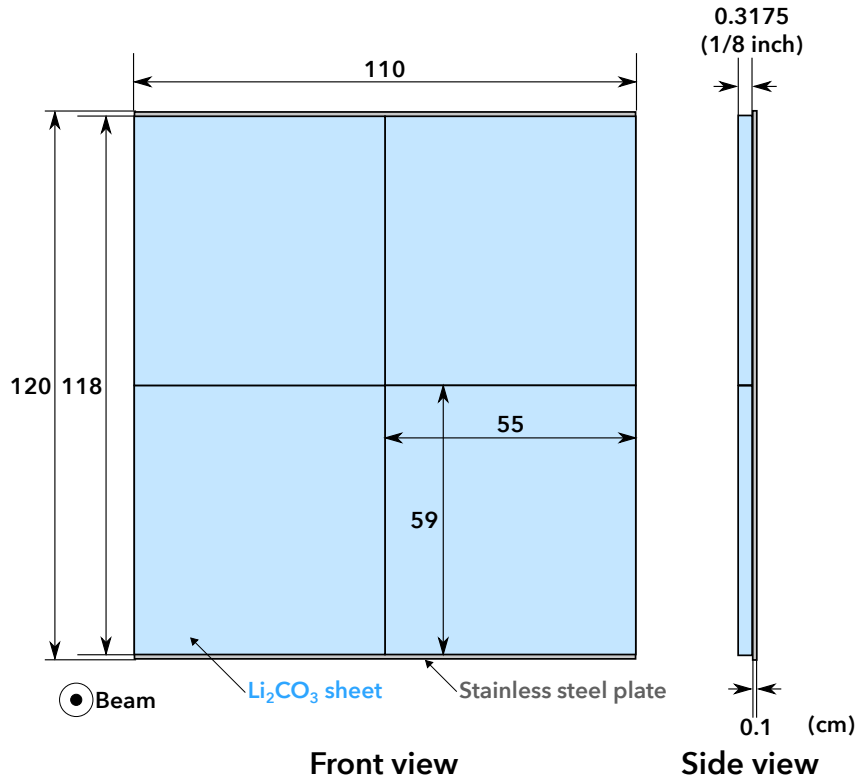|	A	Z	Mass ratio
Li	6.94	3	5.636
C	12.01	6	4.876
O	16.00	8	19.49
Si	28.09	14	70.00

Figure 3.8: Front and side view of the lithium absorber. The Li_2CO_3 sheets are fixed on a stainless steel plate. Dimensions are given in mm.

stainless steel plate. Fig. 3.8 illustrates a geometry of the lithium absorber. 70 % of the sheet in weight is silicon, and the rest is Li_2CO_3. Its density is $1.36\,g/cm^3$, and a size of the sheet is 59 cm high, 55 cm wide and 0.3173 cm[1] thick. Table 3.3 summaries a composition of the sheet and its mass ratio for each element. The lithium absorber was installed upstream the last stainless steel plane of the hadron absorber while the polythene plate was to the downstream side.

3.4 Spectrometer magnets

Two spectrometer magnets were placed on the beamline. The upstream or downstream magnet, called SM1 or SM2, is for LAS or SAS, respectively.

The SM1 is a dipole magnet with a pair of bedstead coils. Its length is 1100 mm, and a horizontal gap of 229 cm and a vertical gap of 152 cm are in the centre. The vertical size of

---

[1] 1/8 inch.
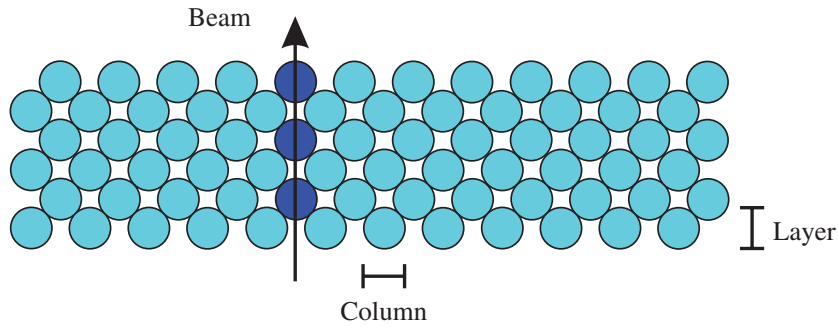
Figure 3.9: A cross-sectional view of a plane of the Scifi detectors [68]. The plane consists of several layers of stacking scintillation fibres. A layer is shifted to a direction perpendicular to the beam with respect to one of the next layer. Fibres in a column are merged into a channel.

the SM1 matched the 180 mrad acceptance of the LAS. A main component of the magnetic field goes from top to bottom, and the strength of the field can be adjusted by changing the height of the central gap. Its bending power 1 T m corresponds to a deflection of 300 mrad at momentum 1 GeV/c [73].

The SM2 is a dipole magnet with a gap of $2 \times 1\,\mathrm{m}^2$ in the middle. Its bending power of 4.4 T m had been measured in the previous experiment, SMC [74]. The bending power corresponds to a horizontal deflection of 7 mrad for a beam with a momentum of 190 GeV/c.

3.5   Tracking detectors

The tracking detectors in the COMPASS spectrometers used in the DY measurement are described.

3.5.1   Large angle spectrometer

Since most of muons from the DY processes are emitted to the large angle region, a tracking by LAS is essential for the DY measurement. For better tracking precision and redundancy, a new station of DC is installed and detectors are updated and maintained.

Scintillating fibre detectors

Scintillating fibre (SciFi) detectors were installed for the beam and muons tracking in upstream region of the spectrometer. One layer is shifted with respect to one of the next layer as illustrated in Fig. 3.9. A group of fibres lined up in the beam direction, which is called column, is treated as the same channel to obtain enough intensity of the scintillation signal. An X projection plane is horizontally sensitive while a Y is vertically sensitive for all stations. Some stations have inclined planes U and V with respect to the X plane. These notations are used for other detectors in this thesis.

Five stations were installed for the DY measurement as summarised in Table 3.4. Three stations FI01, FI15 and FI03 were placed on the upstream side of the PT for beam tracking. They are called the beam telescopes. A U plane of the station FI15 is tilted by 45° with respect to the X plane. A station FI04 was set between the hadron absorber and the SM1 to track dimuons produced in the DY process. Spatial and time resolutions of these stations are about 130 μm and between 350 and 450 ps in one root mean square (RMS). Details of them are described in [75, 76]. A station FI35, so-called vertex detector, was newly built and installed between the main part of the hadron absorber and the nose. The dimuons traverse the hadron absorber, and multiple scattering of the dimuons by the hadron absorber

Table 3.4: A list of SciFi detectors installed for the polarised DY measurement. The dimension of the planes is squared except X', U' and V' of the FI35. Thickness of a station is written in units of radiation length X_0. Only one value is written if parameters are common in the row. Only X, U and V planes are considered for the thickness of the station FI35.

ID	Projection	# of layers	Size (cm^2)	Fibre $\varnothing$ (mm)	Pich (mm)	Ch.	Thickness $(\% X_0)$
01	X, Y	14	3.9^2	0.5	0.41	96	1.6
15	X, Y, U	6	4.2^2	1.0	0.70	64	1.4
03, 04	X, Y, U	21	5.3^2	0.5	0.41	128	3.8
35	X, U, V,	8	$24^2, 16^2, 16^2$	1.0	0.70	320, 224, 224	2.8
	X', U', V'	8	$43, 27, 27$	1.0	0.70	48	

significantly affects tracking and reconstruction of an interaction point. A mission of the vertex detector is measuring points of tracks before multiple scattering by the hadron absorber. The detector has three projection directions X, U and V. The U and V planes are inclined by $+45°$ and $-45°$ to the X plane. Since the nose which should save the vertex detector has an empty hole to suppress back-scattering, the beam and many secondary particles can hit the central region of the detector. A dead zone is needed in the centre region to reduce high hit rate for operation, a staggered design of planes in a projection was employed as illustrated in Fig. 3.10. The idea of the design was that an extension of light guides for channels in a beam region makes a dead zone. By introducing an additional plane with slightly shorter length to the centre to the plane on the dead region recovers inefficient place.

Drift chambers

Four stations of multi-wire drift chambers (DC) were installed around SM1 for tracking; DC0, DC1, DC4 and DC5. Four pair of layers compose each DC. Every second layer is staggered by a half pitch of sensitive wires to minimise a track ambiguities Fig. 3.11.

The DC0 and DC1 [68] with active area $180 \times 127\,cm^2$ were installed upstream of SM1. The U and V planes are inclined by $+20°$ and $-20°$, respectively. The configuration of the detector planes along the beam is Y, Y', X, X', U, U', V, and V'. The plane has 176 sensitive wires of 20 mm diameter with 7 mm pitch. Particle flux at the place of DC0 and DC1 is three times higher than downstream SM1 since particles with low momentum are bent away by the magnet. To stand this high flux environment, a small drift cell size $8 \times 7\,mm^2$ design was employed. Smaller drift cell also gives shorter drift time of electrons which enables us to apply a shorter time window to minimise the number of uncorrelated particles.

A gas mixture of $Ar/C_2H_6/CF_4$ in proportions 45 / 45 / 10 gives a feature of high primary electron rate about 100 per MIP and faster drift velocity $77\,mm\,\mu s^{-1}$. Their spatial resolution is about $190\,\mu m$.

DC4 and DC5 were placed on the downstream SM1. Their basic design is the same as DC0, and the overall dimensions were enlarged to match the angular acceptance downstream the SM1 [69]. The configuration of the planes along the beam is U, U', V, V', X, X', Y, and Y'. Tilts of the U and V planes are $+10°$ and $-10°$, respectively, which are smaller than those of DC0. The sensitive plane consists of 256 wires with a 0.8 mm pitch. Stabilization of temperature of them is crucial since thermal expansion or contraction of their aluminium frame changes the tension of wires and deteriorates their performance. A specific cooling system was installed to minimise such effects. A mixed gas is shared among all the DCs. Their spatial resolution is about $230\,\mu m$.

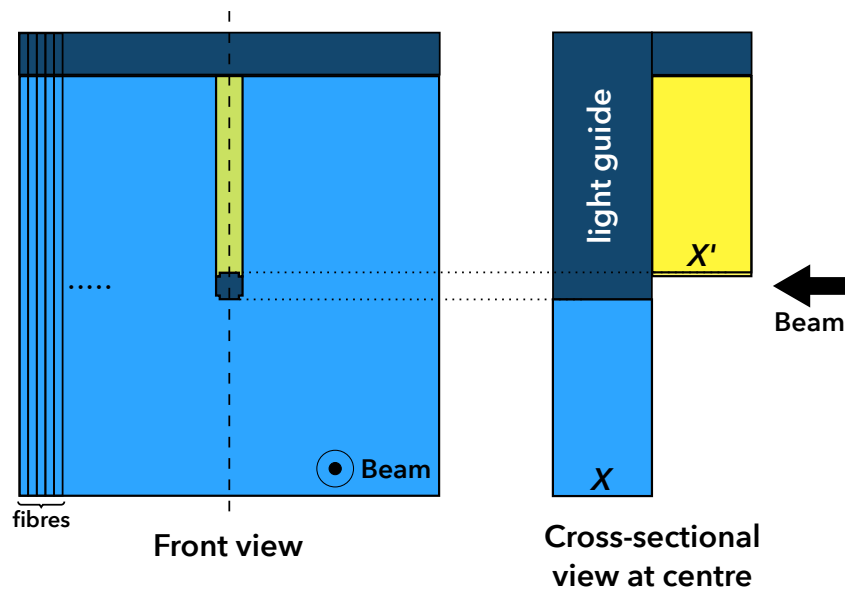**Front view** **Cross-sectional view at centre**

Figure 3.10: Schematic view of X and X' planes of the new vertex detector and its cross-sectional view at its centre. A cross-shaped dead zone at the centre of the detector is produced by stacking X' plane with a slightly shorter length than a half-length of the X plane. Light guide fibres are used for an upper half of the X plane at centre region.
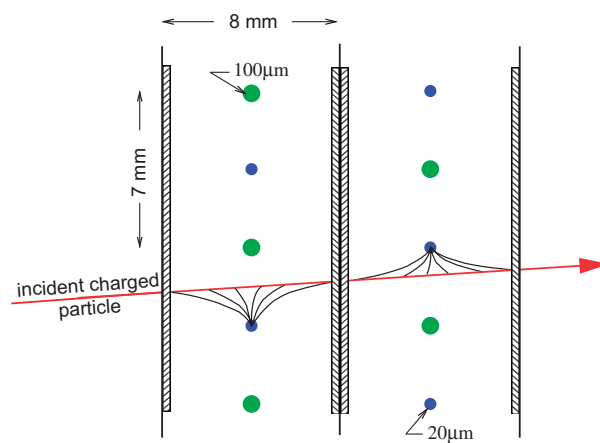

Figure 3.11: A schematic view of a drift cell of the COMPASS drift chamber DC0 and DC1. [68]

DC5 was newly constructed to replace an old detector belonging to LAS while DC4 was installed in 2006. Recovering the old detector was essential to keep high reconstruction efficiency since most of DY events include tracks in LAS. Design of it is almost the same as one of the DC04, and the U and V planes have 32 additional wires on each side to enlarge its acceptance. To prevent DC5 from moving when the SM1 is turned on, it is attached rigidly to the SM1 using a metal rod and an aluminium brace.

Multiwire proportional chamber

Three types of multiwire proportional chambers (MWPCs), named type-A, type-A* and type-B, were installed in LAS and SAS. All layers for all types are characterised by a wire length of about 1 m, a wire diameter of $20\,\mu m$, a wire pitch of 2 mm and an anode/cathode gap of 8 mm. An active area of type-A and type-A* is $178 \times 120\,cm^2$ while one of the type-B is smaller, $178 \times 90\,cm^2$. The type-A has a vertical layer X and two titled layers U and V by $\pm 10.14°$. The type-A* has the same layers as the type-A and an additional horizontal layer Y. The type-B has a vertical layer X and one tilted layer U or V. A dead zone with diameter from 16 mm to 22 mm is in the centre of the chambers. Their spatial resolution was about 1.6 mm. They were operated with a gas mixture of $Ar/CO_2/CF_4$ in proportions 74 / 6 / 20. In total, 21 planes of type-A, four planes of type-A* and nine planes of type-B were used in the run 2015. The details are written in [68].

RICH Wall

The Rich Wall detector with a dimension of $5.27 \times 3.91\,m^2$ which consists of eight planes of mini drift tubes (MDTs) has been operated since 2006 to increase a tracking precision in a large angle region from 150 mrad to 390 mrad on the downstream the RICH detector [69]. The plane consists of eight-cell comb extrusions made of aluminium. One gold-plated tungsten wire with a diameter of $50\,\mu m$ is strung on the centre of the cell with a wire pitch of 10 mm. Fig. 3.12 illustrates a front view of the X plane. There is a hole with a size of $1.02 \times 0.51\,m^2$ in its centre. The X plane comprises 2×12 modules with a length of 3910 mm and 2×12 modules with a length of 1700 mm. A Y plane consists of 2×12 modules with a length of 3910 mm and 2×12 modules with a length of 1700 mm. A mixture of Ar/CO_2 in proportions 70 / 30 is used. A spatial resolution of the order of 1.0 mm is achieved by operating the detector in a drift mode with a high voltage of 2050 V.

Straw tube chamber

Two stations of a straw drift tube chamber with an active area of $9\,m^2$ are installed on the downstream SM1 for tracking charged particles in a large scattering angle from 15 mrad to 200 mrad. The station #3 is set between the DC5 and the RICH while a station #5 is installed between the SM2 and the W45 drift chamber that will be described in Sec. 3.5.2. Six planes X1, X2, Y1, Y2, U, and V of the station #3 and three planes X1, Y2, and U of the station #5 are used for tracking of the DY data. The U and V planes are tilted by 10° and $-10°$ with respect to the X planes, respectively. The plane can be divided into three sections A, B, and C as shown in Fig. 3.13. The B section is composed of 190 long tubes and 64 short tubes to form a physical hole of about $20^2\,cm^2$ because of an exposure of higher rate. The A and C sections consist of 96 tubes. The plane consists of double layers of straw tubes. A gold-plated tungsten wire with a diameter of $30\,\mu m$ is strung in the centre of the tube. The tubes are stacked and form the double layers by glueing together. A mixture of $Ar/CO_2/CF_4$ in proportions 74 / 6 / 20 is used. A spatial resolution of this detector is about $200\,\mu m$. The details of this chamber are found in [77].
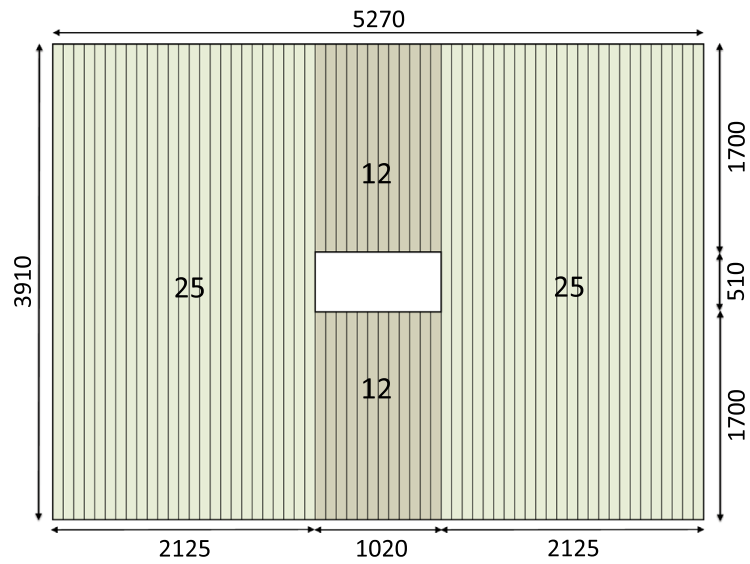
Figure 3.12: Front view of an X-plane of the Rich Wall detector [69]. The large-size numbers correspond to the number of mini drift tubes modules in each sector, the small numbers indicate the dimensions in units of mm.
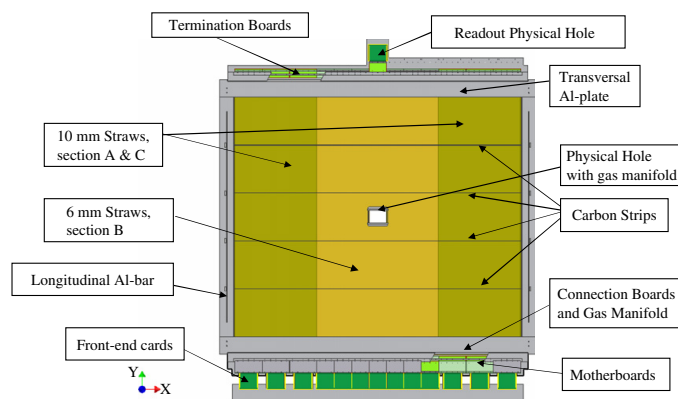

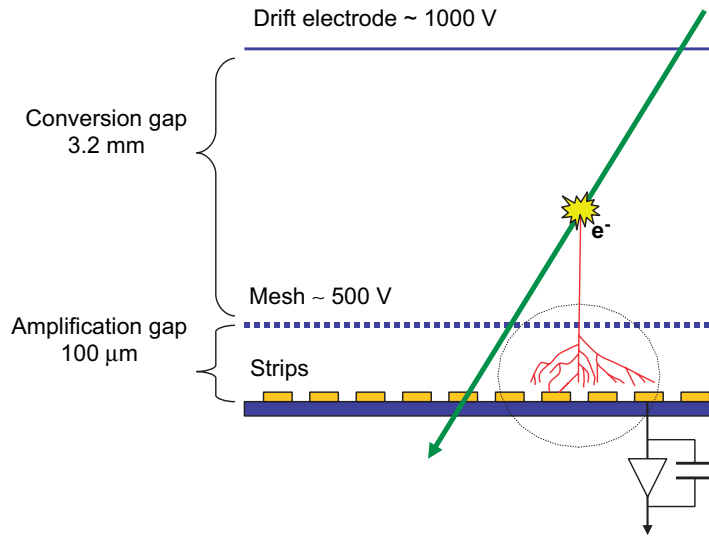Figure 3.13: Schematic view of a plane of the straw chamber [77].

Figure 3.14: Principle of a Micromegas detector [68].

3.5.2 Small angle spectrometer

SAS starts from the SM2 and covers the small angle region. Micromesh gaseous structure detectors (Micromegas), a large drift chamber, so-called W45 and a gas electron multiplier (GEM) compose this tracking system.

Micromegas

Micromegas is a kind of a gaseous particle detector using a metallic micromesh as an electrode for a gas amplification. The COMPASS is the first experiment which uses Micromegas for a high energy physics experiment [78–80].

Fig. 3.14 illustrates a principle of the Micromegas. A metallic micromesh separates a volume filled with a specific gas between a parallel plate electrode structure and a set of parallel microstrips into two: a conversion gap with 3.2 mm thick and the amplification gap with 100 µm. A voltage of about 1000 V is applied to the electrode structure and of about 500 V to the mesh while the microstrips are earthed.

Electrons of pairs of electron/ion produced by an ionizing radiation drift to the mesh in an electric field about $1\,\mathrm{kV\,cm^{-1}}$ over 3.2 mm. An avalanche is produced in an amplification gap with an electric field about $50\,\mathrm{kV\,cm^{-1}}$ over 100 µm by the electrons from the conversion gap. The ions drift to the microstrips over at most 100 µm, and a signal is read from the strip. Widths of the signal cannot exceed drift time that the ions travel over the maximum distance, about 100 ns.

Three stations of the Micromegas with four planes of X, Y, U and V are installed to the spectrometer. The U and V plane are titled by $\pm 45°$ with respect to the X plane. Each detector has an active area of $40 \times 40\,\mathrm{cm}^2$ with a dead zone of 5 cm in diameter. A pitch of the strip is 360 µm for 512 strips in the central part of the plane and 420 µm for 256×2 strips in the outer parts. Spatial and time resolutions are about 100 µm and 5 ns, respectively. A mixture of $\mathrm{Ne/C_2H_6/CF_4}$ in proportions 80 / 10 / 10 is used for good time resolution. All the Micromegas were upgraded to have a pixelated region on its centre in 2015 run. However, a merit of the improvement is not great for the DY measurement due to its very small angle coverage.
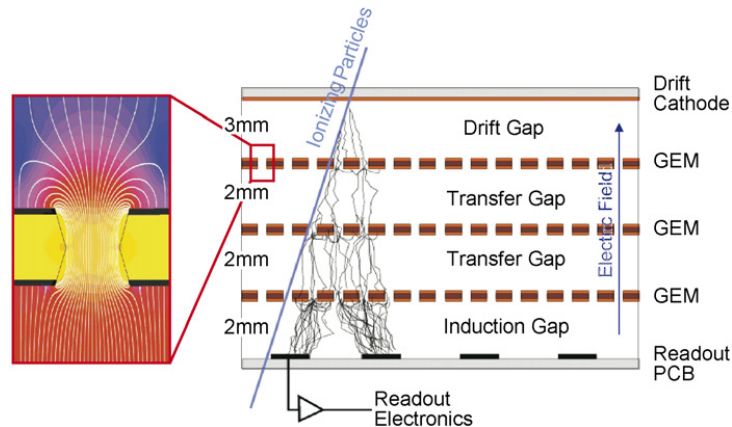
Figure 3.15: Schematic cross-section of the GEM detector in COMPASS [68]. The sketch on the left side is the electric field configuration for typical GEM voltages.

W45

The W45 system is the large drift chambers placed between the SM2 and the ECAL2. The W45 drift chambers got their name when they were used for the first time by the EMC at CERN. After that, the chambers have been used by the NMC, the SMC and the COMPASS presently with several refurbishment.

Six chambers with an active area of $5 \times 2.5 \, \text{m}^2$ are used. Each chamber consists of two pairs of readout planes with up to 144 wires per plane. Some planes are X/Y projections, some are stereo planes U/V, where the wires are inclined by 30° from the vertical direction. A size of a dead zone in the centre of the plane is 0.5 or 1.0 m depending on the station. A mixture of $Ar/CF_4/CO_2$ in proportions 85 / 10 / 5 is used to increase the drift velocity, which is important for efficient track reconstruction. Spatial resolution is about 600 μm.

Gas electron multiplier (GEM) and pixel GEM

GEM [81] is an amplification technique for a position detection of an ionising radiation. COMPASS is the first high-luminosity particle physics experiment to employ gaseous micropattern detectors with amplification in GEM foils only [68].

Fig. 3.15 shows a schematic cross-section of the GEM detector used in COMPASS. The GEM consists of a polyamide foils of 50 μm thick with copper coating on both sides, a drift cathode and a readout anode. The GEM foil has a large number of micro-holes with 70 μm and a number density of $10^4 \, \text{holes/cm}^2$, and suitable potential between both sides is applied. A primary electron produced by an ionising radiation in a drift gap drifts to the GEM foil. When the primary electron goes through a micro-hole on the GEM foil, an avalanche is created due to a high gradient of an electric field as shown in the left side of Fig. 3.15. An amplification level can be changed by changing a number of the GEM layers, in the case of ones for COMPASS, triple stages design is employed. A review of operating principles and applications is introduced in [82].

Ten stations of the GEM with an active area $31^2 \, \text{cm}^2$ are used in the run 2015. A station consists of two GEM detectors with a different projection. To avoid too high occupancies on the central strips, circular region of 5 cm is deactivated during a physics run with a high-intensity beam by decreasing the potential difference across the last GEM foil. A mixture of Ar/CO_2 in proportions 70 / 30 is used to obtain a large drift velocity, low diffusion, non-flammability and non-polymerising properties. A spatial resolution of the GEMs is about 80 μm.
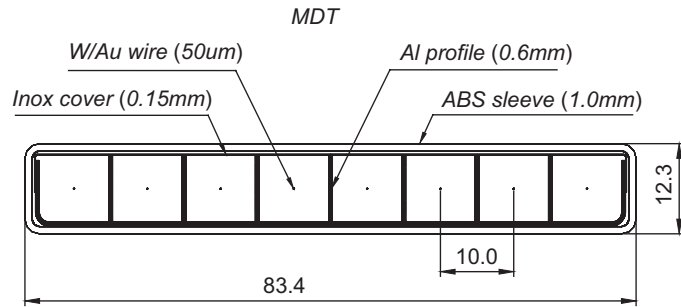
Figure 3.16: A cross-sectional view of the mini drift tube of the MW1 [68].
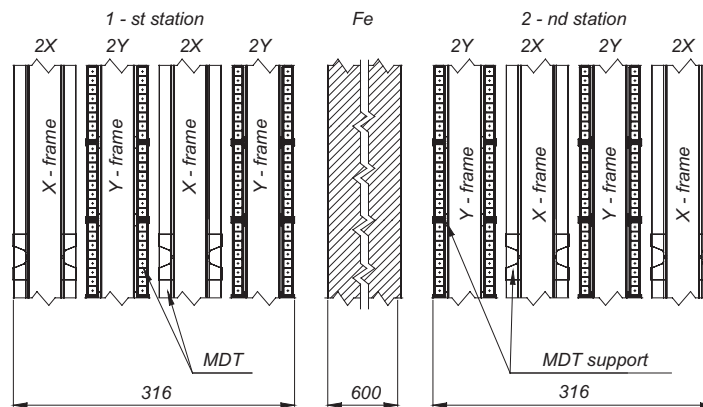
Figure 3.17: Schematic cross-sectional side view of MW1. All dimensions are given in millimetres. Vertically only part of the stations are shown [68].

Two stages of a pixelized GEM are also installed the spectrometer [69, 83]. However, they do not take important role in the DY measurement due to its very small angle coverage.

3.6 Muon identification

A muon identification is essential for the DY measurement. Two systems, so-called muon wall (MW), composed by several detector planes and an absorber are installed to the LAS and SAS spectrometers, respectively.

3.6.1 MW1

The MW1 is composed of two stations of MDTs and an absorber made of iron with 60 cm thick, so-called Muon Filter1 [68]. The MW1 is placed between the RICH and the SM2 and works for a track detected in LAS. An MDT module has an eight-cell comb extrusion with a wall thickness 0.6 mm made of aluminium (Fig. 3.16). Gold plated tungsten wires with 50 μm diameter strung in the centre with a wire pitch of 10 mm and glued to polyethene plastic spacers. The modules are filled with a mixture of Ar/CO_2 with proportions 70 / 30 for a short drift time, a good ageing feature, non-flammable and a reasonable cost. Fig. 3.17 shows side view of the MW1. Four planes of double layers of MDTs with an active area of $4845 \times 4050\,cm^2$ for an X projection and $4730 \times 4165\,cm^2$ for a Y projection forms a station. The planes have a hole of about $150 \times 800\,cm^2$ in their centre. The total number of MST modules in the system is 1056.
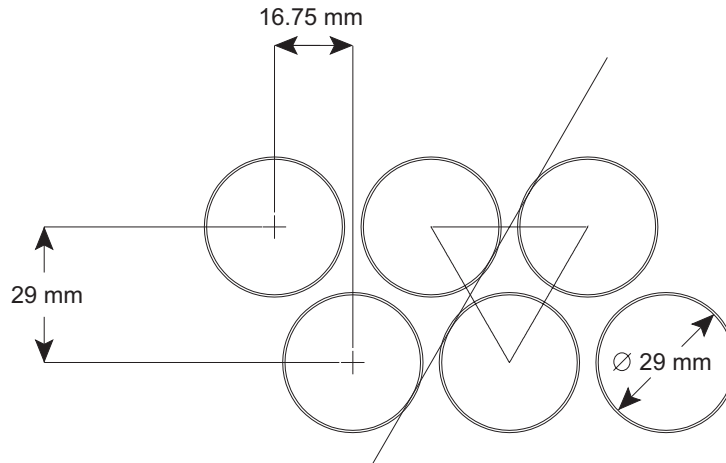
Figure 3.18: The tube layout in a double layer of the MW2 planes [68].

3.6.2 MW2

The MW2 consists of two stations based on drift tubes and a 2.4 m concrete absorber. The concrete absorber is placed on the upstream side of the two stations by about 5 m. A station with a dimension of $447 \times 202\,\text{cm}^2$ has a six double layers in X, Y and V which is inclined by $-15°$ with respect to the vertical projections. Drift tubes made of stainless steel with an inner diameter of 29 mm and a wall thickness 0.5 mm is inserted into precise guide holes in the frame and fixed with a clamp. A gold-plated tungsten anode wire with 50 μm in diameter is strung in the centre of the drift tube. A pitch of the wires is 33.5 mm. Each plane has a hole with a rectangular dimension of $1 \times 0.8\,\text{m}^2$. The hole is covered by the MWPB-B (Sec. 3.5.1) with some overlap. A mixture of Ar/CH_4 with proportions 75 / 25 is used for a fast drift speed, a broad working plateau and stable performance.

3.7 Trigger system

The trigger system has to fulfil several requirements: selecting event candidates in a high rate environment within a 500 ns with a minimum dead time, providing the start of the data acquisition, generating strobes for gating some of the analogue-to-digital converters (ADC) and triggering the readout of detectors and front-end electronics. The general design of the trigger system is aimed at a high selectivity and a high efficiency for the selected event types. The number of usable triggers is limited by the speed of the transfer to the central data acquisition system of about 30 MB/s. An exact event timing is needed to attach beam and outgoing muon track candidates to the event in a unique way. The system is based on fast hodoscope signals, energy deposits in calorimeters and a veto system. The hodoscope system is subdivided into some multi-element modules with different sizes and positions along the beam axis depending on a type of the beam and kinematics of the reactions. General concepts and details of the trigger system is described in [68, 84, 85]. Since signals from the calorimeters are not used to find event candidates of the DY process, the hodoscope system and the veto system are described.

In the DY measurement, three hodoscopes, a large angle spectrometer trigger (LAST) hodoscopes, an outer trigger (OT) hodoscopes and middle trigger (MT) hodoscopes, were employed to select a muon for a dimuon event candidates. Since most of DY events include LAS, three types of the combination were made: LAST-LAST, LAST-OT and LAST-MT. Fig. 3.2 illustrates a position of trigger hodoscopes. LAST hodoscopes consist of three groups of 32 scintillators: HG01Y1, HG02Y2 and HG02Y2. The LAST hodoscope system was designed
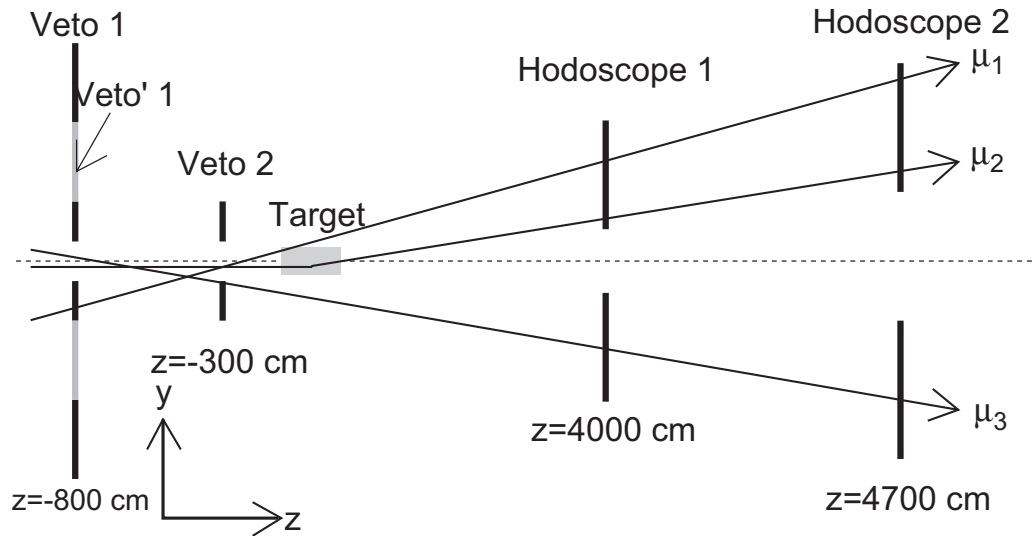
Figure 3.19: Schematic layout of the veto system [85]. The tracks μ_1 and μ_3 are vetoed, whereas the track μ_2 satisfies the inclusive trigger condition.

to enable triggering on dimuons. In addition for triggering on dimuons, two horizontal scintillator hodoscopes of the LAST measure an angle of a muon projected on the non-bending plane and check a compatibility that the dimuon is originated from the target position or not. The LAST can detect a muon with the laboratory polar angle from 25 mrad to 160 mrad. OT hodoscopes consist of three group of scintillators, HO03Y1, HO04Y1 and HO04Y2, while four stations HM04 and HM05 compose the MT. A muon with the laboratory polar angle from 8 mrad to 45 mrad is detected by OT or MT.

Many triggers in the hodoscope systems are caused by muons not interacting in the target due to a muon halo of the beam and a decay of the beam particle into a muon. A layout of the veto system is shown in Fig. 3.19. Two stations VI01 and VI02 are for a rejection of a near halo of a beam. They have an inactive region with 4 cm diameter hole. The first larger detector VI01 is for a rejection of a near halo and located on about 10 cm downstream of the FI01 and the second one is installed between the FI15 and FI03. A VO01 is a veto station for far halo rejection and is set between the VI01 and the FI15.

3.8 Data acquisition system

The data acquisition (DAQ) system needs to treat about $250,000$ detector channels with a typical event size of 35 kB and trigger rate of about 30 kHz during the spill time. Fig. 3.20 shows an overview of a data flow of the COMPASS DAQ system. Analogue outputs from the detectors are digitised and buffered in ADC or TDC modules. A trigger control system (TCS) synchronises the digitising and readout units. Readout modules CATCH[2] and GeSiCA[3] receive the trigger signal from the TCS and transferred to read-out buffers via fast links and then stored to spill buffer cards during the spill time. Data is sent to an event builders via Gigabit Ethernet switches during no spill. The sub-events are combined to build the full events. The events are then transferred to the CERN data centre and stored on tape at the CERN Advanced Storage System (CASTOR). The stored data is called "raw" and needs to be reconstructed to obtain useful information in a physics analysis.

---

[2] **COMPASS** textbfAccumulate, textbfTransfer and textbfControl textbfHardware

[3] textbfGEM and textbfSilicon textbfControl and textbfAcquisition
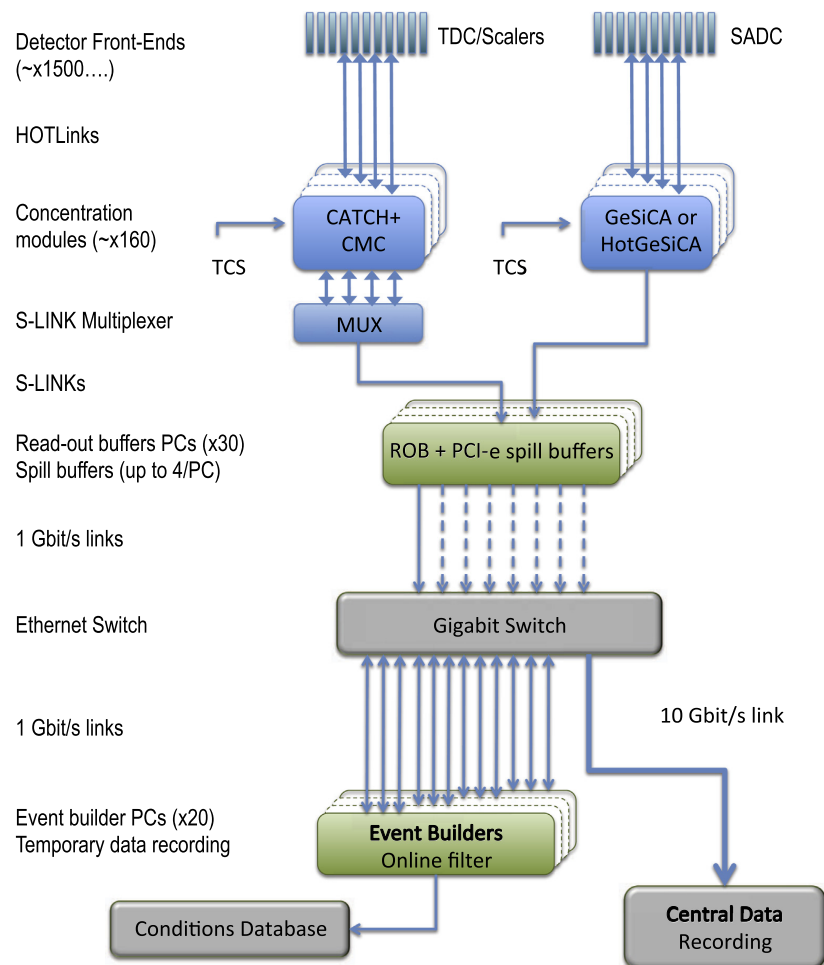
Figure 3.20: Overview of the COMPASS DAQ system [69]. Data coming from the detectors are first digitised in the front-end cards and then merged in the concentrator modules, either CATCH or GeSiCA (HotGeSiCA). The data from the concentrator modules are first sent to the readout buffers and then transmitted to the event builders. The data are temporarily saved on disk, before being migrated to the central data recording facility.

3.9 Data reconstruction and analysis processes

A reconstruction process finds and reconstructs information about hits on detectors, tracks, particles and vertices from the raw data. The COMPASS reconstruction and analysis program (CORAL) [86] performs the reconstruction process.

At the first step of the reconstruction process, the raw data is decoded and transformed into time information and signal amplitudes of the detectors as shown in Fig. 3.21. In the next step, which is called clustering, the hits of channels that are fired by the same particle are grouped. The hit clusters that belong to some detectors have information about an energy loss of a track penetrating the detector. Event reconstruction is performed using the hit clusters. At first, the process finds straight line segments of hit clusters in no strong magnetic field region using a special Kalman filer algorithm [87]. Moreover then, the straight segments are bridged over a region with strong magnetic field. A fast loop up table for the bending in the field (dicofit) is used for the bridging. Tagging of a beam track and a muon identification is performed. A beam track is defined as a track with at least seven hits on the beam telescopes. A track which crosses more than 30 radiation lengths between the first and the last measured points is identified as a muon. Here, since the vertex detector is not used in the event reconstruction, the hadron absorber is not considered in the calculation of the radiation length. At last, the reconstructed tracks are extrapolated to the target region for a vertex search. A vertex with a beam particle is tagged as a primary vertex. Information on the events, a momentum vector, a charge, information about the first and the last hits, and a radiation length of a track, is stored in a mini data summary tape (mDST). χ^2s of the track and vertex in the fittings for the reconstructions are also recorded.

In the case of data produced by Monte-Carlo (MC) simulation, the reconstruction process replaces the decoding to a digitisation process. In the clustering, a specific simulation for each detector is carried out to remove hits with small energy deposit and to smear hit information using position and time resolution of the detector. Hits on the detectors are produced from the hits made by MC and the same reconstruction procedure as one for the real data is performed. Both information on reconstructed events and generated events by MC are saved into a mDST.

PHAST (PHysics Analysis Software and Tools) [88] provides a dedicated framework for analysis of mDSTs. Users can access information on the reconstructed tracks, particles, vertices, a polarisation of the PT and so on event by event.
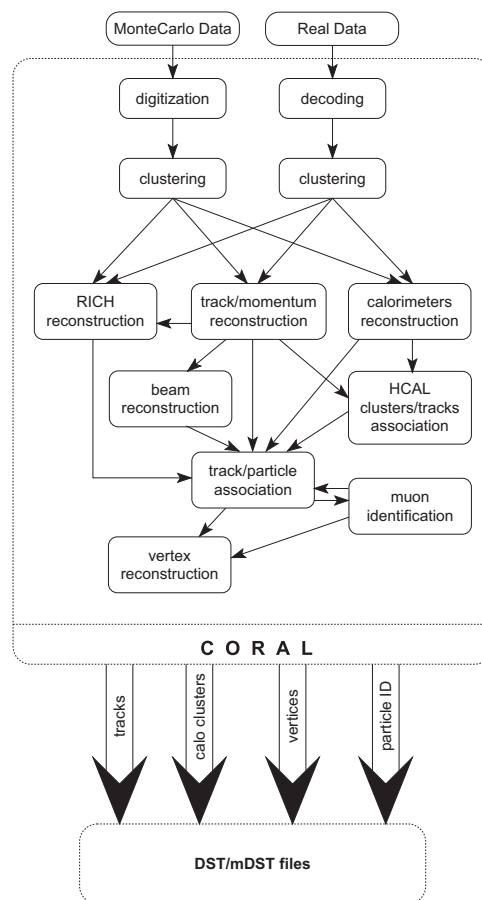
Figure 3.21: Sketch of processes of the COMPASS reconstruction software [68].

Chapter 4

The COMPASS polarised target

One of the vital equipment in the COMPASS is the PT system. The system consists of a cryostat, solenoid and dipole magnets, a microwave (MW) system and a polarisation measurement system using the principle of nuclear magnetic resonance (NMR). Hydrogen nuclei in solid ammonia which contains paramagnetic centres as a result of an electron beam irradiation are polarised by dynamic nuclear polarisation (DNP) technique in a 2.5 T solenoid magnetic field along the beam direction. The polarisation is build up for about 24 h, and the direction of the polarisation is changed to the transverse direction with respect to the beam by so-called field rotation with the solenoid and dipole magnetic field. The polarisation is kept only by 0.6 T of the dipole magnetic field which is transverse to the beam direction during the physics data taking. The polarisation is measured before and after the field rotation at 2.5 T. Polarisation is interpolated in time axis using a principle of a relaxation and in beam axis using "Zig-Zag " method described below. For the physics analysis, polarisation averaged over both a data taking period and target cells is used. Finally, A cleaning operation of the target material for the next DY data taking in 2018 is described.

4.1 Principle of a polarised solid target

Polarisation of protons, which have spin $1/2$, is defined as follows:

$$P = \frac{N^+ - N^-}{N^+ + N^-}, \tag{4.1}$$

where $N^{\pm}$ is the number of protons whose spin is parallel or antiparallel to a quantisation axis. Boltzmann distribution can describe a distribution of $N^{\pm}$ at thermal equilibrium (TE):

$$N^{\pm} = \exp\left(\frac{\pm\mu B}{k_B T}\right), \tag{4.2}$$

where μ is the proton magnetic moment, k_B is the Boltzmann constant, T is an absolute temperature and B is an intensity of an external magnetic field. By substituting Eq. (4.2) to Eq. (4.1), the polarisation at TE is

$$P = \tanh\left(\frac{\mu B}{k_B T}\right). \tag{4.3}$$

If $(\mu B)/(k_B T) \ll 1$ is satisfied, a typical condition of COMPASS PT 0.1 K and 2.5 T can, the relation is approximated to:

$$P \approx \frac{\mu B}{k_B T}. \tag{4.4}$$

Therefore even such a low temperature and a high magnetic field can provide only 1 % of the proton polarisation. In the case of electron polarisation, it is almost 100 % since its magnetic moment of the electron is 1000 times larger than that of the proton. The DNP technique is key solution to achieve a high proton polarisation.
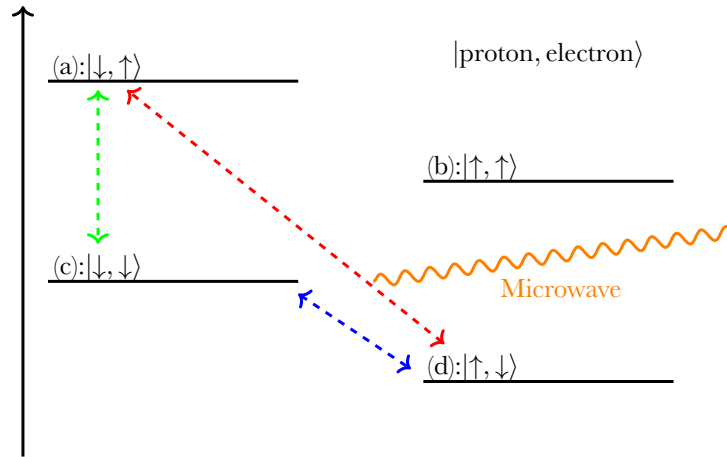
Figure 4.1: A diagram of energy levels of a proton and free electron pair in external magnetic field. The bra-kets indicate the spin state of the pair. The pair can be at four energy levels depending on their spin state. For example, pairs in (d) state can be excited by MW. irradiation indicated by a red arrow. The exited pairs are relaxed to (c) and (d) (a green and blue lines).

Solid effect ([89–91]) is one of a model to explain the DNP technique (Fig. 4.1). Considering a pair of a proton and a free electron in the external magnetic field, an energy level of the pair is split into four levels depending on spin orientations of the particles. For example, pairs in the (d) state can be excited to the (a) state by irradiation of microwave (MW) with a frequency corresponding to the energy difference between the (a) and the (d). The excited pairs are relaxed as time passes. Since a relaxation time of the proton is about 1000 times longer than that of electron due to their magnetic moments, the excited pairs in (a) are relaxed to (c) at first and then (d). Negative polarisation of the proton is achieved as a result of the increase in the number of pairs in the (c) state. Positive polarisation can be achieved by an irradiation of MW with the the energy corresponding to the energy difference between (b) and (c).

4.2   Target material and target cell

This section offers a selection of the target material ammonia (NH_3), a production of the solid ammonia. To place the target material on the beamline stably, target cells which hold the target material are installed. A feature and whole structure of the cells are also introduced.

4.2.1   Target material

Solid ammonia was used as the polarised proton target material. A dilution factor f is a ratio of the number of polarisable particles to the total number of particles. In the case of ammonia as a polarised proton target, its dilution factor is 0.176. In physics analysis, the dilution factor is obtained by weighting the numbers of particles with differential cross-sections of interest, as described in Sec. 5.7.

Ammonia beads were produced by crushing a large bulk of ammonia. A typical size of the beads are about 0.5 mm in diameter and the density at the liquid nitrogen temperature 77 K is 0.853 g/cm^3 [92]. The ammonia beads were irradiated with 20 MeV electrons at the Bonn linac in 2011 to introduce paramagnetic centres with a density of 10^{-4} to 10^{-3} per proton. Since solid ammonia melts at 195 K, the material has been stored in liquid nitrogen, and any operations which will be described were performed in liquid nitrogen environment.
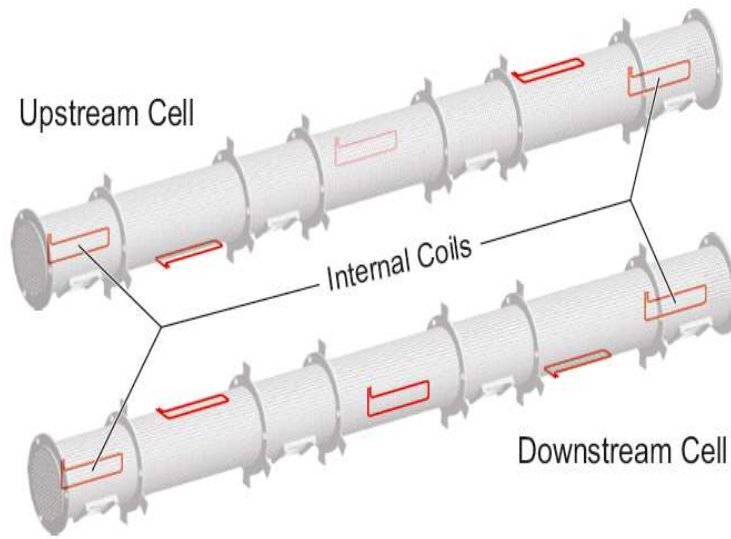
Figure 4.2: The target cells [93]. Red lines draw NMR coils. Three and two coils are placed outside and inside each cell, respectively.

4.2.2 Target cell

A target cell holds the target material on the beamline stably. In the previous COMPASS runs, target cells made of polyamide had been used. Since the cell material contains hydrogen nuclei which cannot be polarised by DNP, the cells induced background about 30 % background in the polarisation estimation. To reduce it, we introduced new target cells made of polychlorotrifluoroethylene (PCTFE, $(C_2F_3Cl)_n$) which does not contain the hydrogen nuclei.

The target cell (Fig. 4.2) consists of four short cylindrical pieces, three long cylindrical pieces, two caps for both ends of the cell, and four caps for loading holes. The short and the long pieces are aligned alternately and connected by three screws made of PCTFE. The two caps close both ends of the structure. There is a hole with a diameter of 2 cm on the side of the short pieces for the material loading as described below. The caps close the loading holes after the loading. The designed length of the target cell was 550 mm, outer diameter was 41.6 mm, and inner diameter was 40.0 mm. A coil made with a stainless steel wire with rectangular dimension 5 cm × 1 cm picks NMR of hydrogen nuclei up to measure a polarisation of the target. Five NMR coils were installed to each target cell. Three coils were fixed on the outside surface of the cell, while two inner coils were placed in the beam spot inside the cell. The installation of the inner coils were the first attempt in COMPASS because possibility that a large amount of heat introduced by the high-intensity hadron beam affects the polarisation had been pointed out. An important role of the inner coils in addition to the polarisation measurement were monitoring an effect of the beam to the polarisation. PCTFE foils with 50 µm thickness wrapped the inner coils to prevent the target material from touching them.

Two target cells were aligned longitudinally with 20 cm separation. The cell, which faces the beam first, is called the upstream cell, while the other is the downstream cell. The NMR coils were numbered from 1 to 10 along the beamline for identification (Fig. 4.3). Two MW stoppers made of copper and three carbon coated honeycomb-grid paper were placed between the target cells. Two ruthenium oxide thermometers were installed on the downstream cell. Speer resistors made of carbon were set to each cell and one of the MW stopper to monitor power of absorbed MW for each cell.
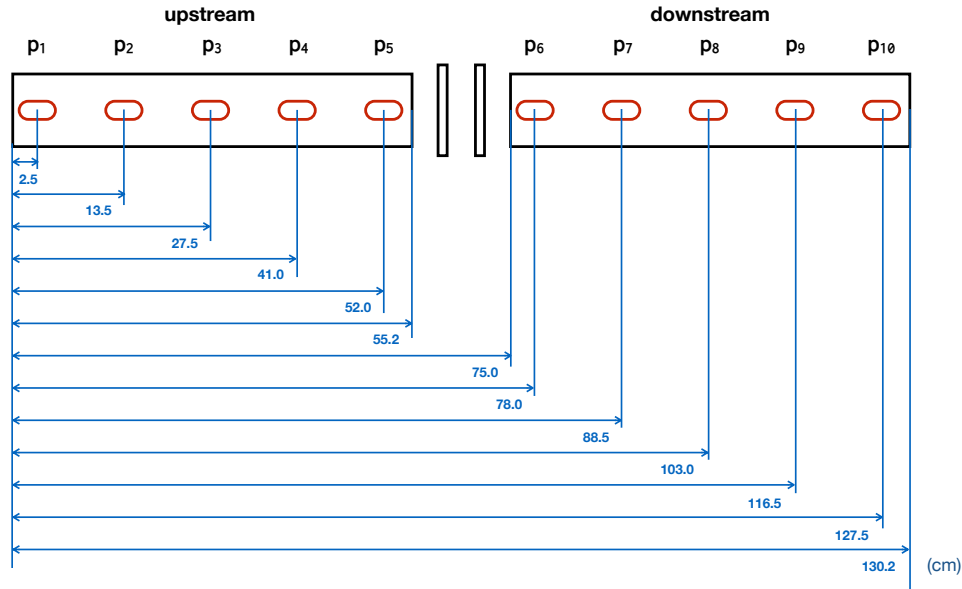
Figure 4.3: A schematic view of a position of NMR coils. Two long boxes indicate target cells. Ten red circles indicate NMR coils. Distance from the upstream edge of the upstream cell and centre of NMR coils are shown in cm.

The two target cells and MW stoppers were fixed to three kevlar tube with STYCAST [1]. A long tube made of CuNi having 40 holes on its side was set on the bottom of the structure for ^{3}He/^{4}He supply. The holes were denser on the downstream side to supply of ^{3}He in the mixing chamber, which will be introduced in Sec. 4.3.1, uniformly. A kevlar tube with 1363 mm long, and 71.5 mm in diameter contained the structure and which was connected to a target holder. The kevlar tube had eight holes on the bottom for an ammonia loading. A centre part of the kevlar tube, which the MW stoppers are in, is coated with a carbon paint for MW absorption.

4.3   PT system

The COMPASS PT system consists of a cryogenic system, a microwave system, two superconducting magnets and a polarisation measurement system. The target material in a mixing chamber is cooled down to ultra-low temperature about 70 mK using ^{3}He/^{4}He dilution technique. The target is polarised using DNP technique longitudinally to the beam under the 2.5 T magnetic field by feeding a microwave, provided from a dedicated system. After polarisation build-up for about 24 hours, the cryostat is operated in the so-called "frozen spin mode" by stopping MW and decreasing a flow of ^{3}He/^{4}He to cool the target material down to about 70 mK. The direction of the polarisation is rotated from longitudinal to transverse by the solenoid and dipole magnetic fields. The longitudinal and transverse direction are defined by the beam direction. A polarization of the target is determined by measuring NMR with the 2.5 T solenoid magnetic filed. For the physics data taking period with the transverse polarization kept with the 0.6 T dipole magnetic filed only, a polarization cannot be monitored but interpolated from the measured polarization values before and after the rotation. since polarisation measurement system is optimised to measure polarisation precisely in the solenoid magnetic field.

---

[1]STYCAST® is a two-part epoxy glue for low temperature with very high thermal conductivity and excellent electrical insulation produced by Henkel.
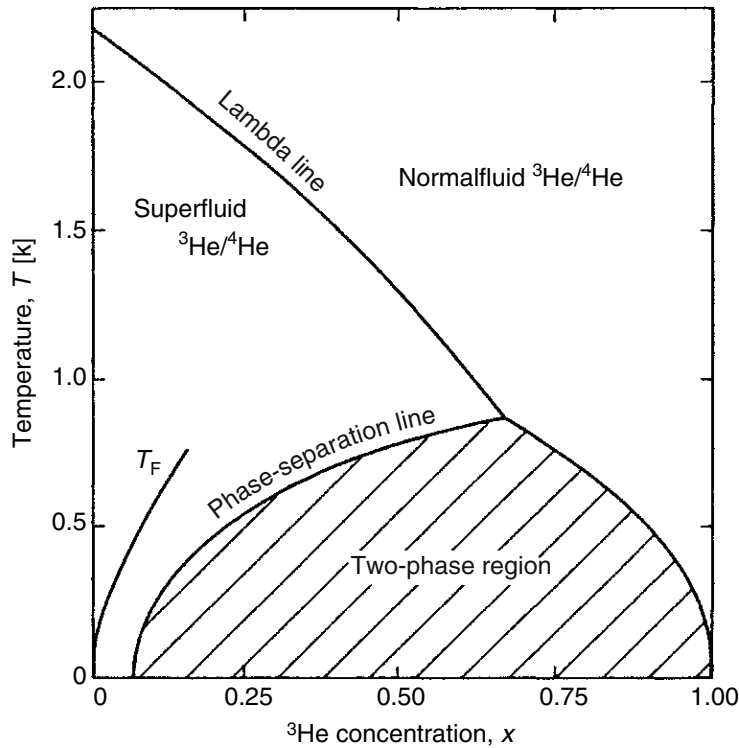
Figure 4.4: A phase diagram of ^{3}He/^{4}He mixture [94]. A phase of ^{3}He/^{4}He mixture is separated blow the lambda point at a temperature of 0.867 K.

4.3.1 Cryogenics

The dilution cryostat consists of a ^{4}He system and a ^{3}He/^{4}He system as shown in Fig. 4.5. ^{3}He/^{4}He dilution technique is the only method to achieve ultra-low temperature below 100 mK continually. Furthermore, the technique can provide a high cooling power typically 100 mW at 200 mK to 300 mK that is needed to remove heat from MW for DNP.

Fig. 4.4 show a phase diagram of ^{3}He/^{4}He mixture at low temperature. ^{3}He/^{4}He at the temperature below the lambda point of 0.867 K separates into a ^{3}He rich phase and a poor phase [94]. The shaded region in the figure is a non-accessible range for ^{3}He/^{4}He mixtures. The ^{3}He rich phase floats on top of the ^{3}He poor phase due to the difference of their densities. Since a saturated vapour pressure of ^{3}He is roughly 100 time higher than that of ^{4}He [95], ^{3}He in the poor phase can be removed by pumping. The equilibrium of this system is restored by dilution of ^{3}He in the rich phase to the poor. The dilution causes high cooling effect, and the effect is called ^{3}He/^{4}He dilution cooling. The ^{4}He system cools ^{3}He/^{4}He gas from room temperature to about 1 K. The cooled ^{3}He/^{4}He is provided to a mixing chamber and the still for the dilution cooling. Vacuum pumps and gas traps are used to control flow and purity of the ^{3}He/^{4}He gas.

^{4}He system

Liquid ^{4}He is supplied from a buffer dewar to the separator. The temperature of the separator is about 4.2 K which is the boiling point of ^{4}He at atmospheric pressure. Some amount of liquid ^{4}He evaporates on the way from the dewar to the separator. Consequently, gas and liquid phases exist in the separator, and liquid the ^{4}He is supplied to the evaporator through heat exchangers. The evaporator is cooled down to 1.4 K by pumping ^{4}He with Sogevac SV630 rotary pump and Leybold RUVAC 2001 roots blower. A flow from the evaporator is
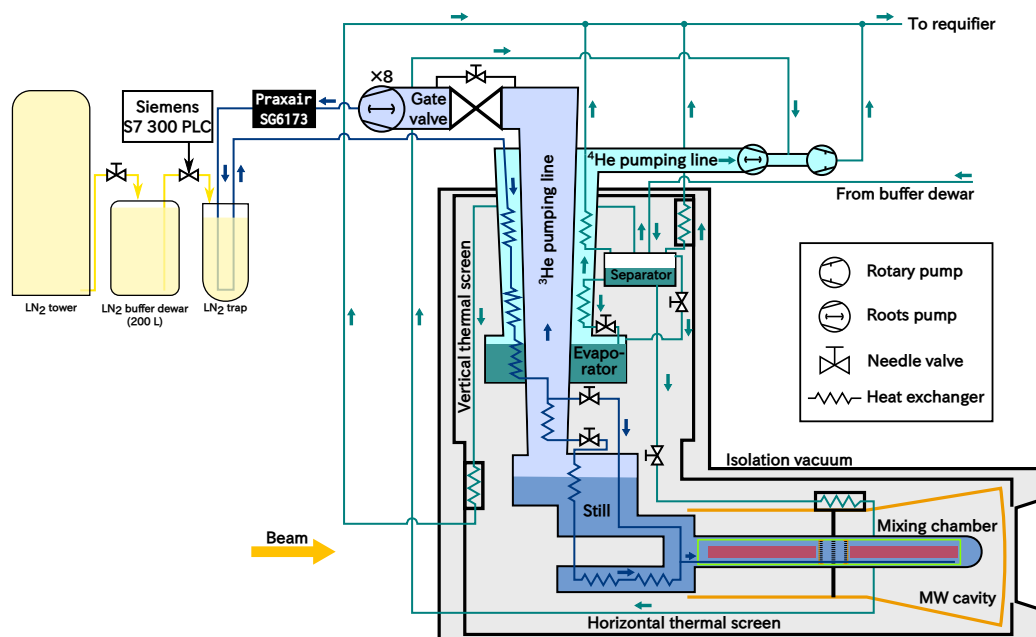
Figure 4.5: A schematic diagram of the cryogenics.

about 0.4 g/s. There is a water cooled heat exchanger between the roots and rotary pumps. The rotary pumps have an internal water cooling circuit additionally.

^{3}He system

About 9000 L of ^{3}He/^{4}He gas is stored at room temperature and is provided to the mixing chamber with exchanging heat between the ^{4}He system. The mixing chamber is made of glass fibre epoxy with 70 mm in diameter and 0.6 mm in wall thickness. ^{3}He/^{4}He is condensed in the mixing chamber and then liquefied. About 10 % to 15 % of the condensed ^{3}He/^{4}He in the mixing chamber is ^{3}He . The ^{3}He/^{4}He mixture is supplied through the CuNi tube and led to the still. ^{3}He is pumped out from the ^{3}He/^{4}He mixture in the still by a series of eight Pfeiffer roots blowers with canned motors. There are six external and internal heat exchangers to remove heat from the ^{3}He gas compression. The compressed gas at roots outlet has from 20 % to 30 % of ^{4}He typically. The ^{3}He gas after the roots is fed to four parallel Praxair SG6173 activated charcoal cartridges followed by a liquid nitrogen trap with activated charcoal to purify the gas. A temperature of the liquid nitrogen trap is monitored with three Pt100 temperature sensors inside to estimate the liquid level. The nitrogen trap is filled automatically from a 200 L buffer dewar by Siemens S7 300 PLC when the liquid level gets lower than a threshold.

Fig. 4.6 shows a temperature of the mixing chamber as a function of a rate of ^{3}He flow [96]. The curves show a dependence of a cooling power. The cryostat is operated in the larger filled region of the figure during DNP. In the DNP mode, a flow of the mixture at 0.65 mbar inlet pressure of the roots pumps is typically 0.2 g/s. A cooling power 350 mW can be obtained at about 300 mK in the mixing chamber and a ^{3}He flow of 100 mmol/ sec. In the frozen spin mode, the temperature of the still is about 1.0 K and pressure 0.42 mbar. A flow at 0.2 mbar of roots inlet pressure is about 0.07 g/ sec. A cooling power about 1 mW can be achieved in this condition.
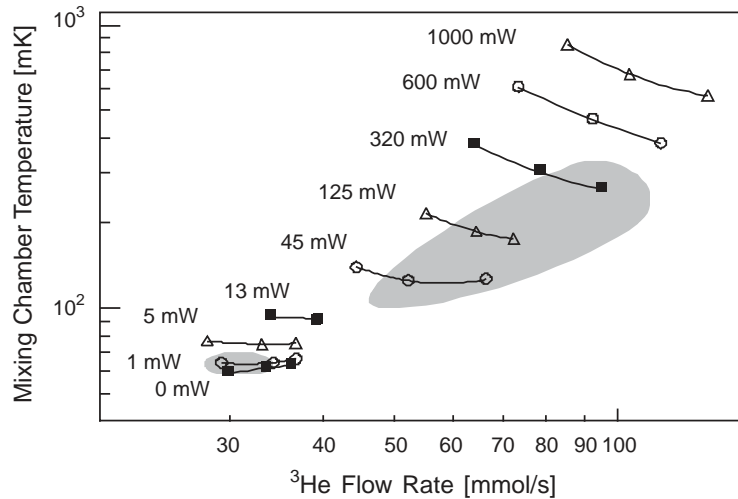
Figure 4.6: A temperature of the mixing chamber as a function of a flow rate of a ^{3}He . The curves show a dependence of a cooling power. The larger and smaller filled regions indicate the condition for the DNP and the frozen spin mode.

Thermal shield and isolation vacuum

The cryostat is placed in an isolation vacuum chamber which is pumped by Edwards Diffstak Mk2 160/700 diffusion pump and Alcatel 2033 rotary pump. Thermal screens surround the cryostat in a vertical and horizontal direction to stop a heat influx from a room temperature environment. Cold gas is provided from the separator to the screens by MKS flow controllers.

4.3.2 Microwave system

The microwave system provides microwave of two different frequencies at the same time to polarise the material in the opposite direction to each other. The system consists of microwave generators, power control attenuators, frequency counters and a power meter.

Fig. 4.7 shows a schematic diagram of the MW system. Microwave with a power of 20 W with a frequency of about 70 GHz is generated by a microwave generator EIO[2], and its power is controlled by the power control attenuator equipped with Magic-T's. It is divided into two lines: one is directed to the EIP-548-B Phase Matrix frequency counter and Millitech DET-12-RPFW0 power meter, and the other is led to the PT cryostat. On the way to the cryostat, its power is decreased by 6 dB to 8 dB. The microwave is fed on the target inside a microwave cavity made of 1 mm thickness of copper. The cavity consists of two parts: one is a cylindrical part with 1421 mm long and 410 mm in internal diameter, and the other is a conical section with 280 mm long. A MW stopper in the cavity isolates the cells from each other.

4.3.3 The solenoid and dipole magnet

The COMPASS superconducting magnet was installed in 2005 instead of the SMC magnet. The replacement increased an opening angle of the PT system from ± 69 mrad to ± 180 mrad. The COMPASS magnet system consists of a solenoid magnet and a dipole magnet (Fig. 4.8). The solenoid magnet with 2350 mm long, and 638 mm in internal diameter produces 2.5 T for DNP and maintaining longitudinal polarisation. There are several trim coils in the solenoid to achieve good homogeneity $\Delta B/B \approx 10^{-5}$ in a volume of 40 mm in diameter and 1300 mm in length along the beam axis. The dipole magnet provides 0.62 T in the transverse direction

---

[2]**E**xtended **I**nteraction **O**scillator
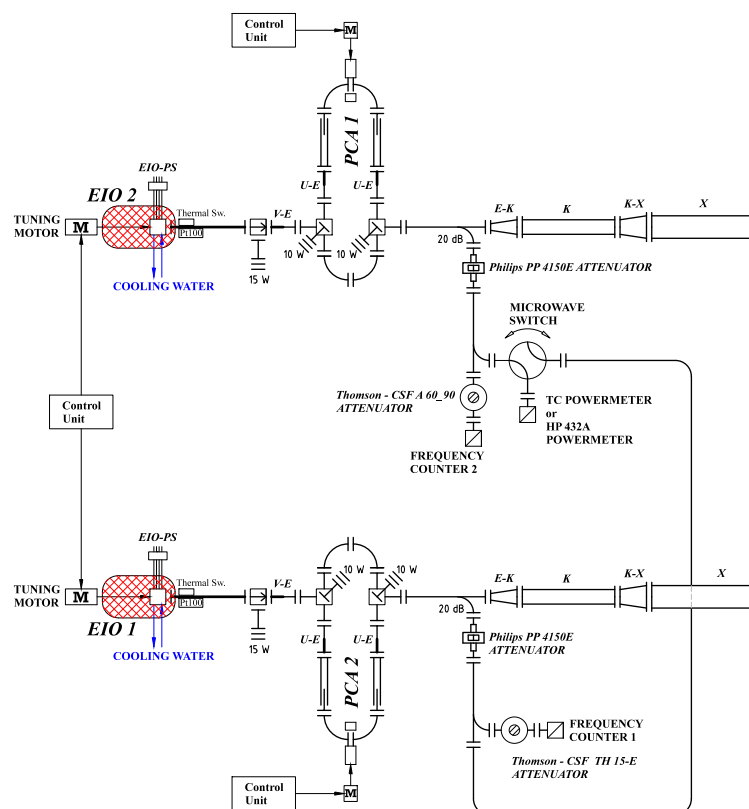
Figure 4.7: A schematic diagram of the microwave system. MW with different frequency is generated by EIO and fed to the cryostat. The power is controlled by the power control attenuator. The power and frequency are measured by EIP-548-B and DET-12-RPFW0.
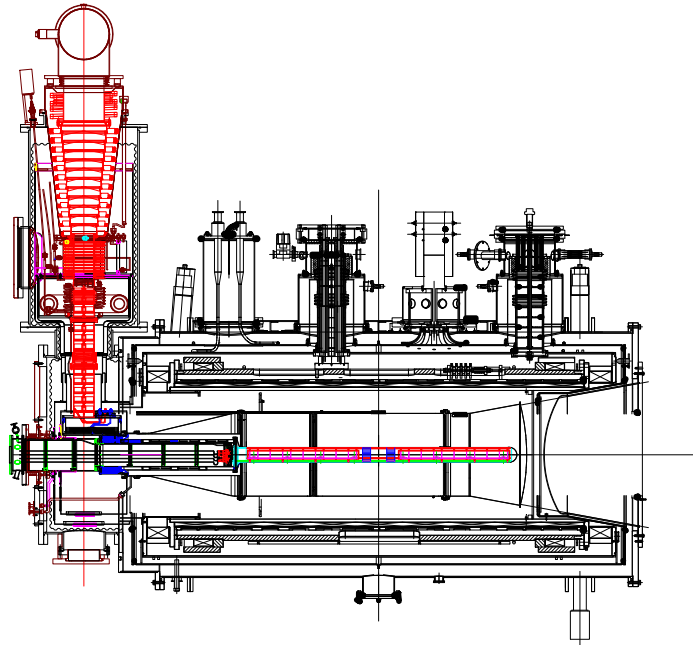
Figure 4.8: The design of COMPASS PT system.

for the magnetic field rotation described below and maintaining transverse polarisation. A homogeneity of the dipole field is much worse than that of the solenoid.

4.3.4 Polarisation measurement

The polarisation is measured with an NMR method. Fig. 4.9 illustrates the diagram of the NMR system. It consists of the 10 NMR coils, Liverpool Q-meter, Yale card, a National Instruments (NI) PXI crate and a synthesiser Programmed Test Sources (PTS250). The synthesiser sweeps frequency from 106.1 MHz to 106.7 MHz to deliver radio-frequency wave to the nuclei via the NMR coils. When NMR is caused, absorption of the radio-frequency wave is maximum, and the resonance signal is observed in the output voltage from the Q-meter as a function of frequency. The area of the NMR signal is proportional to the imaginary part of the magnetic susceptibility of the target and it is proportional to the polarisation. Consequently, the relation between the area of the NMR signal S_{NMR} and the polarisation P is described as $P = CS_{NMR}$.

The coefficient C is determined by measuring a TE signal, which is the NMR signal in TE state, and calculating a polarisation using Eq. (4.3). The measurement is called TE calibration. Background protons around the target material contribute to the TE signal but are not polarised by the DNP technique. This contribution must be subtracted from the TE signal. Measurement without the target material can determine its magnitude, which is called empty cell measurement.

4.4 Oparation

COMPASS PT was operated with the system introduced above. After installation of the PT magnets and the cryostat, position of the PT magnets were surveyed. The positions of the cells
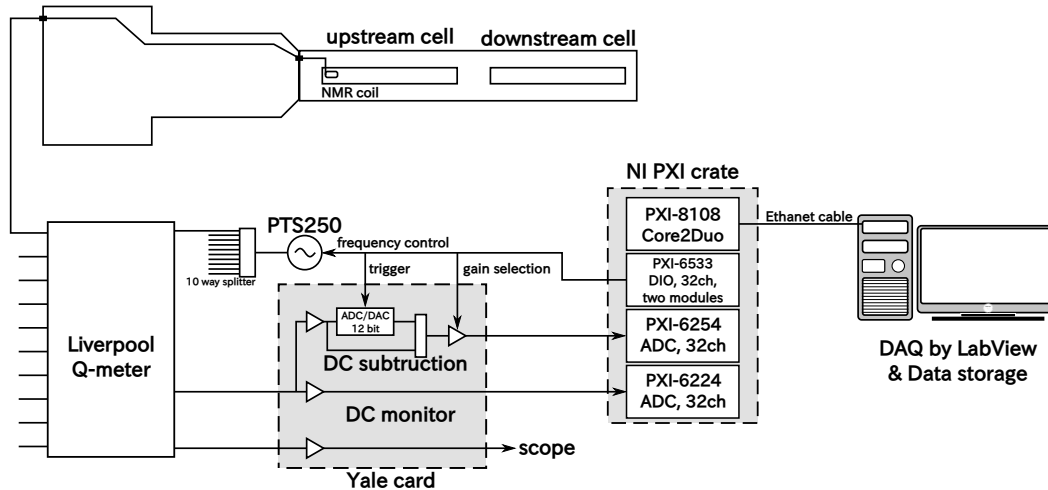
Figure 4.9: A diagram of the polarisation measurement system. Only one NMR coil is drawn.

Table 4.1: Elements in the cells. In the calculation, abundances of atom were used. For hydrogen, the natural abundances are 99.9885 % of protons and 0.0115 % of deuterons. For nitrogen, 99.632 % of ^{14}N and 0.368 % of ^{15}N.

	Proton	Deuteron	^{3}He
upstream (mol)	58.934 ± 0.317	0.007 ± 0.001	0.958 ± 0.207
downstream (mol)	49.974 ± 0.317	0.006 ± 0.001	1.149 ± 0.248
	^{4}He	^{14}N	^{15}N
upstream (mol)	9.757 ± 0.478	19.574 ± 0.106	0.072 ± 0.001
downstream (mol)	11.705 ± 0.573	16.599 ± 0.106	0.061 ± 0.001

are calculated using the survey data and the designed dimension of the cryostat. Operation of the PT system and a material loading are described in this section.

4.4.1 Loading of the target material

After assembling structure of the target cells, the target material was loaded into the target cells in a liquid nitrogen bath. The loading was carried out from the downstream part of the downstream cell to the upstream side. The weight of loaded ammonia was 333.5 ± 1.8 g and 282.8 ± 1.8 g for the upstream and the downstream cells, respectively. Table 4.1 summaries elements in the cells. A packing factor, which is a volume ratio of the loaded ammonia beads to the target cell 691.15 cm^3, was estimated with solid ammonia density of 0.853 g/cm^3 [92] and the weights of the loaded material. The packing factor of the upstream cell was 0.5657 and of the downstream cell was 0.4797. The whole structure was installed to the mixing chamber just after the material loading.

In the material loading for the pilot DY run 2014, an accident that a part of the loaded material to the downstream cell escaped to the nitrogen bath occurred. At that time, target cells made of polyamide were used except the eight caps for the loading holes as production of the PCTFE cells was not finished. Since thermal contraction coefficient of PCTFE is larger than that of the polyamide, the closed loading hole on the most upstream side of the downstream cell by the PCTFE cap was opened by itself. The escaped material was retrieved after
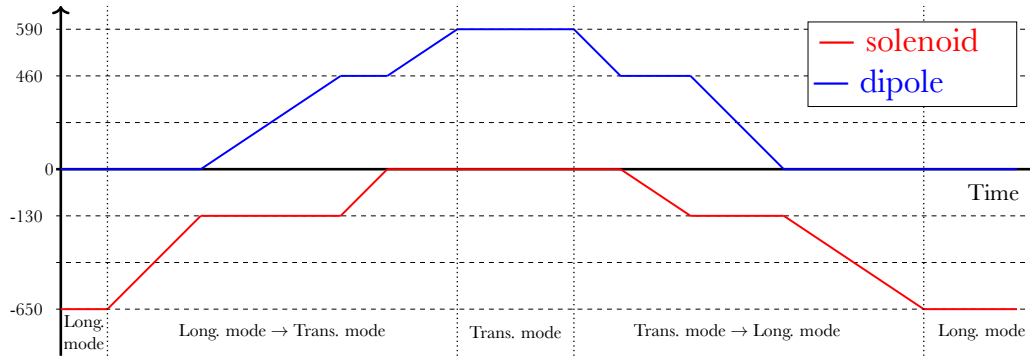
Figure 4.10: A diagram of the operation of magnets for the field rotation. A red and blue lines indicate current of the solenoid and the dipole magnets.

the loading, and some pieces of water ice and dust coming from the MW stoppers were mixed to it. They were combined with the material used for the downstream cell after the pilot run to have enough amount. A contamination of the water ice might affect the TE calibration since DNP does not polarise the hydrogen nuclei. Some pieces were removed in the unloading for 2014 run and the loading for 2015 run, but a dedicated operation was needed for the future DY measurement. The operation was performed in 2017 and described in Sec. 4.8.

4.4.2   Polarisation build-up and the transverse mode

The physics data taking was divided into periods that were about two weeks long. Each period was split into two sub-periods with opposite orientation of the polarisation. At the beginning of the first sub-period, DNP was performed in the 2.5 T solenoid magnetic field by feeding MW to the target cell. The speer carbon registers monitored the absorbed MW power for each cell. The polarisation was reached about 80 % after 24 h polarisation. After several operations of DNP, the slower build-up was observed in the downstream cell constantly. Some efforts were made to have a similar level of polarisation for the cells: MW irradiation to only the downstream cell at the beginning of DNP, giving more power of MW to the downstream cell, and so on.

Fig. 4.10 shows the operation of magnets to change the longitudinal mode to the transverse mode and vice versa. After the polarisation build-up, the target was cooled down to about 60 mK to operate the cryostat in the frozen spin mode. The field rotation from the longitudinal to the transverse mode is made as follows:

1. The current of the solenoid magnet was reduced from -650 A to -130 A.

2. The current of about 460 A was applied to the dipole.

3. The solenoid current was ramped down to zero

4. The dipole current was increased to 590 A.

The rotation took about 30 min, and about 1 % of polarisation loss was observed. The polarisation in the transverse mode was kept with 0.62 T dipole field only, and the physics data was taken. A direction of positive polarisation in the laboratory frame is from up to down. The field rotation from the transverse to the longitudinal mode was performed after the data taking to measure the final polarisation in the sub-period. The field rotation was a reverse operation of one from the longitudinal to the transverse direction.

Before the next sub-period, the polarisation was built up again in the opposite direction by changing the frequency of the microwave. From a second sub-period to a first sub-period
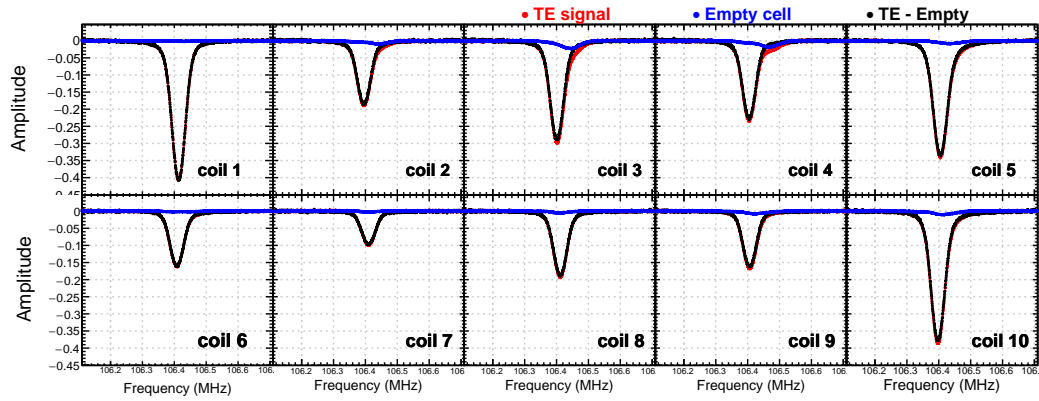
Figure 4.11: NMR signals as a function of frequency obtained from the TE measurement at 0.99 K (red) and the empty cell measurement (blue) for each coils. The black plots shows the subtraction of the TE signal and the empty cell signal.

of the next period, polarisation configuration was kept the same, and polarisation was topped up.

4.5   Result

Results of the TE calibration, the empty cell measurement, polarisation and relaxation measurements are discussed. Polarisation obtained by a coil during the physics data taking is determined by interpolation using the principle of the exponential relaxation. Polarisation will be determined as a function of z coordinate to include a position dependence of polarisation.

4.5.1   TE calibration and empty cell measurement

TE calibration is measurement of NMR signals at a stable temperature with the solenoid magnetic field to determine a relation between a polarisation and an area of a NMR signal. The TE calibrations were performed at 0.99 K, 1.28 K and 1.47 K. Thanks to enough statistic of the TE calibration, an statistical uncertainty of NMR signals was about 1 % to 2 % while it was from 2 % to 5 % in the previous run [97]. Protons in not only the target material but also the cells contribute to TE signals. The contribution from the cells must be subtracted from the TE signals. NMR signal measurement without the material, which is called an empty cell measurement, was performed at 0.97 K after the end of 2015 run The TE signals at 0.99 K, the empty cell signals and results of the subtraction of the empty signals from the TE signals are shown in Fig. 4.11. The contribution of the target cells was about 5 % thanks to the PCTFE while it was about 30 % in the previous COMPASS runs.

Since the approximation in Eq. (4.3) is valid at the typical temperature of the TE calibration 1 K and the magnetic field 2.5 T, an area of the NMR signal is proportional to the inverse of the temperature:

$$P \approx \frac{\mu B}{k_B T} = C S_{\text{target}} = C(S_{\text{TE}} - S_{\text{empty}}), \tag{4.5}$$

where C is a calibration constant, S_{TE}, S_{empty} and S_{target} are area of the TE signal, the cell and the target material, respectively. The calibration constants were determined by fitting to the obtained S_{target} with a linear function of $1/T$ as shown in Fig. 4.12. Table 4.2 summarise the results. Their statistical errors were from 0.2 % to 1.7 % and systematic errors were 3.15 %.
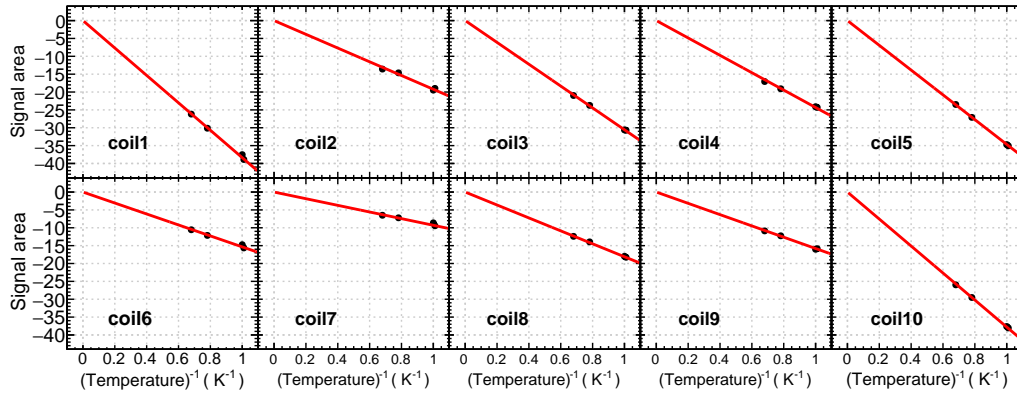
Figure 4.12: The result of TE calibration for each coils. The area of the NMR signal is plotted as a function of temperature inverse K^{-1}.

Table 4.2: Results of the TE calibration and the empty cell measurement.

Coil	C^{-1}	Statistical error
1	-38.13	0.52
2	-17.71	1.70
3	-27.36	0.47
4	-21.33	1.14
5	-33.40	0.22
6	-15.06	1.20
7	-9.00	1.77
8	-17.55	0.36
9	-14.70	0.58
10	-36.22	0.37
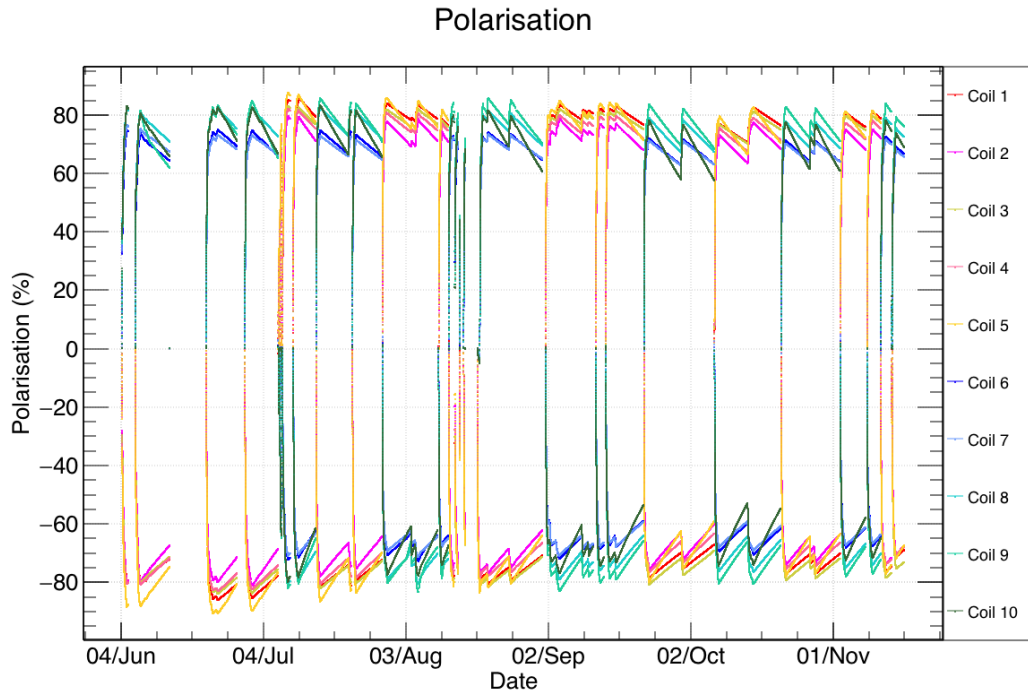
Figure 4.13: The polarisation measured by each coil as a function of time in 2015 run.

Table 4.3: The maximum polarisations and the average polarisations over the physics data taking. Polarisations are simply averaged over coils in the cell.

	Maximum polarisation (%)	Average polarisation over the physics data taking(%)
upstream	82.7, -86.0	74.2, -71.4
downstream	79.3, -77.8	69.2, -67.0

4.5.2 Polarisation values

Fig. 4.13 shows the polarisation measured by the NMR coils in 2015 run. The positive and the negative transverse polarisation indicates the direction of the dipole magnetic field from up to down and down to up, respectively. About 80 % polarisation was achieved at maximum as summarised in Table 4.3 along with the average polarisation over the physics data taking time. Since a deviation of the polarisation over the coils cannot be neglected and suggests position dependence of the coils, polarisation needs to be determined event by event for the physics analysis.

In the physics analysis, averaged polarisation over elapsed time and each cell in a sub-period is used. In the determination of the average, two kinds of interpolation are needed to determine polarisation event by event. One is interpolation along elapsed time since the polarisation was measured only before and after the sub-period. The other one is interpolation along z coordinate of the primary vertex introduced in Sec. 3.9. The first interpolation will be discussed in Sec. 4.5.3 and the latter in Sec. 4.6.

4.5.3 Relaxation time

Since polarisation was not measured during the physics data taking, the polarisation values in the physics data taking were interpolated with an exponential decrease formula $P(t) =$

Table 4.4: Average relaxation times of upstream or downstream cell. Each relaxation time was averaged over coils in the cell.

Cell	Beam	Positive polarisation (h)	Negative polarisation (h)
upstream	on	1400	1200
	off	3600	2900
downstream	on	1000	740
	off	4900	1700
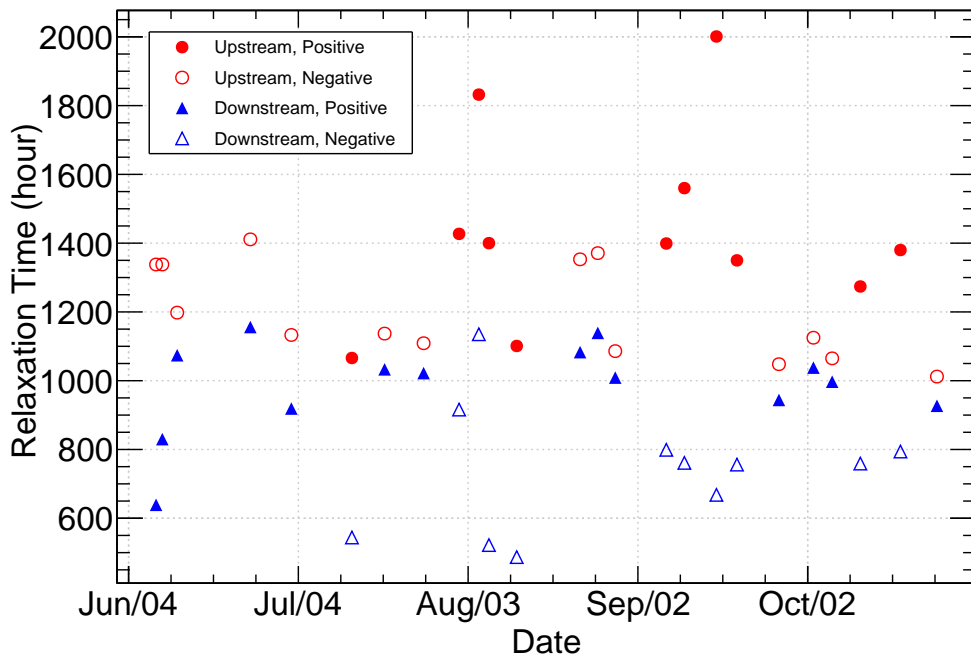
Figure 4.14: Relaxation time for each cell, polarity as a function of the measured date. Red and blue markers indicate the relaxation time of the upstream and the downstream cell. Filled and open markers shows those of the positive and negative polarisation.

$P_0 \exp\left(-t/\tau\right) + P_{TE}$ where τ characterises the rate of polarisation loss and is called a relaxation time.

The relaxation time depended on the target cell, a sign of polarisation and the beam condition as summarised in Table 4.4. Obviously, the relaxation times without the beam were longer than those with the beam. This difference may be understood as effect of heat introduced by the beam and many secondary particles. The relaxation times of the upstream cell with the beam were longer than those of the downstream cell while those of the upstream without the beam were shorter than those of the downstream cell.

Fig. 4.14 shows the relaxation time for each target cell and for each polarity as a function of the measured time. The relaxation time of the downstream was always shorter than that of the upstream cell. A dependency of the measurement time was not observed.
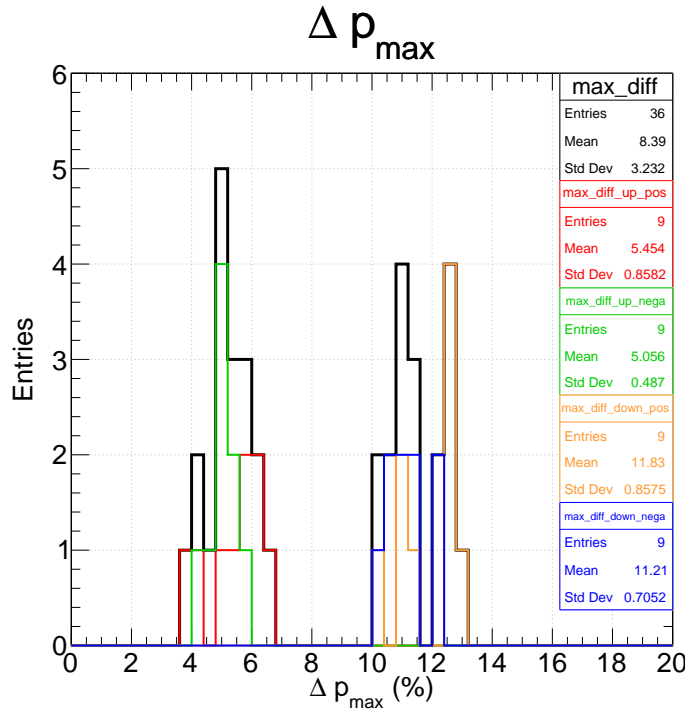
Figure 4.15: A distribution of a maximum difference of polarisation $\Delta p_{\max}$ in each cell period by period where $\Delta p_{\max} \equiv \max(|p_i - p_j|)$. A red(green) line indicates the distribution from the upstream cell in positive(negative) direction. An orange(blue) line shows the distribution from the downstream cell in positive(negative) direction. The ones from the downstream cell are larger than those from the upstream.

4.6 Determination of polarisation as a function of z coordinate

The measured polarisation deviated among the coils since polarisation was not uniform over a cell. Usually a simply averaged polarisation over coils in a cell had been used in COMPASS analysis. Since irradiation of the hadron beam on the PT was the first attempt in COMPASS, an estimation method of polarisation of a cell should be considered again. A maximum difference of polarisation in a cell period by period [3] $\Delta p_{\max} \equiv \max(|p_i - p_j|)$ is shown in Fig. 4.15. The subscript i, j denotes the coil ID. $\Delta p_{\max}$ distributed from 4 % to 13 % depending on the cell and the polarity while it was a few %in the previous COMPASS run. Therefore the deviation must be considered in the averaging and the simple average of polarisation over a cell no longer characterises polarisation in a cell. Several tests of interpolation of polarisation as a function of z were carried out; a liner interpolation using only the inner coils, the Lagrange interpolation over the cell, and a linear interpolation using adjacent coils. Measured polarisation by a coil includes errors about 1 % in statistical and 3 % in systematic. The errors cannot explain the large deviation of polarisation. Therefore, all coils should be taken into account. The Lagrange interpolation gives smooth and reasonable distribution along the z-axis, and the average is almost same as one from Zig-Zag method. However, our data was not enough to ensure the validation, for example, a boundary condition at edges of a cell. Finally, the last method namely Zig-Zag was used. The method assumes:

- the polarizations determined with the NMR measurement are reliable

---

[3]The period is defined in Sec. 5.1.

Table 4.5: Absolute polarisation averaged over a sub-period and target cells. The averaged polarisation over all periods was 72.6 %.

Period	W07	W08	W09	W10	W11	W12	W13	W14	W15
Polarisation (%)	75.2	73.8	74.6	73.1	71.8	69.5	72.0	71.6	73.0

- the difference of polarisations suggests that the existence of nonuniformity of polarisation

- polarisation as a function of z is a continuum.

A formula of the method is written as

$$
p(z) = \begin{cases}
p_1 & (\text{if } -315\,\text{cm} < z < z_1) \\
\dfrac{(z_{i+1} - z)p_i + (z - z_i)p_{i+1}}{z_{i+1} - z_i} & (\text{if } z_i < z < z_{i+1} \text{ where } i = 1, 2, \ldots, 9 \text{ except } 5) \\
p_5 & (\text{if } z_5 < z < (\text{the centre of cells})) \\
p_6 & (\text{if (the centre of cells)} < z < z_6) \\
p_{10} & (\text{if } z_{10} < z < -135\,\text{cm}) \\
0 & (\text{otherwise}),
\end{cases}
$$

(4.6)

where i is the number of coils, $z_i(p_i)$ is a z coordinate (polarisation) of the coil. z coordinate of edges of the upstream cell were -294.5 cm and -239.3 cm and those of the downstream cell were -219.5 cm and -164.3 cm. The upper limit -315 cm and lower limit -135 cm were taken to cover both target cell with enough margin. Fig. 4.16 shows an example of the Zig-Zag method.
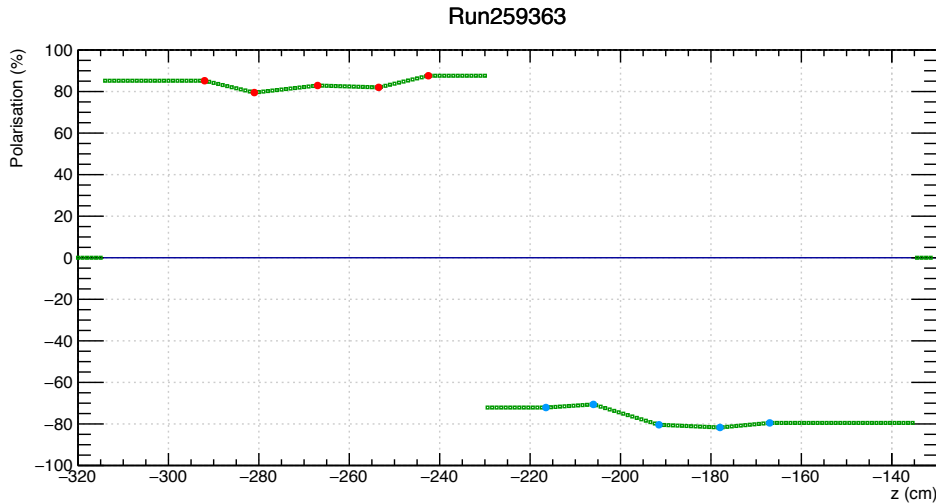
Figure 4.16: An example of the Zig-Zag method. Red(Blue) points indicate the polarisation obtained by a coil in the upstream(downstream) cell. The interpolated polarisation is drawn with a green line.

Polarisation was determined event by event using the Zig-Zag method for each sub-period for the asymmetry extraction. Table 4.5 summarise absolute polarisation averaged over a sub-period and the target cells.

Table 4.6: The Performance of transversely polarised proton target. Data except 1996 were obtained from COMPASS. The "OLD" material was produced in 1995, and the "NEW" material was in 2011.

Year	Beam (GeV/c)	Material	Target cells (cm)	Magnetic field (T)	Maximum polarisation (%)	Relaxation time (h)
1996 SMC	μ, 190	OLD	65, 65	0.5	89, -91	500
2007	μ, 160	OLD	30, 60, 30	0.6	93, -95	4000
2010	μ, 160	OLD	30, 60, 30	0.6	87, -87	9000
2015	hadron, 190	NEW	55, 55	0.6	82, -86	1000

4.7 Comparison with the previous results

Results of transverse polarised proton targets using the ammonia in COMPASS and SMC [98, 99] are summarised in Table 4.6. The lower polarisations and the shorter relaxation times in 2015 than those from the previous results can be understood by the following reasons.

The first reason is the difference of the beam particles and their intensity. The hadron beam with an intensity of about 6×10^7 particles/s was used in 2015 while the muon beam with an intensity of about 4×10^7 muons/s was used in the other years. As discussed above, the hadron beam affected the relaxation time significantly. Additionally, higher intensity of the beam gave more heat to the target. As a result of this, the maximum polarisation achieved was lower than the previous results.

The second reason is an age of the target material. The "NEW" material used in 2015 was produced in 2011 while the "OLD" material used in the previous runs was produced in 1995. The "OLD" material has less paramagnetic centre comparing with the "NEW" material since the paramagnetic centres can be recombined as time passes. This ageing effect makes the target be polarised slower and the relaxation slower. [4]

4.8 Cleaning of the target material

The target material for the downstream cell in 2015 run was cleaned since the contamination of the water ice was known. Fig. 4.17 illustrates the setup of the cleaning. The operation was performed in the glove box to avoid exposure of toxic ammonia gas. The box had a dry gas N_2 supply line to flush ammonia atmosphere and minimise contamination of water from ambient air humidity. There are an outlet line and a relief line for the gas N_2. A pressure gauge on the top of the box monitored the pressure inside the box. Two dewars with 6.6 cm height and 20 cm diameter were set inside the box and filled with liquid nitrogen. The material was divided into two and brought to one of the dewars, and operators removed foreign materials with tools.

Fig. 4.18c shows the all retrieved things. The liquid in the picture was the water ice, and black things were probably dust of carbon coming from the MW stoppers and the coated part of the kevlar tube. Several big ice pieces with a size of about 1 cm were taken. Such big pieces can affect to the TE calibration if they are very close to the NMR coil. The total amount of retrieved things was about 3.6 g, which corresponds to about 1.3 % of the loaded material to the downstream cell.

---

[4] the followings will be mentioned: the suitable spin density 10^{19} spins/g, attenuation of the unpaired electron number
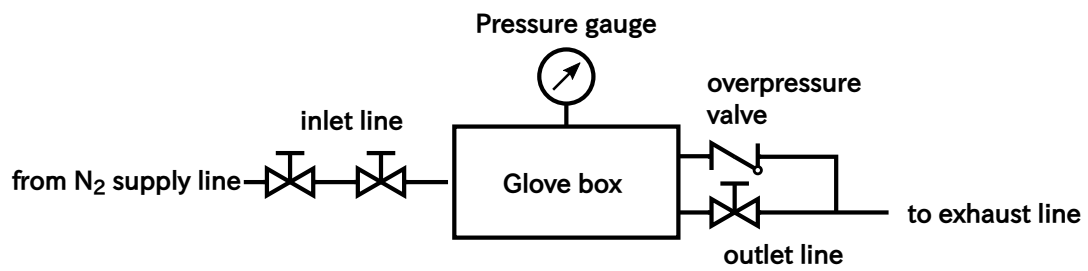
Figure 4.17: A schematic diagram of a setup of the cleaning.

(a) The setup.

(b) One of the biggest water ice retrieved.
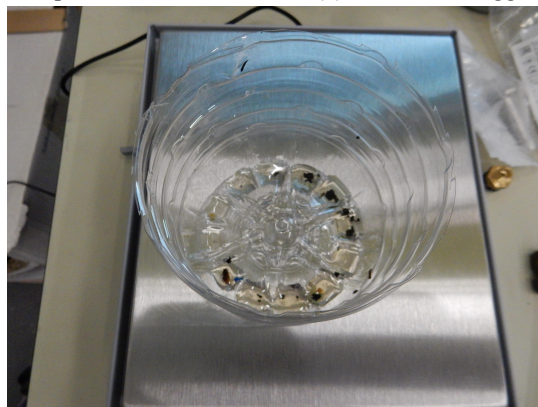
(c) All retrieved things.

Figure 4.18: Pictures of the cleaning of the target materials.

Chapter 5

Analysis

Asymmetry extractions and studies for the extractions are presented in this chapter. At first, stability in data taking is checked by analysing chronological change of parameter. Event selection is performed to get pairs of a muon and an anti-muon (dimuons) from the DY process. A cut of dimuon mass range is studied to remove dimuons coming from non-DY processes with MC simulation. Some dedicated MC study of the DY process are carried out to study effects by the reconstruction and an acceptance of the COMPASS spectrometer. Finally, the asymmetries discussed in Chapter 2 are extracted from the selected dimuon events. Many systematic studies on the asymmetry extraction are also performed.

Definition of the lab frame

In this thesis, a lab frame is defined as below:

z-axis nominal beam direction

y-axis vertical direction from down to up

x-axis direction of a vector product of $\vec{y} \times \vec{z}$.

Unlike the TR frame Sec. 2.3, the z-axis in the lab frame is not changed in spite of deviation of the beam direction. The origin of the coordinate is kept the same as that used in the previous SIDIS measurements where it was defined as the centre of the PT, for example [100], however the PT system is moved to the upstream by about 2 m for installation of the hadron absorber. The centre of the PT system for the DY measurement is at (0, 0, -230) in cm. A θ angle is the zenith angle and a ϕ angle is the azimuthal angle.

5.1 Data taking period

A six-month data taking which was divided into nine periods was carried out in 2015 as Table 5.1 summarises. Each period took two weeks except for the last period and was composed of two sub-periods. In a sub-period, data taking was performed in a "run"". A typical run collects data of 200 spills.

5.2 Stability checks

In the long measurement, data taking was sometimes not stable for many kinds of reasons: unstable beam, troubles with or repair of detectors and so on. Since such data may introduce bias toward analysis, they are called "bad" and must not be analysed. This stability check finds such unstable condition statistically by analysing the reconstructed data. This kind of stability check has been performed in SIDIS analysis at COMPASS [101].

Table 5.1: List of the physics data taking period in the 2015 run. The notations "+" and "-" in the polarisation column means a positive and a negative polarisation, respectively. Direction of polarisation is defined in Sec. 4.4.2.

Period	Sub-period	Polarisation (up-, down-stream)	First run	Last run	Begin time (day/month)	End time (day/month)
W07 (P1)	1	+−	259363	259677	09/07	15/07
	2	−+	259744	260016	16/07	22/07
W08 (P2)	1	−+	260074	260264	23/07	29/07
	2	+−	260317	260565	30/07	05/08
W09 (P3)	1	+−	260627	260852	06/08	12/08
	2	−+	260895	261496	13/08	26/08
W10 (P4)	1	−+	261515	261761	26/08	01/09
	2	+−	261970	262221	04/09	09/09
W11 (P5)	1	+−	262370	262772	11/09	22/09
	2	−+	262831	263090	23/09	30/09
W12 (P6)	1	−+	263143	263347	30/09	07/10
	2	+−	263386	263603	08/10	14/10
W13 (P7)	1	+−	263655	263853	15/10	21/10
	2	−+	263926	264134	22/10	28/10
W14 (P8)	1	−+	264170	264330	28/10	02/11
	2	+−	264429	264562	04/11	08/11
W15 (P9)	1	+−	264619	264672	09/11	11/11
	2	−+	264736	264857	12/11	16/11

Spill by spill check

Reconstructed events having pairs of oppositely charged penetrating particles which travel more than 30 radiation lengths between the first and the last measured points are analysed. Additionally, the item 3 criterion which will be introduced in Sec. 5.3 is applied to ensure that the muon travels through the spectrometer. Checked parameters event by event are listed in Table 5.2. Here, definitions of the track, the muon, the vertex, and the primary vertex are given in Sec. 3.9.

Assuming that most of the data were taken in stable condition, these parameters listed in Table 5.2 should be constant in time. Therefore a comparison of a parameter obtained from a spill to an averaged value over neighbouring spills can judge whether the condition of the measurement during the spill was stable or not.

To define "bad" spills, parameters of a spill are compared to those of a group of spills in the data taking period. The group of spills are composed of continuing spills around the spill in time. The size of the group is determined for each parameter and each period. A mean and a standard deviation of the parameter, $\langle x \rangle$ and σ, are calculated for each group. If a parameter of a spill is out of the range of $(\langle x \rangle \pm X \times \sigma)$, the spill was tagged as bad. Where X characterise tolerance. Some examples of the tolerance in units of the sigma and the number of neighbouring spills are shown in Table 5.4. Fig. 5.1 shows examples of the check for the three periods W07, W13 and W15. Blue and red points indicate good and bad spills, respectively. The plots on the top, the middle, and the bottom correspond to item 12, item 5 and item 4 in Table 5.2, respectively. Most points far from the majority are detected successfully. Furthermore, the check can find groups of bad spills, for example, one in the top left plot. Some red points can be found in a majority region since the check is performed for all parameters at same time. Even if most parameters are found to be good and only one parameter is bad, the spill is tagged as bad.

Table 5.2: List of macro-variables checked for the spill by spill check.

1. number of beam particles per event

2. number of primary vertices per event

3. number of outgoing particles per event

4. number of outgoing tracks per event

5. number of outgoing particles from primary vertex per event

6. number of μ^+ tracks per event

7. number of μ^- tracks per event

8. number of μ^+ tracks from primary vertex per event

9. number of μ^- tracks from primary vertex per event

10. number of hits by beam particles per beam particle

11. number of beam particles per primary vertex

12. number of outgoing particles from primary vertex per primary vertex

13. number of hits by outgoing particles per outgoing particle

14. sum of χ^2 of outgoing particles per outgoing particle

15. sum of χ^2 of all vertices divided by all vertices

16. trigger rate of LAST-LAST, MT-LAST and OT-LAST.

Table 5.3: List of kinematic variables and angles checked for the run by run check.

1. x_N, x_π, x_F, q_T, and $M_{\mu\mu}$

2. momentum of muons, dimuon, and beam

3. position of interaction vertex

4. azimuth angles of muons, dimuon and beam in a laboratory frame

5. θ_{CS}, ϕ_{CS}, and ϕ_S

Table 5.4: Examples of the tolerance in units of the sigma and the number of neighbours for the bad spill rejection. The parameters are used for the items item 1, item 2, and item 11 in Table 5.2. The values in "Sigma" column is shown in units of a standard deviation.

Period	Tolerance size (σ)	Number of neighbours
W07	3	3000
W08	3	3000
W09	4	1500
W11	3	2000
W12	3	1000
W13	3	1000
W14	2	500
W15	5	1000
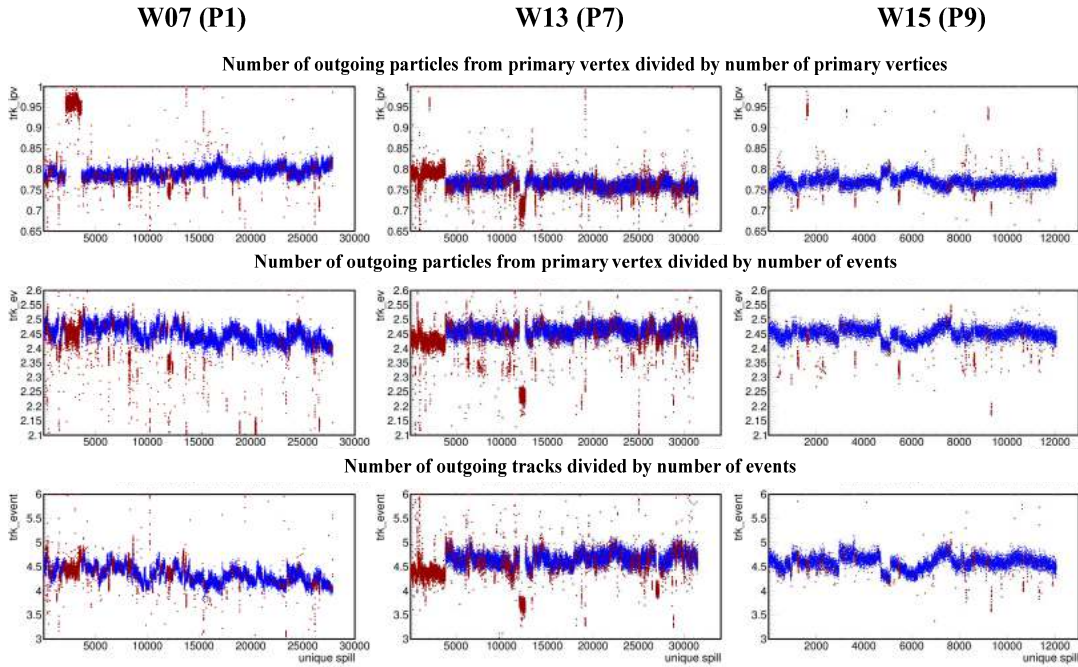
Figure 5.1: Examples of the bad spill check. Three periods W07, W13 and W15 are shown. The top, the middle, and the bottom plots correspond to the item 12, item 5 and item 4 in Table 5.2, respectively. The horizontal axis corresponds to a serial number of a spill in a period. Blue and red points represent the good and bad spills, respectively.

Table 5.5: Impact of the stability check. The second column shows a fraction of a rejection by the spill by spill check. The third column shows a ratio of a rejection by the run by run check in addition to the second column. The values are fraction of bad spill/runs to all spills/runs.

Period	Bad spill (%)	Bad spill and run (%)
W07	11.79	17.94
W08	18.00	21.19
W09	14.76	17.11
W10	15.88	17.80
W11	22.49	26.14
W12	12.71	13.79
W13	22.32	22.73
W14	8.91	10.70
W15	3.94	3.94

Run by run check

Stability of not only the parameters but also some variables related to dimuons must be checked since they can affect results of physics analysis directly. A mean value and the shape of a distribution of the variables summarised in Table 5.3 are monitored by analysing data with the data selection criteria which will be introduced in Sec. 5.3. Since the number of dimuon events is few, typically ten, variables are averaged over a run and checked run by run. If a mean of the variable is away from five standard deviations of the overall mean in its period, the run is tagged as bad. The shape of distribution is compared with one from the other runs with Unbinned Kolmogorov-Smirnov (KS) test [102]. If a distribution is not compatible with most of the runs, the run is marked as bad. Run by run checks are carried out after applying the results of the spill by spill check. In addition to the checks, runs having less than ten spills or bad spills of 70 % are rejected since short runs usually mean that the data taking was interrupted due to some problem identified. Fig. 5.2 shows some results of the run by run check for the virtual photon momentum. The lines and points correspond a shape and mean of a run. Green and blue indicate configuration of polarised target. The red lines and points are runs tagged as bad. Only the bad run rejection is applied to plots in Figs. 5.2a and 5.2c. Figs. 5.2b and 5.2d show impact of the bad run rejection with applying the bad spill rejection in advance. Fig. 5.2a and Fig. 5.2c are results of the checks while Fig. 5.2b and Fig. 5.2d are results of the checks with applying the bad spill rejection in advance. The spill by spill check had rejected most of "bad" runs. A list of bad runs are made to reject them in the selection in Sec. 5.3.

Table 5.5 summarises the impact of the checks. Results were stored in a list for the data selection described in Sec. 5.3.

5.3 Data selection

After the stability checks, the following event selection criteria were applied to obtain appropriate dimuon events. Order of applying cut is the same as the following list.
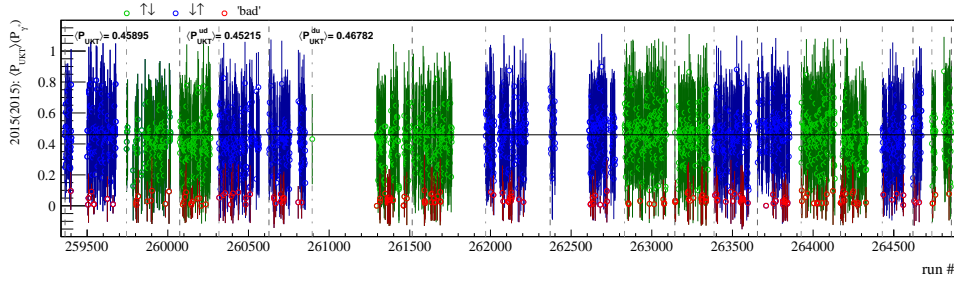
(a) A result of unbinned KS test for a virtual photon momentum $P(\gamma^*)$ as a function of the run number.
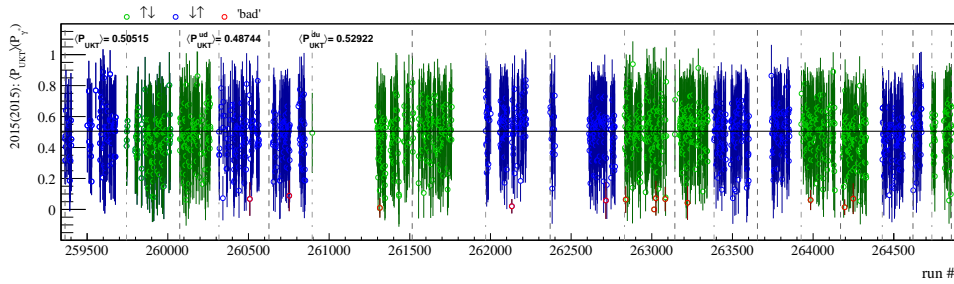
(b) The same as Fig. 5.2a for the data with the bad spill rejection in advance.
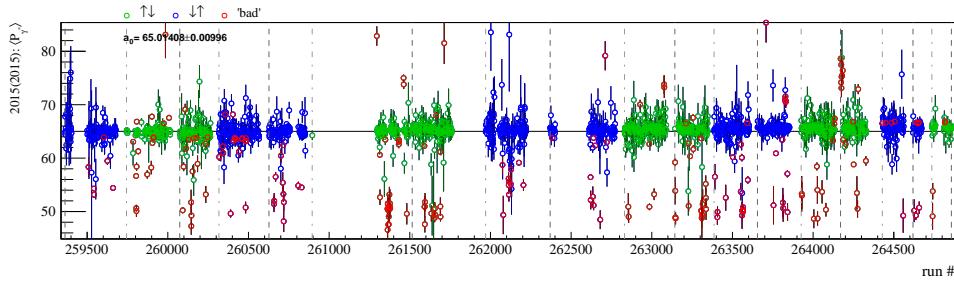
(c) A comparison of mean value of the $P(\gamma^*)$.
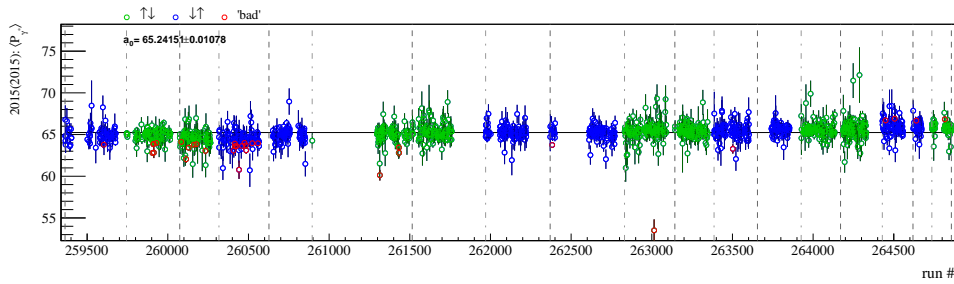
(d) The same as Fig. 5.2c for the data with the bad spill rejection in advance.

Figure 5.2: Examples of the bad run check for a virtual photon momentum $P(\gamma^*)$. Green and blue points represent configuration of polarisation. When the target in the upstream cell is polarised to positive while one in the downstream to negative, a green mark is plotted. The Blue marks are vice versa. Red circles indicate bad runs.

1. **Oppositely charged dimuon ($\mu^+\mu^-$ cut)**
   The first cut requires a pair of positive and negative muons associating with a primary vertex. If two or more primary vertices are associated with the pair, the best primary vertex, which has the most associated tracks, is taken. If some candidates exist, one with the smallest χ^2 is taken.

2. **Dimuon trigger (Trigger cuts)**
   A firing of at least LAST-LAST or OT-LAST is required. [1]

3. **The first and the last measured point (Zfirst and Zlast cuts)**
   These are requirements to the first and the last measured point of muon tracks. The first measured point in an upstream of the SM1 magnet ($z = 300$ cm) and the last measured point in a downstream of the Muon Filter1 ($z = 1500$ cm) are required.

4. **Definition of muon's track time (T-def cut)**
   It requires that a track time of each muon ($t_\pm$) with respect to the trigger time is defined.

5. **Difference of muons' track time (T-diff cut)**
   A difference of the muons' track time is less than 5 ns, i.e. $|t_+ - t_-| < 5$ ns.

6. **$\chi^2/\mathbf{NDF}$ of muon tracks ($\chi^2/\mathbf{NDF}$ cut)**
   The χ^2 for the track reconstruction, which has been introduced in Sec. 3.9, for both muons divided by a Number of Degrees of Freedom (NDF) is required to be less than ten.

7. **Trigger validation cut**
   This cut ensures that the muon tracks are in an active area of the fired dimuon trigger geometrically. Muon tracks are extrapolated to the trigger hodoscopes. If both LAST-LAST and OT-LAST are fired, at least one validation is required.

8. **Bad spills and runs rejection (Bad spill/run cuts)**
   The results of the stability checks discussed in Sec. 5.2 are applied to get good runs and spills.

9. **The Bjorken variable x_π, x_N and the Feynman's x_F cuts**
   $0 < x_{\pi(N)} < 1$ and $-1 < x_F < 1$ are required. These cuts reject dimuon events reconstructed incorrectly.

10. **q_T cut**
    Transverse momentum of the virtual photon q_T is required to be larger than $0.4\,\mathrm{GeV}/c$ and less than $5.0\,\mathrm{GeV}/c$. The lower limit ensures a reasonable angular resolution of the azimuthal angles. The upper limit rejects a tail of high q_T events although this impact is negligible.

11. **Target cut in z-axis**
    Interaction vertices are required to be inside the target cells, i.e., -294.5 cm to -239.3 cm or -219.5 cm to -164.3 cm in z coordinate as Fig. 5.3 shows.

12. **Target cut in r-axis**
    r-axis is defined in a cylindrical system with x and y coordinates in the laboratory system by the following formula: $r = \sqrt{x^2 + y^2}$. This cut requires an R of the primary vertices inside the target cells. Although the radius of the cell is 2 cm, less than 1.9 cm is required to cut the wall of the cells to ensure enough redundancy.
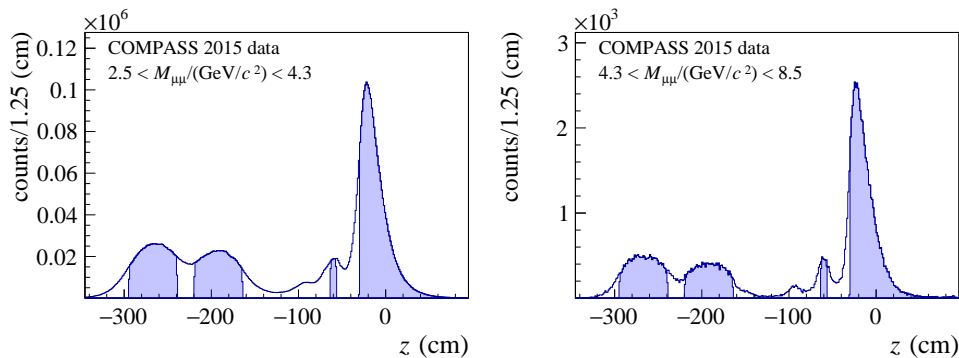
Figure 5.3: The primary vertex distribution in the z coordinate. The left and right plots are in the dimuon mass range from $2.5\,\text{GeV}/c^2$ to $4.3\,\text{GeV}/c^2$ and from $4.3\,\text{GeV}/c^2$ to $8.5\,\text{GeV}/c^2$, respectively. The four filled regions indicate the upstream and the downstream cell of the PT, an unpolarised aluminium target and the tungsten beam plug, respectively. In this analysis, events with the vertex in the PT cells are analysed.

The impact of each cut is summarised in Table 5.6.

5.4   Background estimation

According to the previous DY experiments, for example, NA50 collaboration [103], a cut of dimuon invariant mass can select DY events from other processes giving μ^+ and μ^- in the final state Fig. 5.4. An optimisation of the cuts was performed with Monte-Carlo simulation.

Fig. 5.5 shows a flow of this study. At first, MC events of DY, J/ψ, ψ' and Open Charm (OC) processes are generated and reconstructed by CORAL. The reconstructed data are analysed with the same analysis code for the real data. In parallel, a combinatorial background (CB) is estimated from the real data with the like-sign method. The MC events and CB are combined to reproduce the dimuon mass distribution obtained from the real data.

5.4.1   MC simulation of DY, J/ψ or ψ production and Open charm process

TGeant [104, 105] is a Geant4 [106] based Monte-Carlo simulation toolkit for COMPASS II experiment.

TGeant is implemented with several modes for each physics program: SIDIS, GPD, hadron spectroscopy, Primakoff and DY. In the DY mode, beam parameters were determined from a measurement in a dedicated run in 2014 with low-intensity pion beam and the operational BMS. TGeant equips Pythia6 [107] or Pythia8 [108, 109] for event generation. For a background estimation , Pythia8 is employed. Parton distribution functions are fed to Pythia via LHAPDF [110, 111]. The Gaussian type of the k_T distribution is assumed in all physics processes. The beam particle interacts with only proton or neutron. [2] In the current description, trigger and detector inefficiencies were not simulated.

MC events are generated as follows:

1. A beam particle, called a primary beam particle, is shot at $z = -700\,\text{cm}$ and $t = 0$. Parameters of the beam are determined by the parametrisation introduced above.

---

[1] A firing of MT-LAST is not required since most events firing MT-LAST include a μ^- coming from a decay of beam particle.

[2] A mixing switch to specify an interacting particle with the beam particle was implemented for future study. The switch selects according to a number ratio of proton and neutron in the material with weighting of a cross section.

Table 5.6: The number of events with the selection criteria in two dimuon mass ranges. The value in a cell is obtained by applying the cuts on its row and all the above.

Cut	$2 < M_{\mu\mu}$ GeV/c^2	$4.3 < M_{\mu\mu} < 8.5$ GeV/c^2
1. $\mu^+\mu^-$ cut	41008609	1159349
2. Trigger cuts	32046393	868291
3. Zfirst and Zlast cuts	30467114	784379
4. T-def cut	30301533	776643
5. T-diff cut	19059490	373081
6. χ^2/NDF cut	18937973	370054
7. Trigger validation cut	14238292	169526
8. Bad spill/run cuts	11629288	138255
8. x_π, x_N and x_F cuts	11629087	138159
9. q_T cut	10107057	124848
10. Target cut (Z)	2917566	38200
11. Target cut (R)	2554933	34904
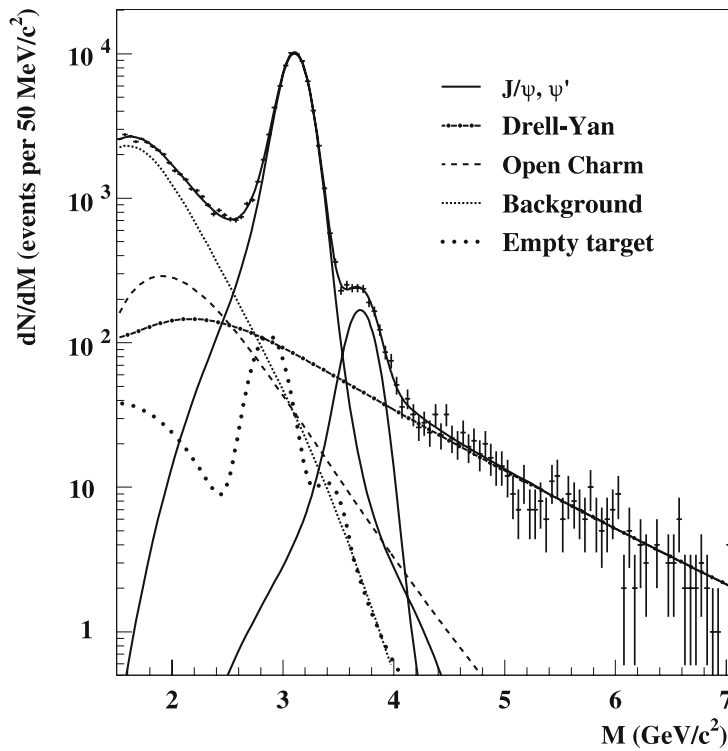
Figure 5.4: Dimuon mass distribution from a proton beam on a lead target at NA50 experiment in CERN [103].
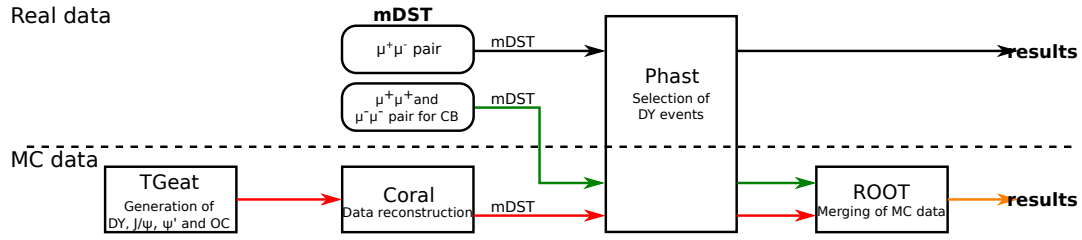
Figure 5.5: A flow of the background estimation. TGeant generates DY J/ψ, ψ' and OC events independently. CORAL reconstructs these raw data with the same condition as the mass production of the real data. The combinatorial background was estimated from the real data using the like-sign method. MC data and combinatorial background were combined to reconstruct the dimuon mass distribution after analysing mDSTs. The same analysis program for the real data was used for the analysis. The merging of MC and CD was performed at the level of ROOT.

2. Some beam particles are also shot to simulate the effect of a pileup if a user requires. The pileup beam particles distribute from $-T$ to T uniformly in time. The number of the pileup beam particles is determined by a Poissonian random number generator with the T and a beam intensity Φ as follows:

$$n = \text{RandPoisson}(2T \cdot \Phi) - 1, \tag{5.1}$$

where RandPoisson() is a random number generator that produces integers according to a Poisson distribution. The subtraction of one is needed for the primary beam particles.

3. Trajectories of the beam particles are simulated. Additionally, a point where the first inelastic interaction of the primary beam occurred is defined as an interaction point of the simulating physics process, for example, DY.

4. Pythia generates the physics event at the interaction point using the parameters of the primary beam.

5. Geant4 simulates passage of particles generated by Pythia and pileup beams through the COMPASS spectrometer. All information about the event is saved in an output file. Since the format is same as the real data, CORAL can reconstruct events in the output file in the same way as for the real data.

DY process

In the DY process simulation, a single photon production $f + f \rightarrow \gamma^*$ is allowed, where f represents a quark, and the photon decays into only a dimuon. A user can specify a range of a dimuon mass. A width of the primordial k_T distribution $0.9\,\text{GeV}/c$ is used for both pions and nucleons instead of the default value $1.0\,\text{GeV}$ to have more similar distribution to the real data. A lower cut off of $0.1\,\text{GeV}/c$ for q_T is applied to avoid singularities in $q_T \rightarrow 0$. An initial and final QCD/QED radiations are prohibited.

Since a cross section of the DY process decreases as the dimuon mass increases, an enormous number of events are needed to have enough statistics in order to compare to the real data over a long mass range. To have it with reasonable processing time, three types of DY simulations with different mass range are performed: a high mass DY (HMDY) with $3.5\,\text{GeV}/c^2$ to $9.0\,\text{GeV}/c^2$, a low mass DY (LMDY) with $1.5\,\text{GeV}/c^2$ to $3.5\,\text{GeV}/c^2$ and an all mass DY (AMDY) $1.5\,\text{GeV}/c^2$ to $9.0\,\text{GeV}/c^2$. Since AMDY is used as a reference to determine a shape of dimuon mass spectrum, much fewer events are generated for AMDY than those of HMDY

and LMDY. Event ratio of HMDY to LMDY were determined to reproduce the dimuon mass spectrum of the AMDY data. The merged DY data is simply called "DY-MC" or "DY".

J/ψ and ψ' production process

In J/ψ event generation, all charmonium processes equipped with Pythia8 are used:

- $g + g \rightarrow c\bar{c}[^3S_1^{(1)}] + g$
- $g + g \rightarrow c\bar{c}[^3S_1^{(8)}] + g$
- $q + g \rightarrow c\bar{c}[^3S_1^{(8)}] + q$
- $q + \bar{q} \rightarrow c\bar{c}[^3S_1^{(8)}] + g$
- $g + g \rightarrow c\bar{c}[^1S_0^{(8)}] + g$
- $q + g \rightarrow c\bar{c}[^1S_0^{(8)}] + q$
- $q + \bar{q} \rightarrow c\bar{c}[^1S_0^{(8)}] + q$
- $g + g \rightarrow c\bar{c}[^3P_J^{(8)}] + g$
- $q + g \rightarrow c\bar{c}[^3P_J^{(8)}] + q$
- $q + \bar{q} \rightarrow c\bar{c}[^3P_J^{(8)}] + g$
- $g + g \rightarrow c\bar{c}[^3P_J^{(1)}] + g$
- $q + g \rightarrow c\bar{c}[^3P_J^{(1)}] + q$

- $q + \bar{q} \rightarrow c\bar{c}[^3P_J^{(1)}] + g$
- $g + g \rightarrow c\bar{c}[^3S_1^{(8)}] + g$
- $q + g \rightarrow c\bar{c}[^3S_1^{(8)}] + q$
- $q + \bar{q} \rightarrow c\bar{c}[^3S_1^{(8)}] + g$
- $g + g \rightarrow c\bar{c}[^3D_J^{(1)}] + g$
- $g + g \rightarrow c\bar{c}[^3P_J^{(8)}] + g$
- $q + g \rightarrow c\bar{c}[^3P_J^{(8)}] + q$
- $q + \bar{q} \rightarrow c\bar{c}[^3P_J^{(8)}] + g$
- $g + g \rightarrow c\bar{c}[^3S_1^{(1)}] + c\bar{c}[^3S_1^{(1)}]$
- $g + g \rightarrow c\bar{c}[^3S_1^{(1)}] + c\bar{c}[^3S_1^{(1)}]$
- $q + \bar{q} \rightarrow c\bar{c}[^3S_1^{(1)}] + c\bar{c}[^3S_1^{(1)}]$.

Here, a spectroscopic notation $q\bar{q}[^{2S+1}L_J^{(N)}]$ is used to describe a spin of the particle, where (1) and (8) in the notation are reminders of the colour singlet and octet nature of these states. These particles are assumed to decay exclusively into J/ψ and g. The J/ψ is allowed to decay into only a dimuon. Other configuration is the same as the one for the DY process.

A pair of $c\bar{c}$ is generated in ψ' process and decays into dimuon:

- $g + g \rightarrow c\bar{c}[^3S_1^{(1)}] + g$
- $g + g \rightarrow c\bar{c}[^3S_1^{(8)}] + g$
- $q + g \rightarrow c\bar{c}[^3S_1^{(8)}] + q$
- $q + \bar{q} \rightarrow c\bar{c}[^3S_1^{(8)}] + q$
- $g + g \rightarrow c\bar{c}[^1S_0^{(8)}] + g$

- $q + g \rightarrow c\bar{c}[^1S_0^{(8)}] + q$
- $q + \bar{q} \rightarrow c\bar{c}[^1S_0^{(8)}] + q$
- $g + g \rightarrow c\bar{c}[^3P_J^{(8)}] + g$
- $q + g \rightarrow c\bar{c}[^3P_J^{(8)}] + q$
- $q + \bar{q} \rightarrow c\bar{c}[^3P_J^{(8)}] + q$

A setting for ψ' is the same as the J/ψ process.

Open charm process

OC process is a breakup of a $c\bar{c}$ pair into two mesons, one contains a charm quark and a light anti-quark, and the other contains a anti-charm quark and a light quark. In this simulation, $g + g \rightarrow c + \bar{c}$ and $q + \bar{q} \rightarrow c + \bar{c}$ are simulated. A muon or an antimuon must exist in the decay of produced mesons.

5.4.2 Combinatorial background

Many muons are produced in the same event by decay of mesons which are created in hadronic cascade interactions (e.g., $\pi^{\pm} \to \mu^{\pm} + \nu_{\mu}(\bar{\nu}_{\mu})$) mainly in the hadron absorber. Such uncorrelated pairs of muons form combinatorial background in the DY measurement. Since there are no charge correlation in the background, one can estimate a contribution of the combinatorial background using pairs of same charge muons, like-sign pair. It estimates a contribution of the combinatorial background (CB) to the measured dimuon statistically. The like-sign method gives the number of the pairs of uncorrelated oppositely charged muons by counting the number of pairs of uncorrelated identically charged muons.

In condition with the high-intensity hadron beam, Poisson distribution describes the number of combinations of uncorrelated identically charged mesons. Number of combinations of positive mesons decaying into a muon is given as:

$$_{n_+}C_2 = \frac{n_+!}{2(n_+ - 2)!} = \frac{n_+(n_+ - 1)}{2}, \tag{5.2}$$

where n_+ is number of positive mesons. Eq. (5.2) holds both for positive and negative mesons. The number of like-sign pairs of positive muons N_{++} in N times of interaction is described as follows:

$$\begin{aligned}
N_{++} &= N A_{++} \int P(n_+) \omega^2 {}_{n_+}C_2 dn_+ \\
&= \frac{N A_{++} \omega^2}{2} \left(\langle n_+^2 \rangle - \langle n_+ \rangle \right) \\
&= \frac{N A_{++} \omega^2}{2} \langle n_+ \rangle^2,
\end{aligned} \tag{5.3}$$

where ω is a probability that the meson decay into a muon and something, $P(n_+)$ is a probability of creating n mesons in the same event and A_{++} is an acceptance for a pair of positively charged mesons. For a pair of oppositely charged muons, the number is given by

$$N_{+-} = N A_{+-} \int \omega P(n_+) n_+ \omega P(n_-) n_- dn_+ dn_- = N A_{+-} \omega^2 (\langle n_+ \rangle \langle n_- \rangle). \tag{5.4}$$

Therefore, the number of the oppositely charged muon pairs is

$$N_{+-} = 2\sqrt{N_{++} N_{--}} \frac{A_{+-}}{\sqrt{A_{++} A_{--}}}. \tag{5.5}$$

To cancel the charge dependence of the acceptance, so-called "Image cut" is applied. The cut requires a charge-symmetrical acceptance to trigger hodoscopes which are fired. Technically, the cut is the same as "Trigger validation cut", but the extrapolation is performed after reversing muons' charge.

Fig. 5.6 shows invariant mass distributions of muon pairs obtained from real data along with the dimuon mass distribution. The red, green and black lines represent a $\mu^+\mu^+$, $\mu^-\mu^-$ pairs and the combinatorial background estimated with the like-sign method.

5.4.3 Reproduction of the real data by MC and the combinatorial background data

TGeant with Pythia8 was used for the background estimation. The pion PDF GRVPI0 [112] and the nucleon PDF GRV98lo [113] were employed since it is evident that the parametrisations of a pion and nucleon PDFs are correlated, GRV98lo which was used for the extraction of the GRVPI0 from DY data was selected.
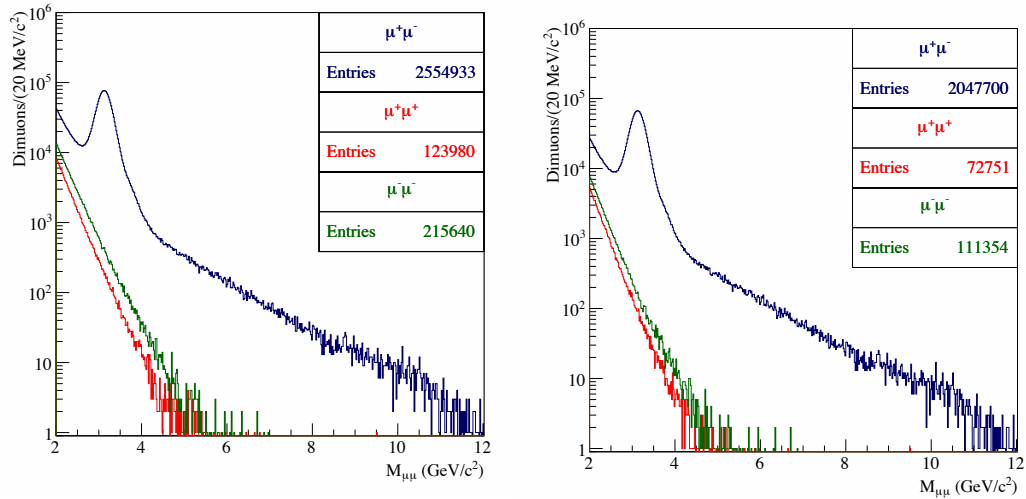
(a) Invariant mass distributions of muon pairs with the selection criteria.

(b) The same as left with the image cut.
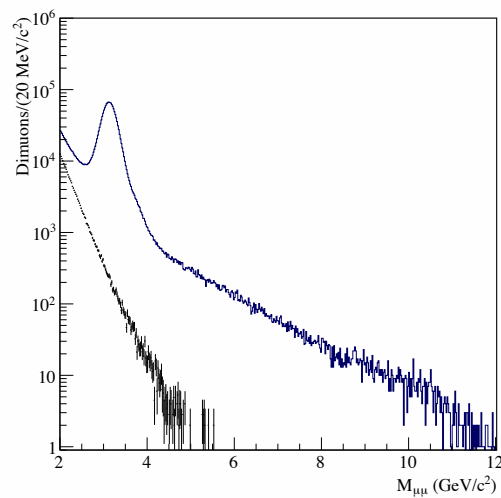
(c) A combinatorial background.

Figure 5.6: Invariant mass distributions of dimuons. The red, green lines represent $\mu^+\mu^+$ and $\mu^-\mu^-$ pairs. The black line indicates a combinatorial background estimated with the like-sign method applying the image cut. The blue lines show the dimuon mass distribution.
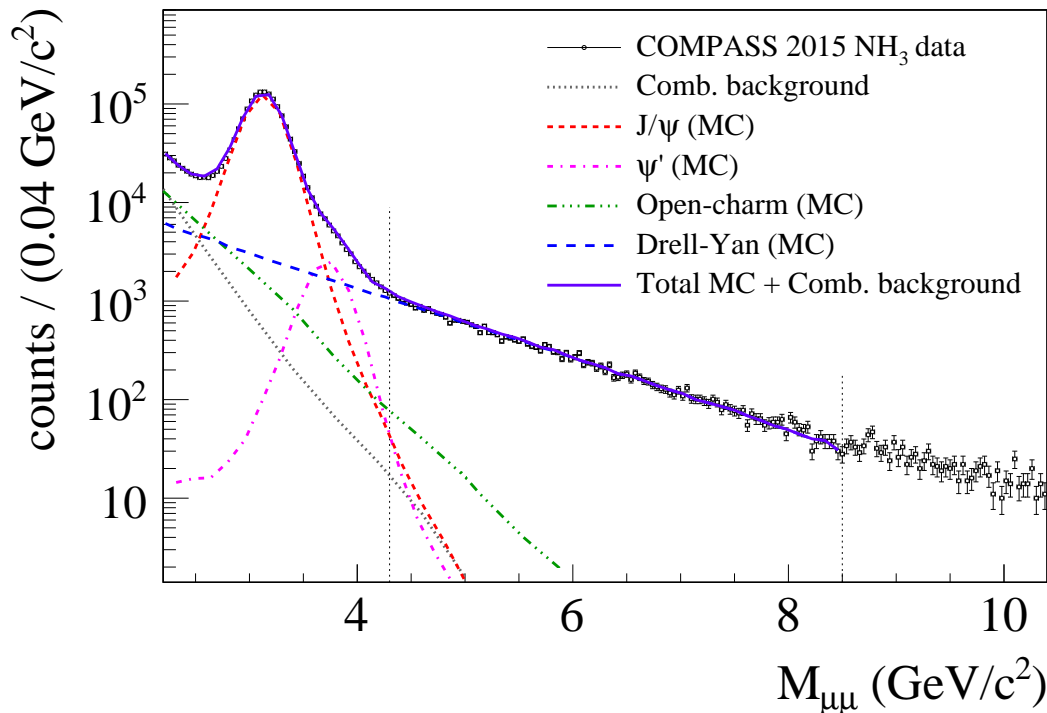
Figure 5.7: The dimuon mass distributions from the real data and reconstructed one from MC and CB data. The black points indicate the dimuon mass spectrum. The black dashed line represents CB estimated from the real data with the like-sign method. The dashed blue, red, pink and green lines show the spectrum of DY, J/ψ, ψ' and OC processes from MC data. The solid blue line represents the reconstructed spectrum. The vertical dashed line indicate the dimuon mass range from $4.3\,\mathrm{GeV}/c^2$ to $8.5\,\mathrm{GeV}/c^2$.

DY, J/ψ, ψ', and OC events were generated independently, and CB was estimated from the real data with the like-sign method. MC data were merged to reproduce the real data by the following steps:

1. A fraction of HMDY and LMDY events was determined by fitting to the real data in a dimuon mass range from $6\,\mathrm{GeV}/c^2$ to $9\,\mathrm{GeV}/c^2$.

2. A contribution of J/ψ, ψ', OC is determined by fitting to the dimuon mass distribution obtained from the real data in $2\,\mathrm{GeV}/c^2$ to $9\,\mathrm{GeV}/c^2$. DY-MC and CB are introduced to the fitting as a fixed parameter.

In both steps, fittings are carried out with the log likelihood method.

Fig. 5.7 shows a dimuon mass distribution reproduced dimuon distribution with one obtained from the real data. MC and CB data succeeded to reproduce the real data well. The slight difference in the dimuon mass larger than 8.5 GeV came from Υ. Table 5.7 summarises results of the background estimation for various dimuon mass range. Finally, the mass range from $4.3\,\mathrm{GeV}/c^2$ to $8.5\,\mathrm{GeV}/c^2$ with a $4\,\%$ of statistical contamination was chosen.

5.5 Distribution of kinematic variables

kinematic variables of x_N, x_π, x_F, q_T and $M_{\mu\mu}$ defined in Sec. 2.3 obtained with the selection criteria in the dimuon mass range from $4.3\,\mathrm{GeV}/c^2$ to $8.5\,\mathrm{GeV}/c^2$ are shown in Fig. 5.8. A mean value, standard deviation of the variable are shown in each plot. Fig. 5.9 shows a

Table 5.7: Results of the background estimation. The values in the Data column are the number of events from the real data. The background column shows a ratio of DY-MC events to sum of the MC and CB events. The upper cut off of $8.5\,\mathrm{GeV}/c^2$ was given due to an observation of contamination from Υ events.

Mass (GeV/c^2)	Data	DY	J/ψ	ψ'	OC	CB	Background
4.0 - 8.5	44245	40412	1054	1863	1679	319	11 %
4.1 - 8.5	39089	37186	608	722	1347	233	7 %
4.2 - 8.5	34986	34213	415	310	1106	176	6 %
4.3 - 8.5	31721	31448	242	139	814	126	4 %
4.4 - 8.5	28916	28907	164	65	656	91	3 %
4.5 - 8.5	26453	26583	120	33	557	75	3 %
4.6 - 8.5	24287	24434	94	17	440	60	2 %
4.7 - 8.5	22265	22451	64	9	332	45	2 %
4.8 - 8.5	20383	20593	53	8	274	28	2 %
4.9 - 8.5	18779	18871	41	3	199	17	1 %
5.0 - 8.5	17202	17320	39	3	149	15	1 %

correlation between x_π and x_p. Fig. 5.10 is a correlation map between the kinematic variables. Mean values of $x_p i$ and x_N are 0.50 and 0.17, respectively, hence valence quarks are dominant in the measurement. 5.4 % of events have negative x_F.

5.6 MC study in the high mass range

Simulation enables us to study a resolution of the spectrometer for the kinematic variables, a quality of the reconstruction, and an acceptance.

A dedicated MC study was performed on these topics. It was the same as the one for the background estimation except for the event generator Pythia6. Only DY events in a dimuon mass range of $3.5\,\mathrm{GeV}/c^2$ to $9.0\,\mathrm{GeV}/c^2$ are generated and the same selection criteria as the one for the real data is applied. The dimuon mass range is for redundancy of the reconstruction although the selection of the dimuon mass from $4.3\,\mathrm{GeV}/c^2$ to $8.5\,\mathrm{GeV}/c^2$ was required in any case.

5.6.1 Resolution of the kinematic variables

Resolution for the kinematic variables should be known to optimise the selection criteria. The study can be performed by comparing a variable from generated MC data (MC-truth) and a reconstructed variable. The difference between the reconstructed and the MC-truth is calculated. Two definitions of the resolution are tested: a Root Mean Square (RMS) of the difference and a fit with two Gaussians to the distribution of the differences. For the latter case, a narrower and higher Gaussian is called the leading Gaussian while the other one is called the tail Gaussian. The leading Gaussian represents dominantly to the spectrometer's resolution of the parameter. Since the resolution does not consider the tail Gaussian in the latter case, the obtained resolution is optimistic. Results for the kinematic variables are summarised in Table 5.8.

5.6.2 An event migration from one cell to another

As discussed above, the z coordinate resolution of the interaction point was about $10\,\mathrm{cm}$. It means that events reconstructed in the cell are composed of not only events generated in the
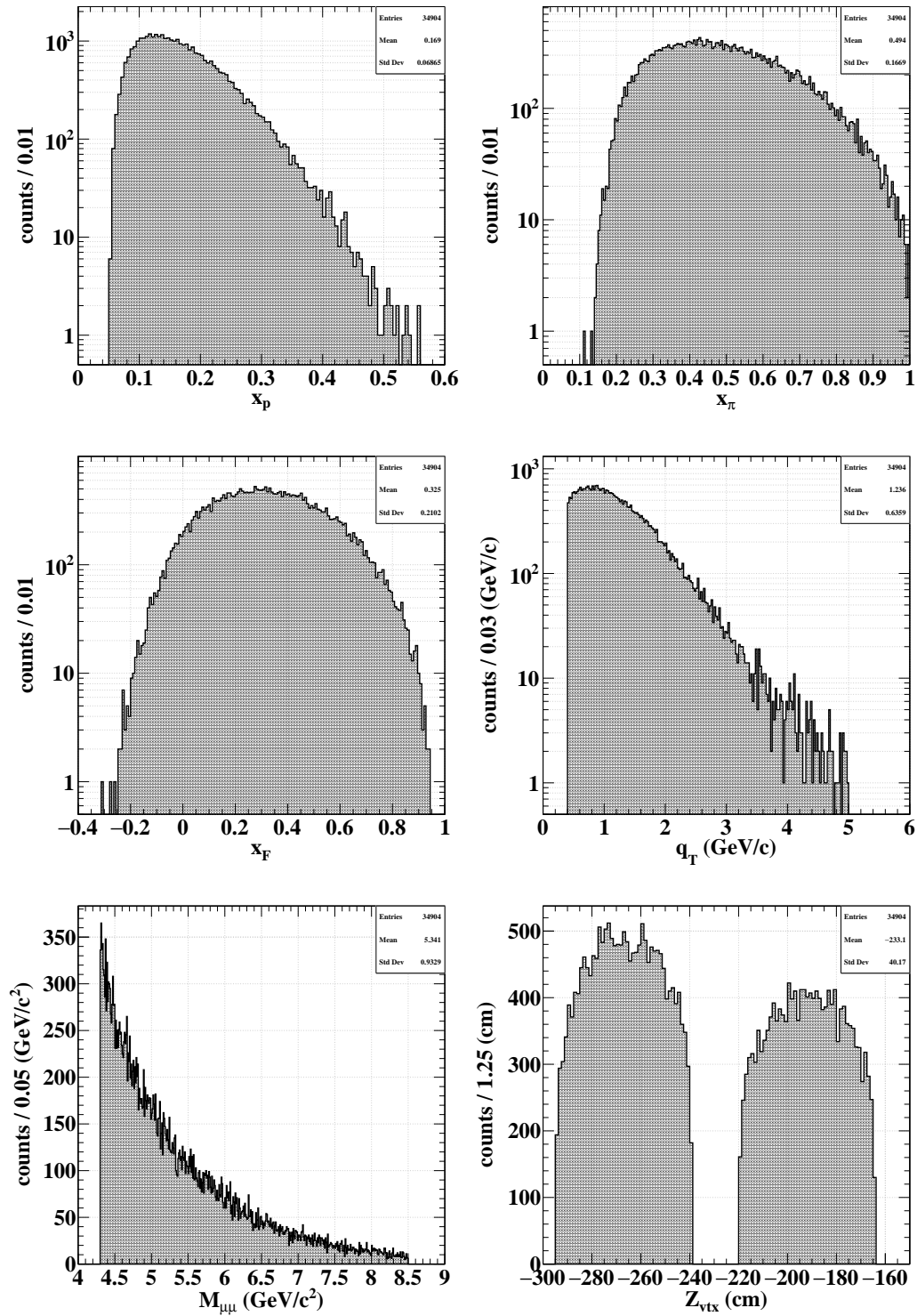
Figure 5.8: Kinematic distributions of x_N, $x_\pi x_F$, q_T and $M_{\mu\mu}$ in a dimuon mass range from $4.3\,\mathrm{GeV}/c^2$ to $8.5\,\mathrm{GeV}/c^2$.
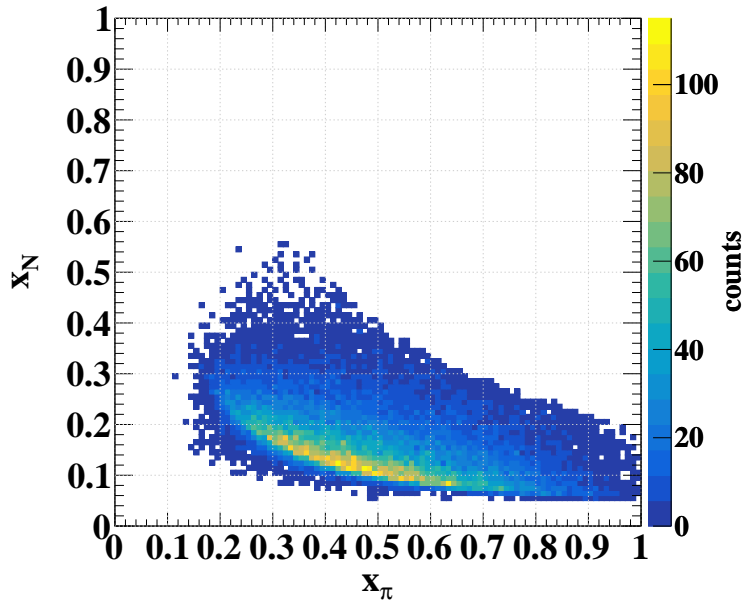
Figure 5.9: A phase space of x_π and x_N in the dimuon mass range from $4.3\,\mathrm{GeV}/c^2$ to $8.5\,\mathrm{GeV}/c^2$.
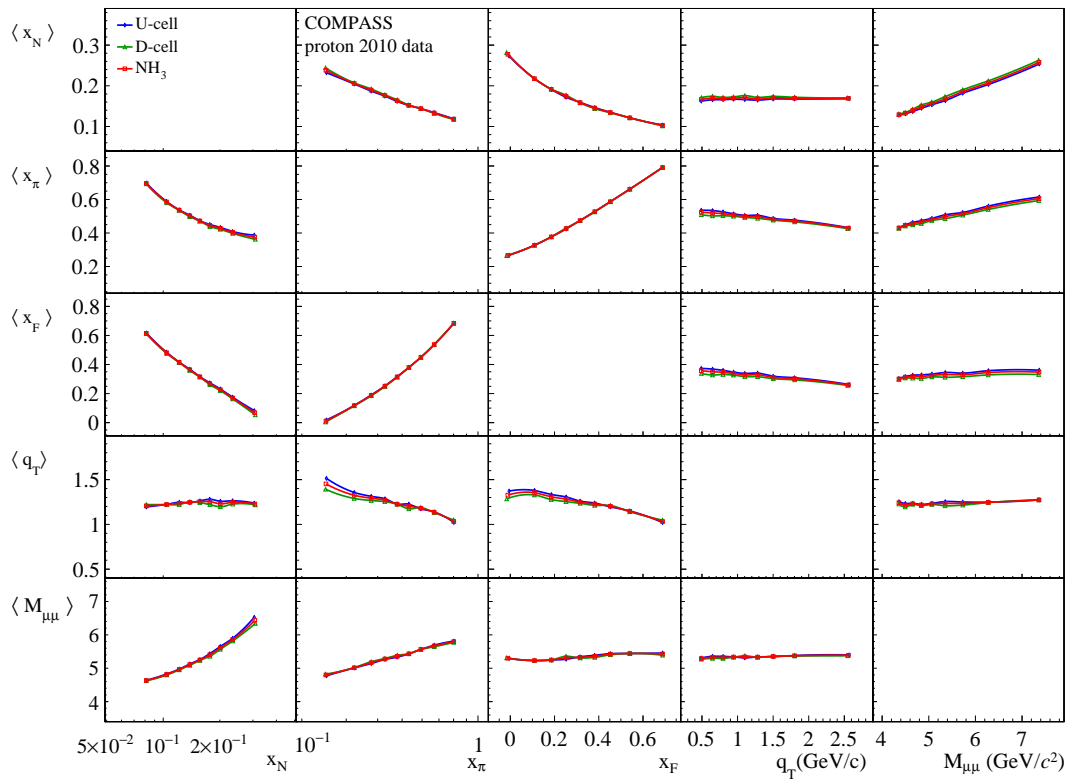
Figure 5.10: Correlations between Kinematic variables x_N, $x_\pi x_F$, q_T and $M_{\mu\mu}$ in the range $4.3 < M_{\mu\mu} < 8.5\,\mathrm{GeV}/c^2$. The blue, green lines show correlations of events in the upstream and the downstream cells while the red lines show for both cells.

Table 5.8: Resolutions for main kinematic variables and angles.

Variable	RMS	σ of the leading gaussian
x_{vtx} (cm)	0.04039	0.0279
y_{vtx} (cm)	0.03823	0.02396
z_{vtx} (cm)	10.97	8.22
$M_{\mu\mu}$ (GeV/c^2)	0.19068	0.18146
x_N	0.01863	0.01104
x_π	0.01314	0.00896
x_F	0.01951	0.0139163
q_T (GeV/c)	0.1487	0.1070
ϕ_S (rad)	0.19333	0.09005
ϕ_{CS} (rad)	0.19756	0.09461
θ_{CS} (rad)	0.0263969	0.01719

Table 5.9: The ratio of reconstructed events of the upstream and the downstream cell from MC data. The columns are the region that events are generated. About 95 % the generated event is reconstructed as events from the same cell.

Generated in	Reconstructed in	
	U-celll (%)	D-cell (%)
Upstream of U-cell	2.157	0.001665
U-cell	95.71	1.296
Gap of the cells	1.7	3.271
D-cell	0.1632	94.24
Downstream of D-cell	0	0.8588
Anything else (R > 2 cm)	0.2714	0.3311

target cell but also outside the cell. This effect of an event migration is estimated with MC simulation. Fig. 5.11 shows z coordinate distribution of reconstructed interaction points from MC data. Each distribution except black one is generated in different regions: the upstream cell, the downstream cell, liquid helium regions, and a region with $r > 2$ cm. The liquid helium regions are divided into three: an upstream of the upstream cell, a downstream of the downstream cell, and a gap between the cells. The black line shows the sum of all the coloured spectrum. Table 5.9 summarises a level of the event migration for each cell. More than 90 % of reconstructed events in each cell was generated in the cell. The largest contamination in each cell was events generated between the cells and was about 1.6 % for the upstream and 3.9 for the downstream, respectively. A successful vertex reconstruction was obtained, and the cells were identified well.

5.6.3 Acceptance

Acceptance is a ratio of the number of detected events to generated events. Since the COMPASS spectrometer covers from 30 mrad to 180 mrad, some muons emitted outside the coverage cannot be detected. In the MC simulation, using information on such generated but not detected events, the acceptance can be estimated. Note that the number of reconstructed events includes an efficiency of the reconstruction. Fig. 5.12 shows the estimated acceptance including a reconstruction efficiency of x_N, x_π, x_F, q_T, $M_{\mu\mu}$, $\cos(\theta_{CS})$, ϕ_{CS} and ϕ_S. The
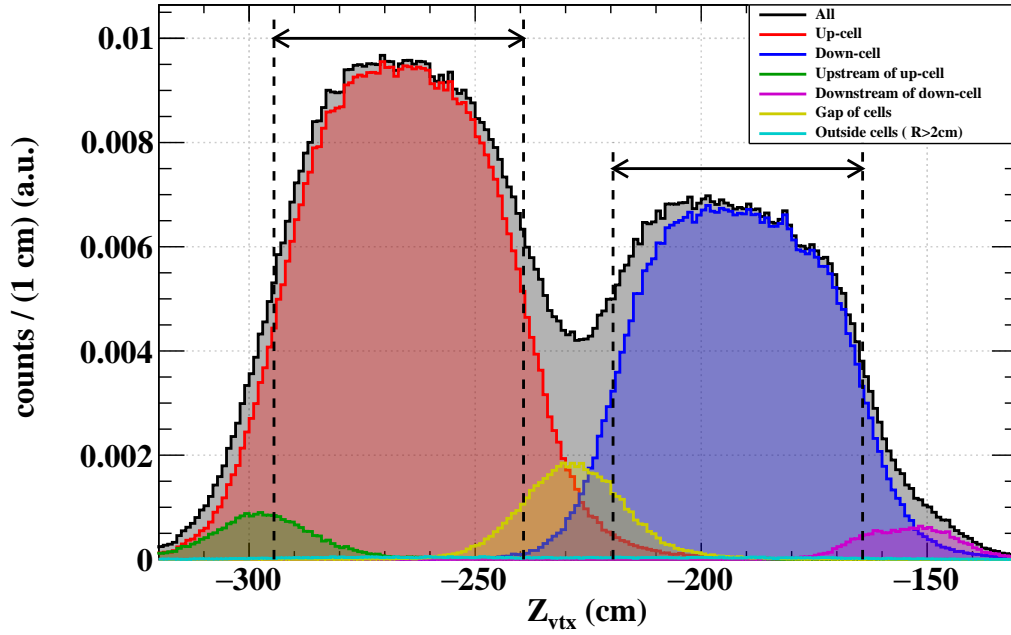
Figure 5.11: z distribution of reconstructed interaction vertices from the MC data for each region of the target area. The black line is the reconstructed distribution with the selection criteria except for the target cut in the z-axis. The other lines are the reconstructed distributions with the additional selection of a region. The two horizontal arrows indicate the upstream and the downstream cell region.

large error bars of q_T at the end of spectra are due to low statistics since the number of events decrease more or less exponentially as q_T increases.

5.7 Dilution factor

The dilution factor of ammonia as the proton target 0.176 needs to be modified as discussed in Sec. 4.2.1:

$$f_{\rm p}^{\rm DY} = \frac{n_{\rm p}\sigma_{\pi-{\rm p}}^{\rm DY}}{n_{\rm p}\sigma_{\pi-{\rm p}}^{\rm DY} + \sum_{\rm A} n_{\rm A}\sigma_{\pi-{\rm A}}^{\rm DY}}, \tag{5.6}$$

where $n_{\rm p(A)}$ is the number of polarisable protons (nuclei) in the target region. $\sigma_{\pi-{\rm p(A)}}^{DY}$ represents a differential cross section of the DY process with a pion and a proton (nuclei).

A parton-level Monte-Carlo program, MCFM [114] estimates the differential cross section of the DY process. Some modifications are applied to the MCFM to treat pion beams. To have a reasonable processing time, the differential cross section is calculated in a 3D grid, $M_{\mu\mu}$, q_T and x_N. A q_T cut off of $0.1\,{\rm GeV}/c$ is applied to minimise handling of divergences when $q_T \to 0$. The range of the dimuon mass is from $3.5\,{\rm GeV}/c^2$ to $9.5\,{\rm GeV}/c^2$, of the x_N is from 0.01 to 1.0 and of the q_T is from $0.1\,{\rm GeV}/c$ to $10\,{\rm GeV}/c$. After the simulation, a smoothing is performed to clean up fluctuation which affects the cross-section in a region close to the upper and the lower limits of the acceptance.

The smoothing was based on the one equipped in ROOT which uses a kernel algorithm. The first smoothing is performed on the (q_T, x_N) projections of the dilution factor and the second on the $(M_{\mu\mu}, x_N)$ projections. Influence of the smoothings on the dilution factor is found to be small. Only around boundaries of the acceptance, does their effect go up to $10\,\%$.
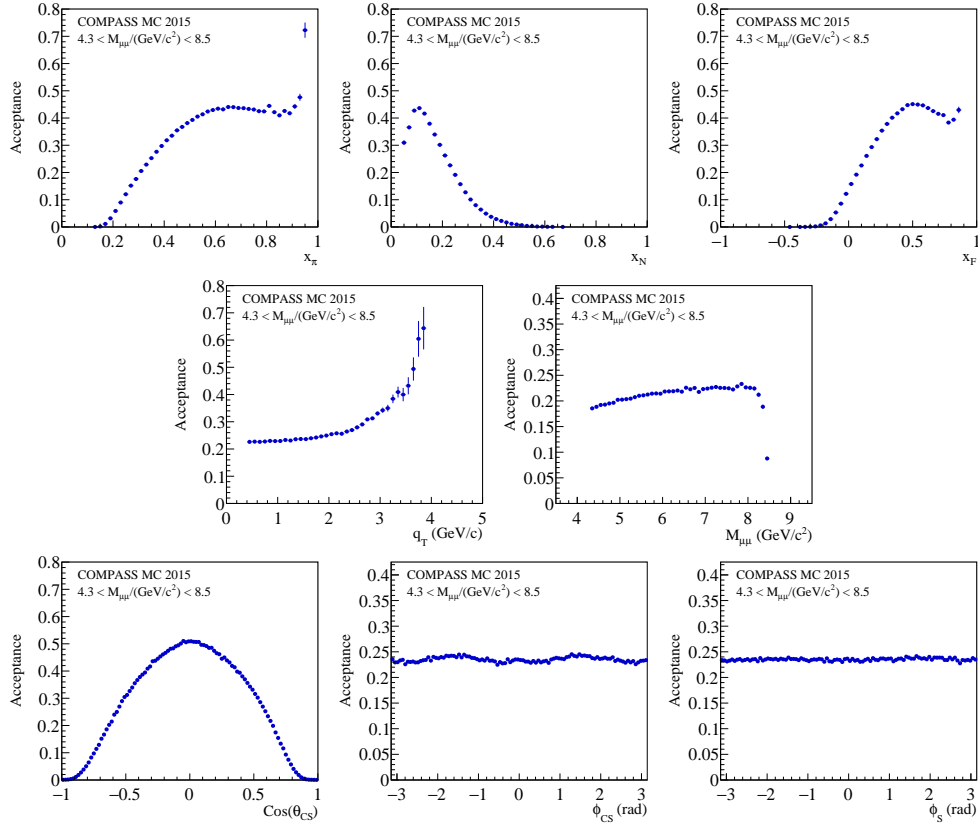
Figure 5.12: Geometrical acceptance including a reconstruction efficiency of x_N, x_π, x_F, q_T, $M_{\mu\mu}$, $\cos(\theta_{CS})$, ϕ_{CS} and ϕ_S for the COMPASS spectrometer in 2015.

Fig. 5.13 shows a correlation between a dilution factor and x_N for the DY events. The left and the right plots correspond to events in the upstream cell and the downstream cell, respectively. The obtained values are used in the asymmetry extraction (Sec. 5.9) event by event. Averaged dilution factors for the upstream and the downstream cell were 0.1969 and 0.1895, respectively.

5.8 Depolarisation factor

The depolarisation factor introduced in Eq. (2.16) with three type of functions $1+\cos^2\theta_{CS}$, $\sin^2\theta_{CS}$ and $\sin 2\theta_{CS}$ are calculated as a function of x_N, x_π, x_F, q_T and $M_{\mu\mu}$. Three values of the $\lambda = 0.5, 0.75, 1.0$ are used to study the effect of the known deviation of λ. Fig. 5.14 shows the results. An average value of θ_{CS} in each bin was extracted from data with the selection criteria. Fig. 5.15 shows ratios of the factors with respect to ones with $\lambda = 1.0$.

The obtained values are used in the asymmetry extraction (Sec. 5.9) event by event.

5.9 Asymmetry Extraction

All asymmetries in Eq. (2.15) are extracted simultaneously using an fD Weighted Extended Unbinned Maximum Likelihood (WE-UML) method [115] which had been used for the SIDIS analysis [116]. Weighting of the dilution factor and the depolarisation factor are performed event by event. Asymmetries are extracted in a kinematic bin of x_N, x_π, x_F, q_T and $M_{\mu\mu}$ integrating over all the other variables. The following likelihood with ϕ_{CS} and ϕ_S are used for fittings:
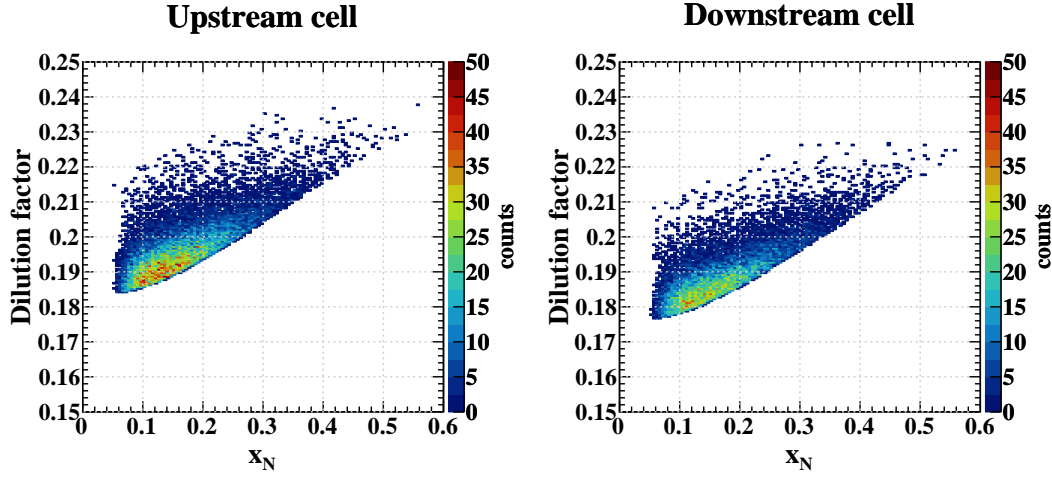
Figure 5.13: A correlation between the dilution factor and x_N for events in the upstream cell (left) and the downstream cell (right).

$$\mathcal{L} = \prod_{cell=1}^{n_{cell}=2} \left[\prod_{pol=1}^{n_{pol}=2} \left\{ \left(e^{-I_{cell}^{pol}} \prod_{n=1}^{N_{cell}^{pol}} P^{pol}(\phi_{CS,n}, \phi_{S,n}; a_{cell}^{pol}, \vec{A}) \right)^{\frac{\bar{N}}{N_{cell}^{pol}}} \right\} \right]$$

$$= \left(e^{-I_u^+} \prod_{n=1}^{N_u^+} P^+(\phi_{CS,n}, \phi_{S,n}; a_u^+, \vec{A}) \right)^{\frac{\bar{N}}{N_u^+}} \left(e^{-I_u^-} \prod_{n=1}^{N_u^-} P^-(\phi_{CS,n}, \phi_{S,n}; a_u^-, \vec{A}) \right)^{\frac{\bar{N}}{N_u^-}}$$

$$\left(e^{-I_d^+} \prod_{n=1}^{N_d^+} P^+(\phi_{CS,n}, \phi_{S,n}; a_d^+, \vec{A}) \right)^{\frac{\bar{N}}{N_d^+}} \left(e^{-I_d^-} \prod_{n=1}^{N_d^-} P^-(\phi_{CS,n}, \phi_{S,n}; a_d^-, \vec{A}) \right)^{\frac{\bar{N}}{N_d^-}}$$

$$\tag{5.7}$$

where the notation "+" and "−" indicate a positive and negative polarisation, the superscript *pol* corresponds to a direction of polarisation, up or down. The "u" and "d" means the upstream and the downstream cell, $N_{cell}^{\pm}$ means the number of dimuons with positively or negatively polarised target, $\bar{N}$ is an average number of muon pairs per kinematic bin, and n_{cell} is the number of the target cells, two. The probability density function $P^{\pm}$ and cross-section σ are written with $\vec{A}$ as a vector of asymmetries:

$$P^{\pm}(\varphi_{CS}, \varphi_S; a_{cell}^{\pm}, \vec{A}) = a_{cell}^{\pm}(\varphi_{CS}, \varphi_S; \vec{A}) \cdot \sigma^{\pm}(\varphi_{CS}, \varphi_S; \vec{A}), \tag{5.8}$$

with

$$\sigma^{\pm}(\varphi_{CS}, \varphi_S; \vec{A}) = 1 + A_U^{\cos\varphi_{CS}} + A_U^{\cos 2\varphi_{CS}} \pm \sum_{i=1}^{3} \langle P_{T,cell} \rangle f D_{[w_i(\varphi_{CS}, \varphi_S)]} A_T^{w_i(\varphi_{CS}, \varphi_S)}, \tag{5.9}$$

where $\langle P_T \rangle$ is a transverse polarisation. The asymmetries for unpolarised DY $A_U^{\cos\varphi_{CS}}$ and $A_U^{\cos 2\varphi_{CS}}$ are defined in Sec. 2.3.2. And $I_{cell}^{\pm} = \int\int d\phi_{CS} d\phi_S P^{\pm}(\phi_{CS}, \phi_S; a_{cell}^{\pm}, \vec{A})$ is a probability density normalisation coefficient given by the expected number of dimuons, $a_{cell}^{\pm}(\phi_{CS}, \phi_S)$ involves the unpolarised cross-section.
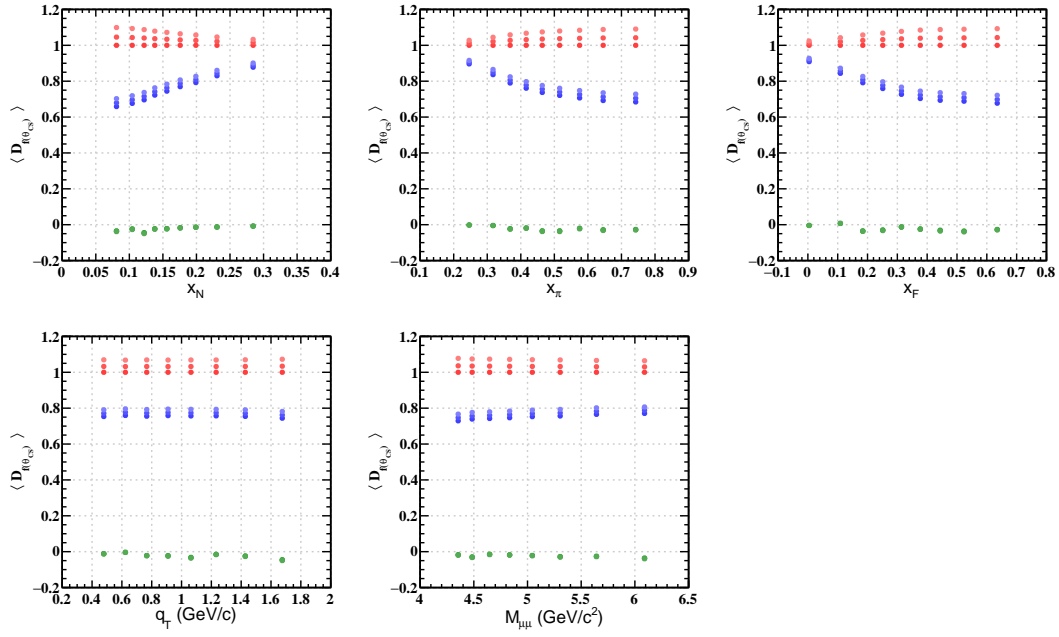
Figure 5.14: Depolarisation factors as a function of x_N, x_π, x_F, q_T and $M_{\mu\mu}$. Red, blue and green points indicate the factor with $D(1 + \cos^2\theta_{CS})$, $D(\sin^2\theta_{CS})$ and $D(\sin 2\theta_{CS})$. The colour strength of points represents the factor with the $\lambda = 1.0, 0.75$ and 0.5.
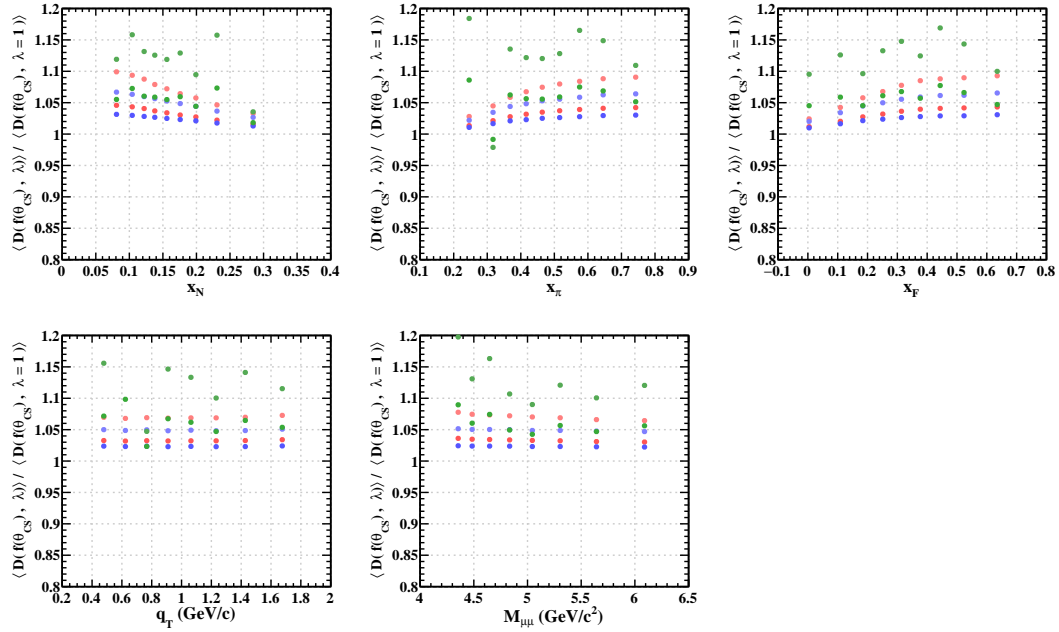
Figure 5.15: Ratios of depolarisation factors to ones with $\lambda = 1.0$ as a function of x_N, x_π, x_F, q_T and $M_{\mu\mu}$. Red, blue and green points show the factor with $D(1 + \cos^2\theta_{CS})$, $D(\sin^2\theta_{CS})$ and $D(\sin 2\theta_{CS})$. The colour strength of points indicate the factor with the $\lambda = 0.75$ and 0.5.

Contributions of the term for the positively and negatively polarised target in Eq. (5.7) are weighted with powers of $\bar{N}/N_{cell}^{\pm}$ to reduce possible false asymmetries and acceptance effects. The parameters $a_{cell}^{\pm}$ are treated as a free parameter for an unpolarised part and difference of luminosity in the pair of sub-periods. This treatment is analogous to the analysis of SIDIS. Weights of the dilution factor f (Sec. 5.7) and the depolarisation factor $D(\theta_{CS})$ (Sec. 5.8) are applied event by event to the cross-section $\sigma^{\pm}$. The values of polarisation are given cell by cell and period by period [3].

To have similar statistics in bins of kinematic variables in an asymmetry extraction, the following binning configurations are defined:

- x_N: 0.0, 0.13, 0.19, 1.0

- x_π: 0.0, 0.40, 0.56, 1.0

- x_F: -1.0, 0.21, 0.41, 1.0

- q_T: 0.4, 0.9, 1.4, 5.0 GeV/c

- $M_{\mu\mu}$: 4.30, 4.75, 5.50, 8.50 GeV/c^2.

The results are shown in Sec. 5.10, and some tests and study of the systematics are shown in Sec. 5.11.

5.10   The result

The extracted asymmetries using the WE-UML method with the binning introduced in Sec. 5.9 as a function of the kinematic variable x_N, x_π, x_F, q_T and $M_{\mu\mu}$ are shown in Fig. 5.16. Statistical errors are indicated by the black lines on the red points while the red horizontal bars represent systematic errors.

Fig. 5.17 shows asymmetries averaged over all kinematic variables. The average asymmetry $A_T^{\sin\phi_S}$ is consistent with zero within the standard deviation of the total uncertainty.

5.11   Systematic study

Asymmetries are extracted with different configurations and compared to the asymmetries presented in Sec. 5.10 to check whether the tested configurations introduces a clear bias or not. The following subjects are carried out:

1. compatibility check of the periods

2. check of an impact of the bad spill and run rejection

3. test of tighter target cut for z coordinate of the primary vertex than that in the selection criteria described in Sec. 5.3

4. test of relaxed q_T cut than that in the selection criteria described in Sec. 5.3

5. test of statistically balanced periods

6. comparison to an UML method

---

[3]Polarisation is not given event by event since if statistics of the cells are not balanced, values event by event can give bias.
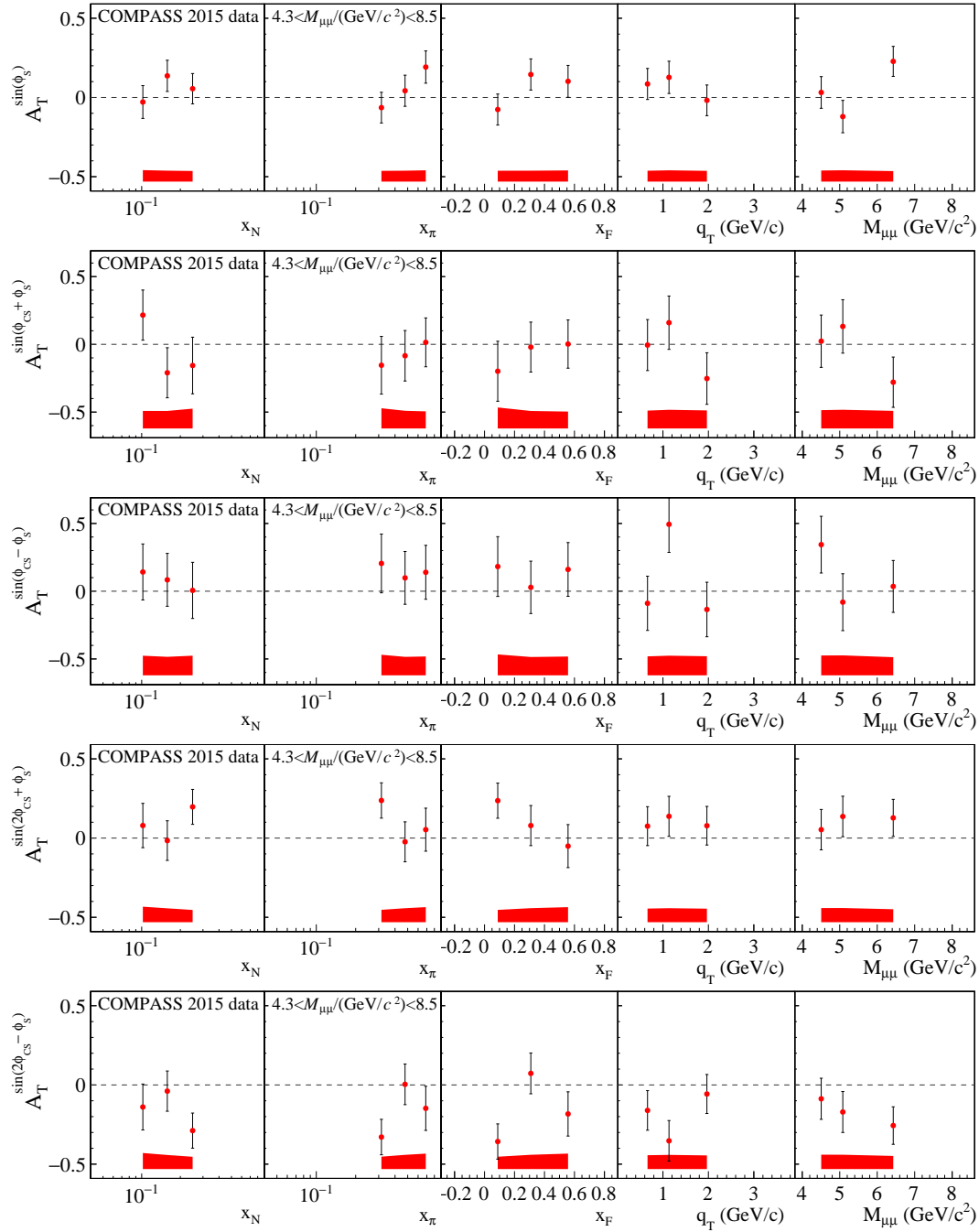
Figure 5.16: Asymmetries extracted with the WE-UML method as a function of x_N, x_π, x_F, q_T and $M_{\mu\mu}$. Each black vertical line corresponds to statistical error, and systematic errors are indicated by red horizontal bars.
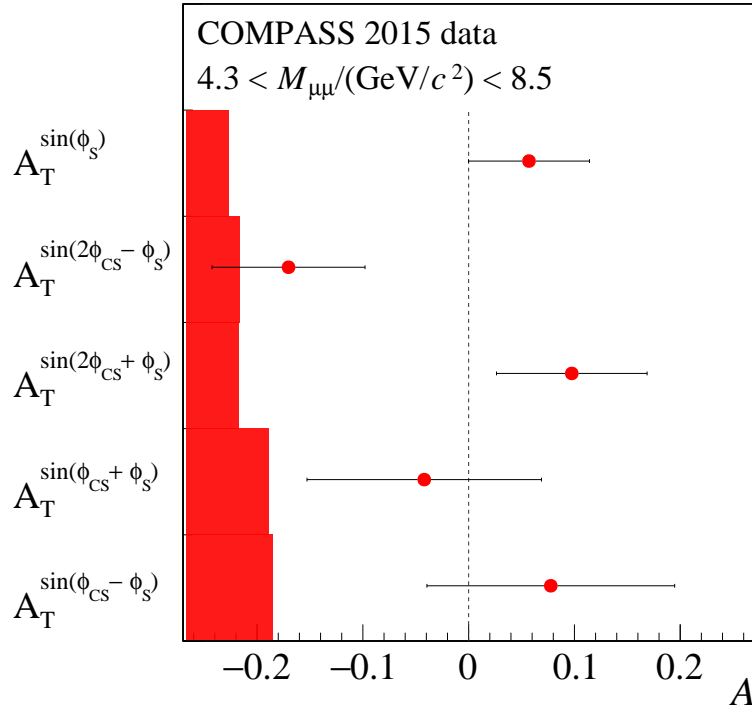
Figure 5.17: Asymmetries integrated over all the kinematic variables.

7. comparison of asymmetries extracted from the top segment of the spectrometer and that from bottom segment

8. comparison of asymmetries extracted from the left segment of the spectrometer and that from right segment

Differences between the asymmetries and asymmetries in the tested configurations are not significant according to their pull distributions.

5.11.1 Compatibility check of the periods

Asymmetries integrated over all the kinematic variables extracted period by period are shown in Fig. 5.18. The red lines show weighted mean with their uncertainty. No large discrepancy among the periods was observed.

Fig. 5.19 and Fig. 5.20 show asymmetries extracted period by period with a kinematic bin of x_N, x_π, x_F, qT and $M_{\mu\mu}$. Averaged values over the bins are written in the plots. The asymmetries and the averaged values are well compatible over a year. Pull distributions of the asymmetries are shown in Fig. 5.21. The pulls are calculated with the following formula:

$$\left(\langle A \rangle_i - \langle A \rangle_{all}\right) \sqrt{\sigma^2_{\langle A \rangle_i} - \sigma^2_{\langle A \rangle_{all}}}, \tag{5.10}$$

where $\langle A \rangle_{all}$ is the averaged asymmetry over all data, $\langle A \rangle_i$ is the asymmetry averaged over ith period, and $\sigma_{\langle A \rangle_i}$ and $\sigma_{\langle A \rangle_{all}}$ are standard deviations of $\langle A \rangle_i$ and $\langle A \rangle_{all}$. The 135 entries in each histogram correspond to the different bins and periods: (the number of kinematic variables) $\times$ (the number of bins) $\times$ (the number of periods) $= 5 \times 3 \times 9$. Mean value and RMS of the pull distributions are around -0.03 and 1. These means the pulls are consistent with the standard normal distribution, therefore the results of the periods are compatible each other. The final asymmetries are obtained by averaging over asymmetries extracted from period by period with weighting of power of $\bar{N}/C_c^{\pm}$ as presented in Sec. 5.9.
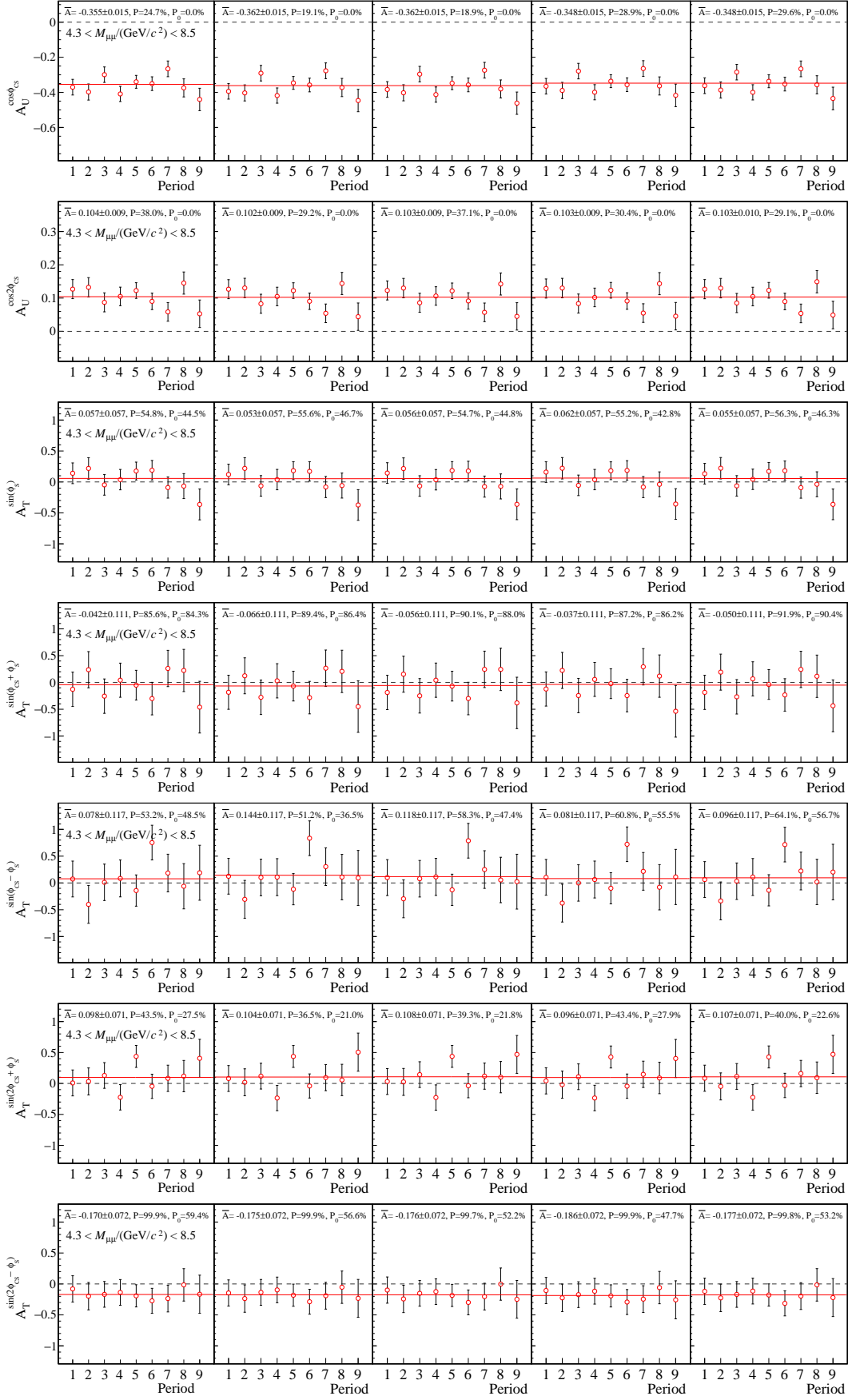
Figure 5.18: Comparisons of asymmetries averaged over all kinematic variables period by period. The columns correspond to averaged asymmetry over a kinematic bin of x_N, x_π, x_F, qT and $M_{\mu\mu}$. The red lines show a result of a fitting with a constant function.
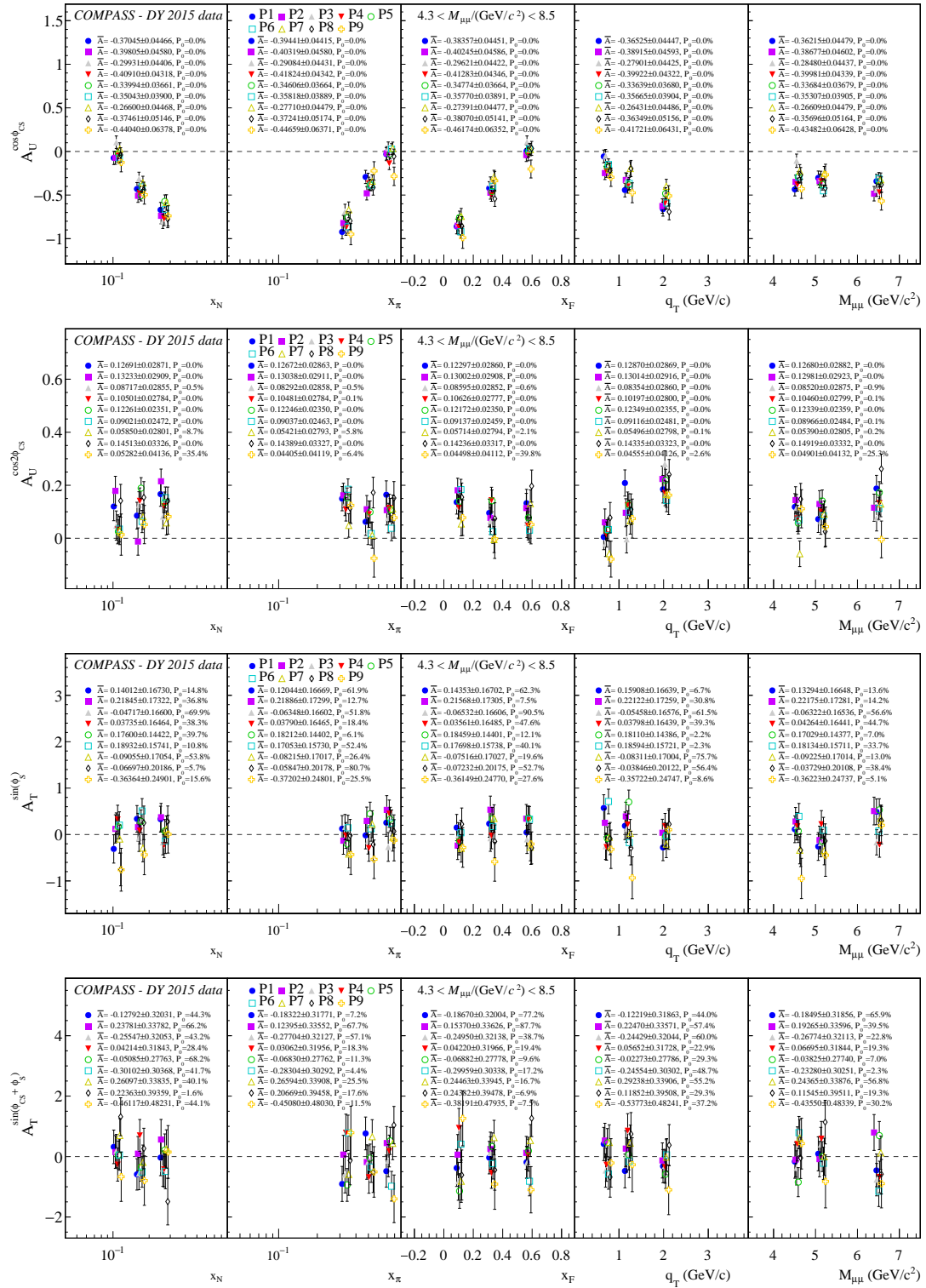
Figure 5.19: Comparisons of asymmetries extracted period by period with kinematic bins. The legends in the plots show a correspondence between a marker and a period.
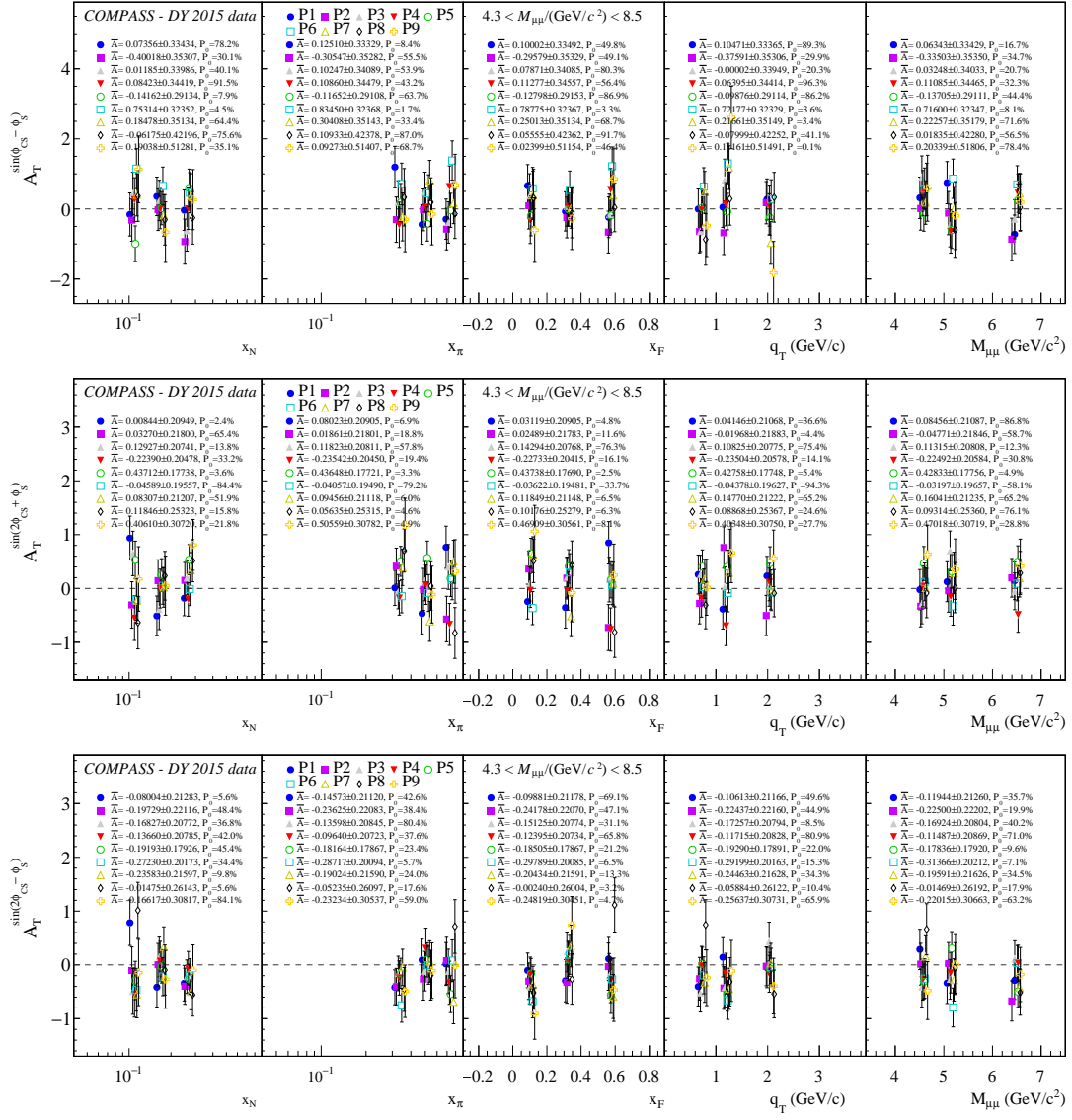
Figure 5.20: Comparisons of asymmetries with kinematic bins period by period. The legends in the plots show a correspondence between a marker and a period.
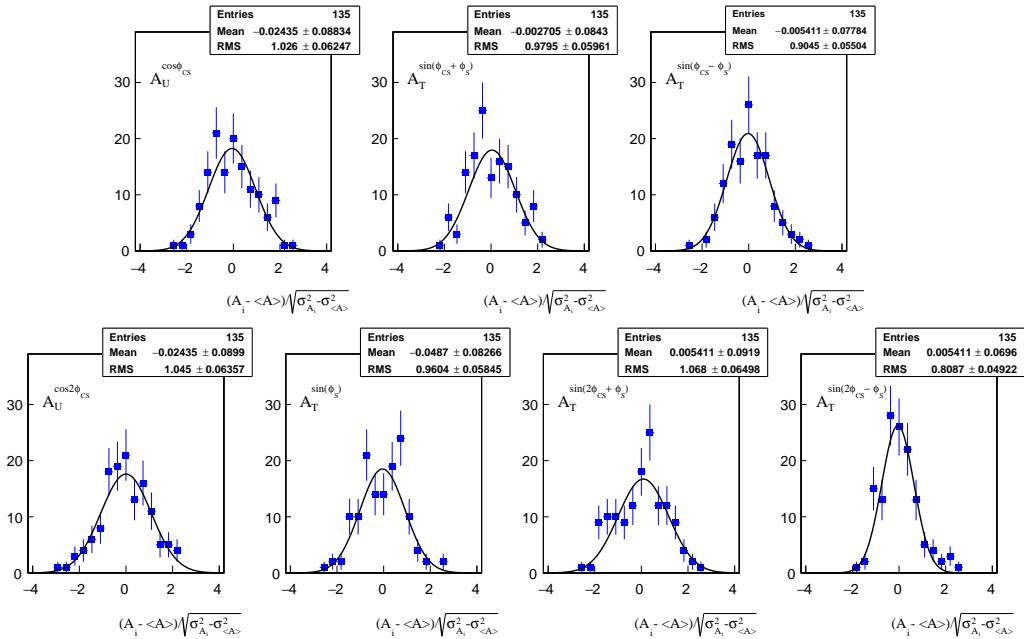
Figure 5.21: Pull distributions of asymmetries for a compatibility check of the periods.

5.11.2 Test of the bad spill rejection

Asymmetry extractions without the bad spills and runs rejection are performed to check the impact of the rejection on the asymmetry extraction as shown in Fig. 5.22. The filled and open points are asymmetries with and without the rejection. Asymmetries with the rejection are larger than those without the rejection, but the differences are smaller than statistical errors. Fig. 5.23 shows "pseudo" pull distributions witch is defined as

$$\frac{A_{1,i} - A_{2,i}}{(\sigma_{A_{1,i}} + \sigma_{A_{2,i}})/2}. \tag{5.11}$$

$A_{2,i}$ refers the asymmetry in Sec. 5.10. The distribution contains the difference between values with a normalisation of the statistical errors. The RMSs of the pseudo pulls are about 0.46 in units of a standard deviation.

5.11.3 Test of tight target cut

Migration of events to the cell is observed as discussed in Sec. 5.6.2, it is worth checking whether a tighter target cut gives different results or not. The tight target cut shrinks the target region in z coordinate for both sides by 5 cm. Hence the tight cut requires a z coordinate of the interaction point to be in -289.5 cm to -244.3 cm or -214.5 cm to -169.3 cm. The tight cut additionally rejects more than 14 % of events. Fig. 5.24 shows a comparison between the asymmetries with and without the tight cut. An impact of the tight cut is found to be smaller than statistical uncertainty, therefore there is no reason to let the target cut tighter. Psuedo pull distributions are shown in Fig. 5.25. RMS of the distributions is about 0.4.

5.11.4 Test of relaxed q_T cut and other selections

In the selection criteria, $q_T > 0.4$ GeV/c was required to have good angular resolution. Asymmetry extractions with a relaxed q_T cut, which is a requirement of $q_T > 0.1$ GeV/c, are carried out to see the impact of the relaxed cut as Fig. 5.26 shows. The first points of asymmetry in q_T bins get closer to zero at least for the $A_T^{\sin(2\phi_{CS}+\phi_S)}$ and the $A_T^{\sin(2\phi_{CS}-\phi_S)}$. A simple idea that the TSAs will vanish when $q_T \to 0$ explains reasonably. The points in the remaining asymmetries are not the case, and these can be due to statistical errors. "Psuedo" pull distributions of these tests are shown in Fig. 5.27. RMS of the distributions is about 0.36 in units of a standard deviation.

In addition to the relaxed q_T cut, some tests of selections were carried out. For example, a test of a relaxation of beam-decay-muons rejection criteria was tried using some combination of the θ cut and a cut of the middle trigger with different binnings. No significant biases were found from these tests.

5.11.5 A test of statistically balanced periods

If statistics of given sub-periods are significantly different, the difference can introduce a bias to the asymmetries. Such situation is possible if total flux of the beam of a sub-period is significantly different from one of the other sub-period. This is a test of analysing statistically balanced sub-periods. To obtain statistically balanced sub-periods, some events at the bigging or the end of sub-period which has more data are ignored. About 10 % of all events are rejected. By applying this rejection, a difference of the total beam flux between sub-periods gets smaller. Fig. 5.28 shows the comparison. The obtained asymmetries are stable, and no bias is found. The pseudo pulls are shown in Fig. 5.29 and their RMS are about 0.33.
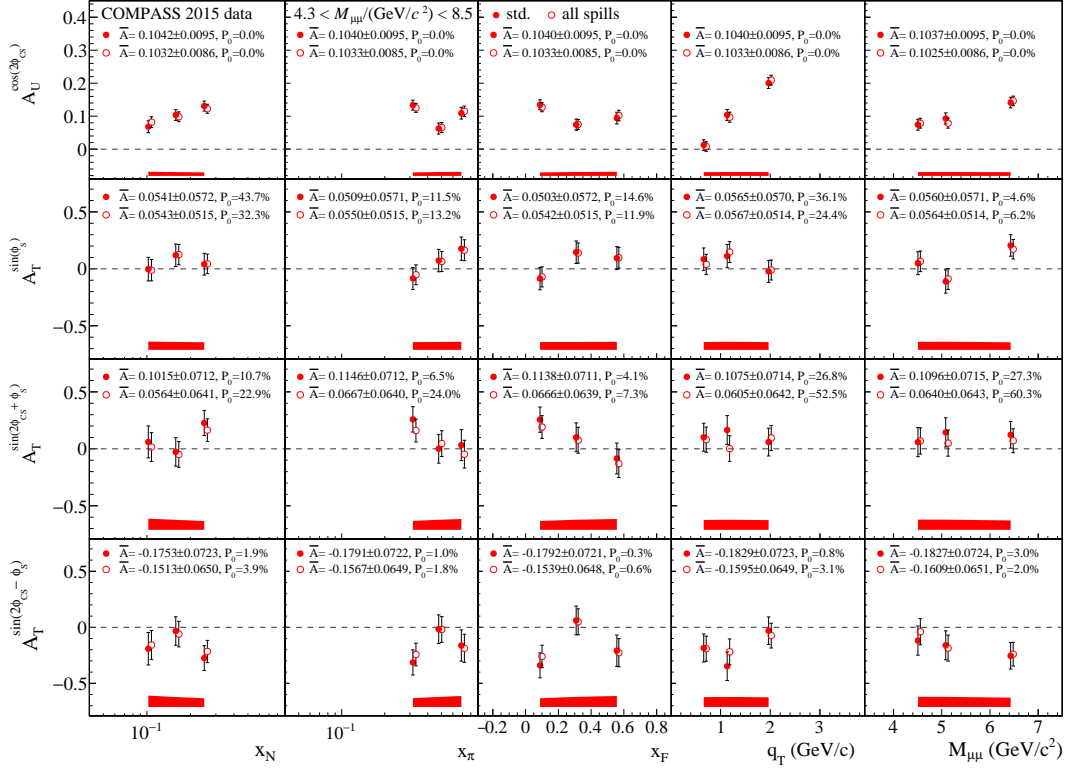
Figure 5.22: Comparison of asymmetries with and without the bad spill rejection. The filled and open dots indicate the asymmetries with and without bad spill rejection, respectively.
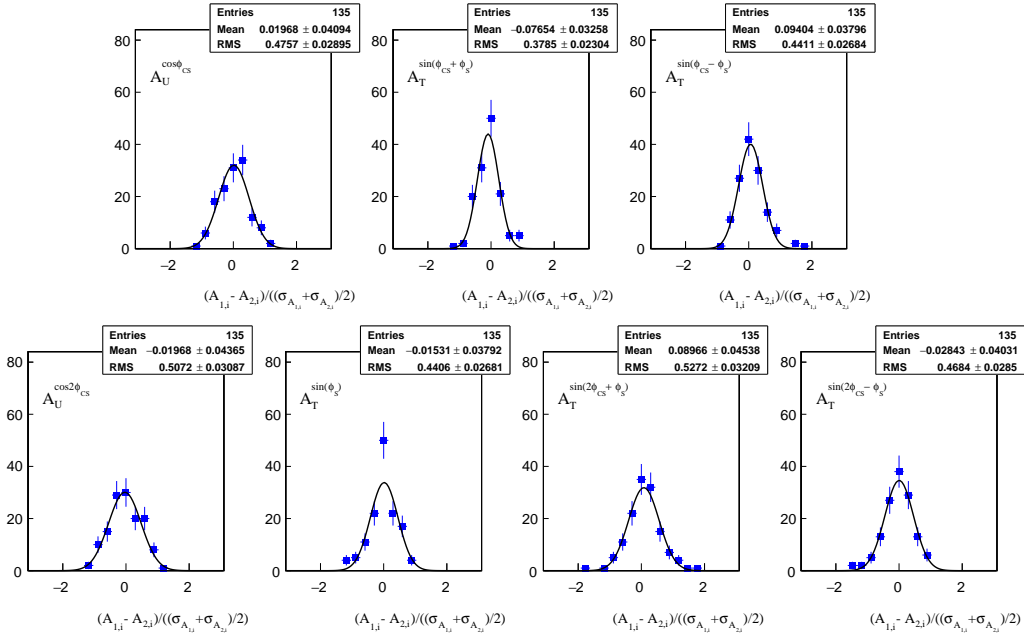
Figure 5.23: Pseudo pull distributions for the test of bad spill rejection.
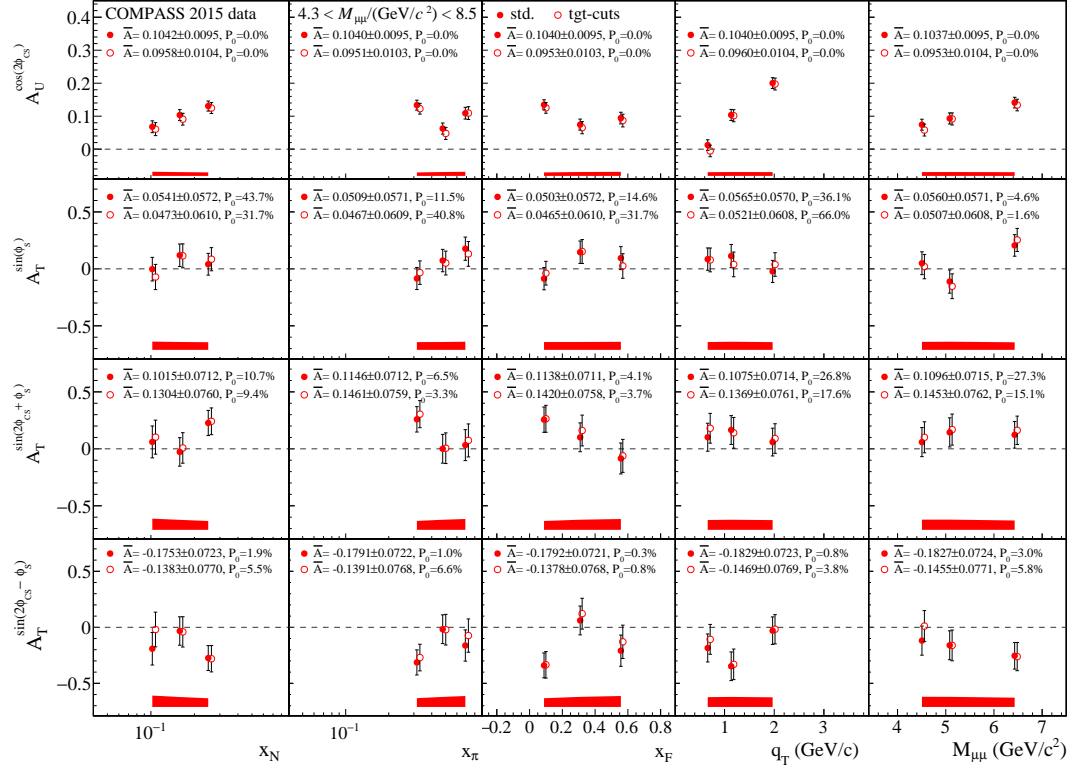
Figure 5.24: Comparison of asymmetries with and without the tight target cut. The filled and open dots represent the asymmetries with and without the tight target cut, respectively.
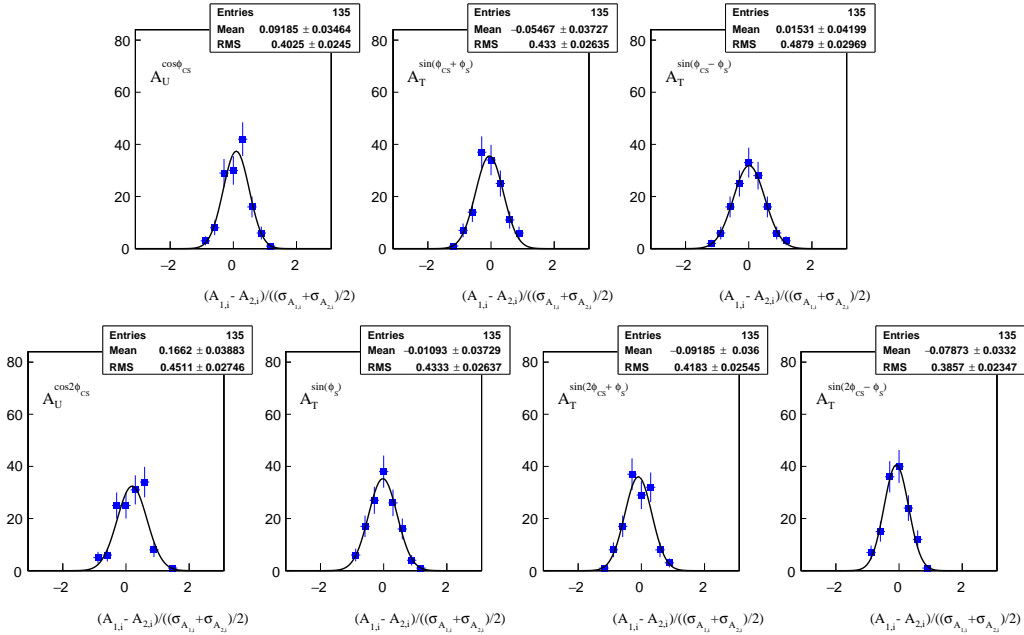
Figure 5.25: Psuedo pull distributions for the test of the tight target cut.
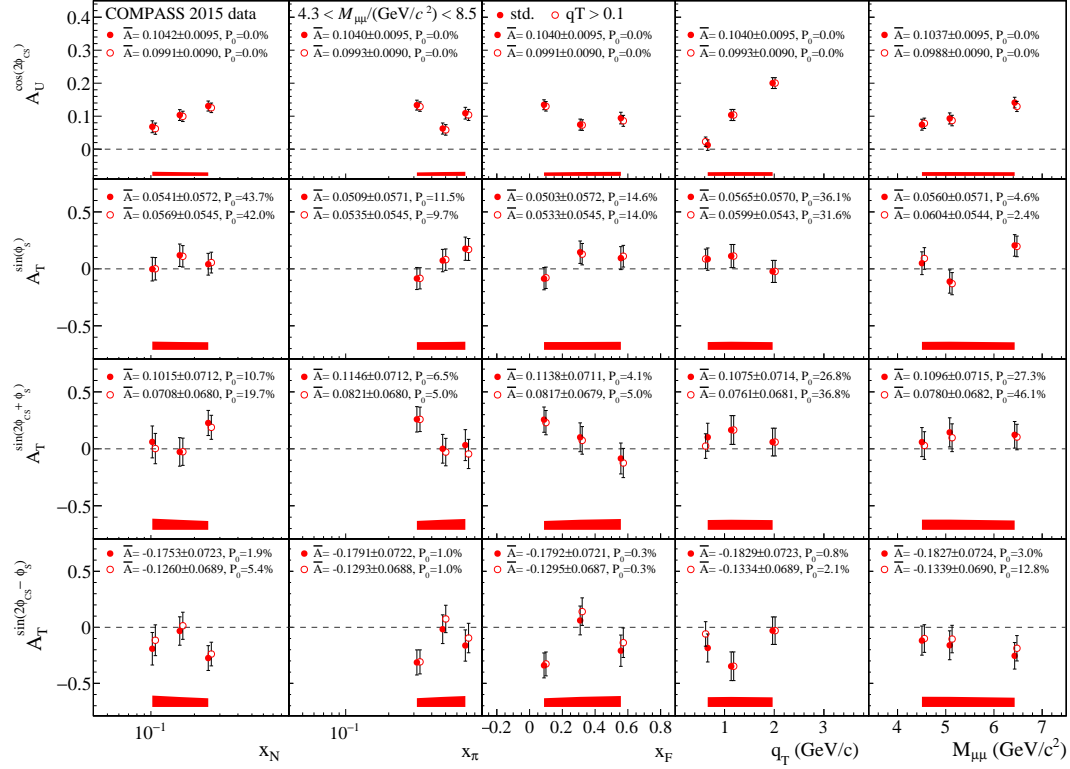
Figure 5.26: Comparison of asymmetries with the standard q_T cut or the relaxed q_T cut. The filled and open dots indicate the asymmetries with and without the relaxed q_T cut, respectively.
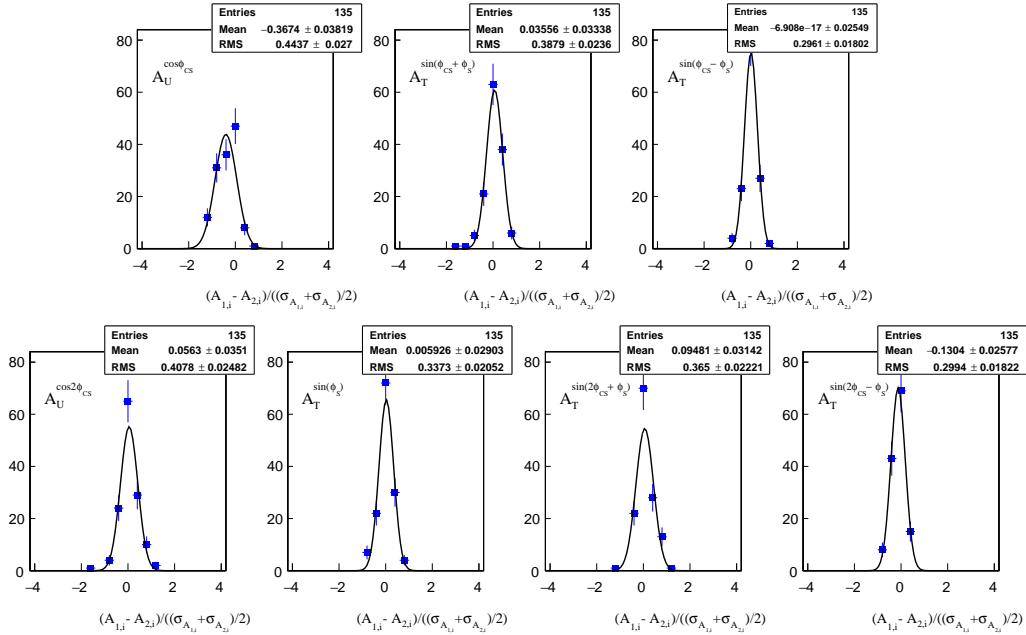
Figure 5.27: Psuedo pull distributions for the test of the loose q_T cuts.
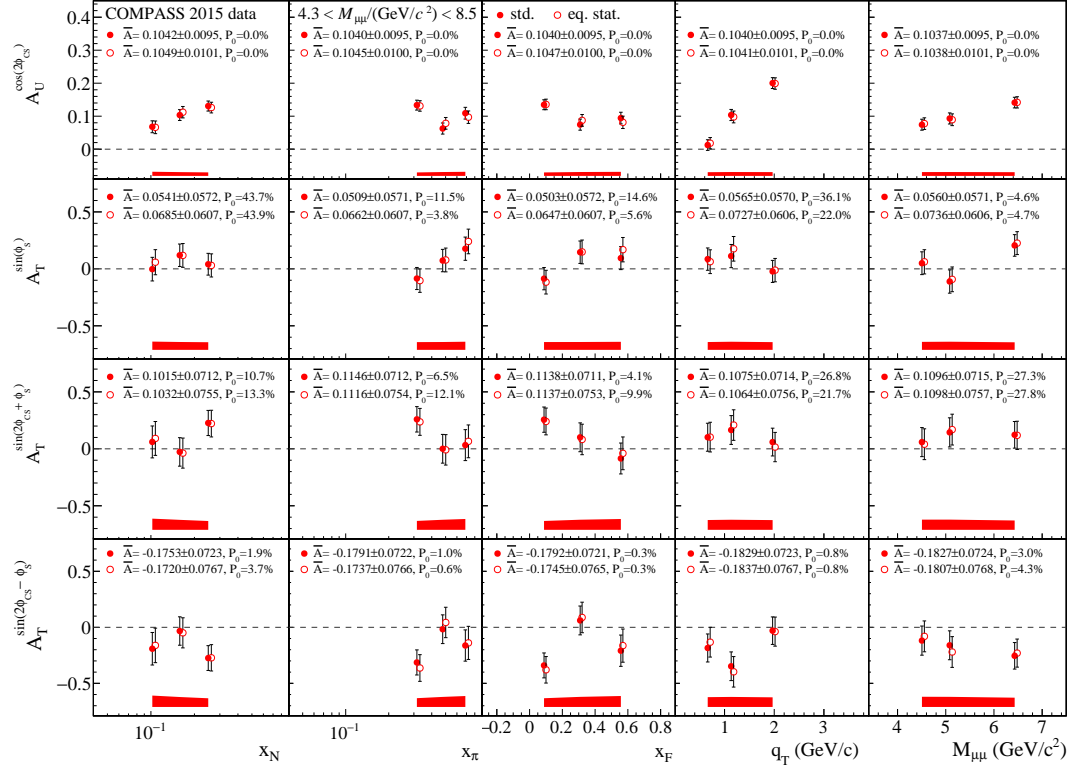
Figure 5.28: Comparison of asymmetries extracted with all data and with statistically balanced periods. The filled and open dots indicate the asymmetries from all data and from the balanced data, respectively.
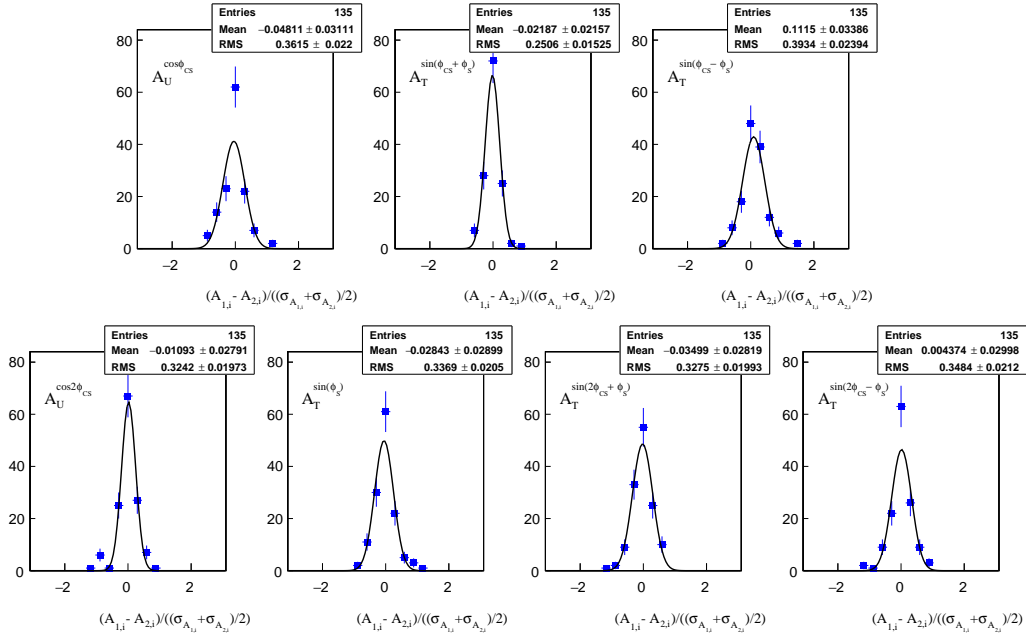
Figure 5.29: Pull distributions for the test of the balanced statistics.
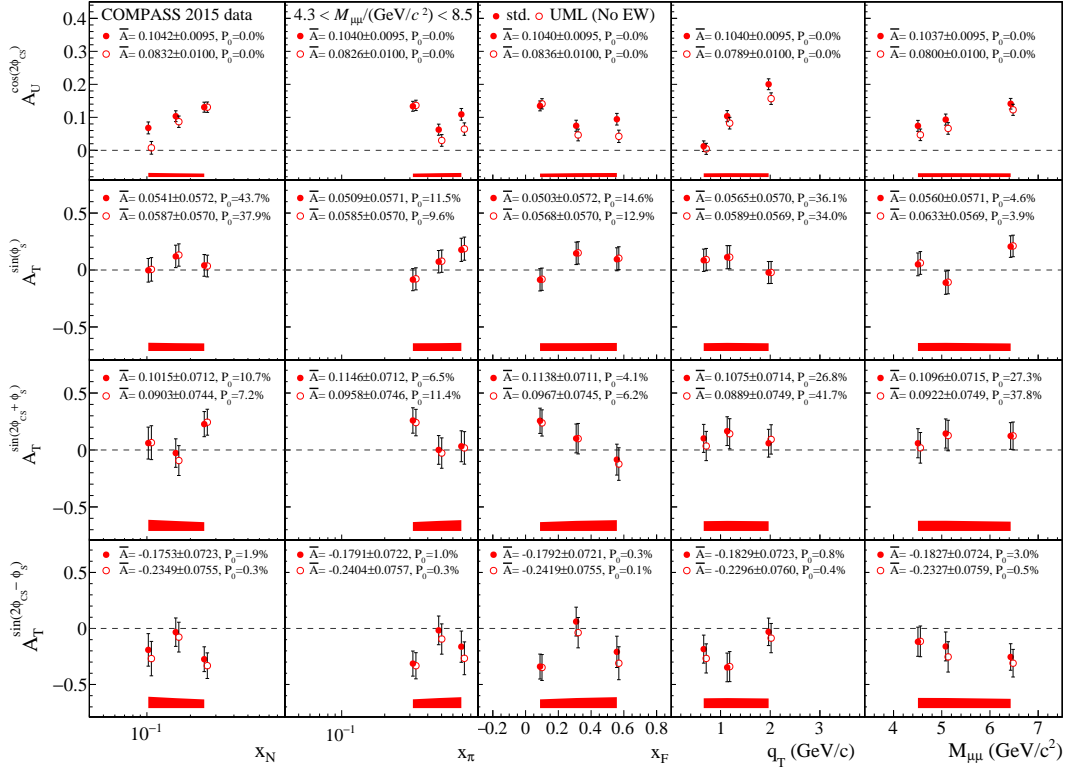
Figure 5.30: Comparison of extraction methods between the WE-UML method and the UML method. Filled and open dots show asymmetries the WE-UML and UML, respectively.

5.11.6 Comparison to an UML method

Comparisons to asymmetries obtained with a Unbinned Maximum Likelihood (UML) method are performed as Fig. 5.30 shows. In the asymmetry extractions with the UML, the dilution factor and the depolarisation factor are calculated bin by bin and correction of them are applied after fitting while these factors are calculated event by event in the extraction with WE-UML. Differences of the $A_T^{\sin\phi_S}$ are the smallest since the term of $A_T^{\sin\phi_S}$ does not include the correction of the depolarisation factor. For the other asymmetries $A_T^{\sin(2\phi_{CS}+\phi_S)}$ and $A_T^{\sin(2\phi_{CS}-\phi_S)}$, statistical errors with WE-UML is less than those with UML by 4 % to 5 %. $A_T^{\sin(2\phi_{CS}+\phi_S)}$ and $A_T^{\sin(2\phi_{CS}-\phi_S)}$ with UML are shifted by about 0.6 in standard deviation. The shift for the $A_T^{\sin(2\phi_{CS}+\phi_S)}$ is understood by different treatment of higher twist terms in the fit. A value of the depolarisation factor in the fit with UML is about 0.02 while a range of the factor in the fit with WE-UML is ±0.7. In the WE-UML case, the higher twist asymmetries gave different impacts from the twist-2 asymmetries at the level of a covariance matrix. The differences between two methods are not taken in the evaluation of the systematic uncertainties.

5.11.7 Comparison of the top-bottom or the left-right segments (TBLR test)

Since the COMPASS spectrometer is not symmetric geometrically for the virtual photon from the DY process, it is possible that a false asymmetry is introduced. For the investigation, two comparisons are performed: between top and bottom segments, and between left and right segments of the spectrometer. The segments are defined by an azimuthal angle of the μ^- in

Table 5.10: Systematic uncertainties in units of $\sigma_{sys}/\sigma_{stat}$ estimated from the TBLR test.

Segment	$A_T^{\sin\phi_{\mathrm{S}}}$	$A_T^{\sin(\phi_{\mathrm{CS}}+\phi_{\mathrm{S}})}$	$A_T^{\sin(\phi_{\mathrm{CS}}-\phi_{\mathrm{S}})}$	$A_T^{\sin(2\phi_{\mathrm{CS}}+\phi_{\mathrm{S}})}$	$A_T^{\sin(2\phi_{\mathrm{CS}}-\phi_{\mathrm{S}})}$
T-B	0.79	0.63	0.67	0.56	0.57
R-L	0.49	0.59	0.51	0.49	0.58
TBLR	0.6	0.6	0.6	0.5	0.6

the laboratory frame. If no false asymmetry is introduced, asymmetry extracted from top-bottom and left-right should be the same. Fig. 5.31 shows asymmetries extracted from each segment, and asymmetry differences between top-bottom or left right are shown in Fig. 5.32. Since azimuthal angles of μ^+ and μ^- are strongly correlated, a choice of μ^+ or μ^- does not give a difference. For the three TSAs, asymmetry differences are zero or compatible to zero within their statistical uncertainties. In the case of $A_U^{\cos 2\phi_{\mathrm{CS}}}$, asymmetries from the left and right segments show different values. This difference suggests that an acceptance as a function of ϕ_{CS} is not uniform, hence a bias on the $A_U^{\cos 2\phi_{\mathrm{CS}}}$ can exist. The unpolarised asymmetry should be extracted from the dedicated analysis using Eq. (2.12).

To estimate the systematic errors, the absolute value of the difference $A_{L-R} \equiv |A_L - A_R|/\sqrt{\sigma_L^2 + \sigma_R^2}$ and $A_{T-B} \equiv |A_T - A_B|/\sqrt{\sigma_T^2 + \sigma_B^2}$ are calculated and normarised to the statistical error. The differences are subtracted by The statistically expected value ~ 0.68 is subtracted from the differences in quadrature as $\sqrt{A^2 - 0.68^2}$ for each period and kinematics bin separately. The systematic error has been calculated for both tests, T-B and L-R, as a statistically weighted mean over the nine periods and kinematic bins separately for the different segments of the spectrometer and the each of the TSAs. Since the final asymmetries are built on overall sample and not the segmented one, as estimate for the overall "TBLR" systematic error, the average of "T-B" and "L-R" is taken. The systematic errors in units of the statistical uncertainties are summarised in Table 5.10.

5.11.8   False asymmetry

To estimate systematic uncertainties, asymmetry extractions from some fake-datasets which are made artificially to cancel asymmetries are performed with the UML estimators in order to treat low statistical samples. The asymmetries extracted from the fake-datasets are called false asymmetries, and non-zero value of the false asymmetry characterise systematic uncertainty. Several types of the fake-dataset are made as follows:

1. Sign of polarisation is flipped for one of the cells.

2. Both cells are divided into two fake sub-cells. Polarisation of a sub-cell is reversed with respect to the other sub-cell. A pair of the fake sub-cells from the same cell is assigned as a fake-sub-period. The asymmetries are extracted for each of the fake-sub-period configurations. The asymmetries are expected to be zero since the physics cancels out. Possible non-zero effects can be attributed to acceptance variations per cell.

3. Data of each given period are randomised into two fake-sub-periods by assigning even or odd serial number of the runs to the one sub-period and the other. The asymmetry extraction is performed from the two fake-sub-periods in the same way as the normal data.

4. Several other types are defined, and the results are found to be correlated to the above ones.
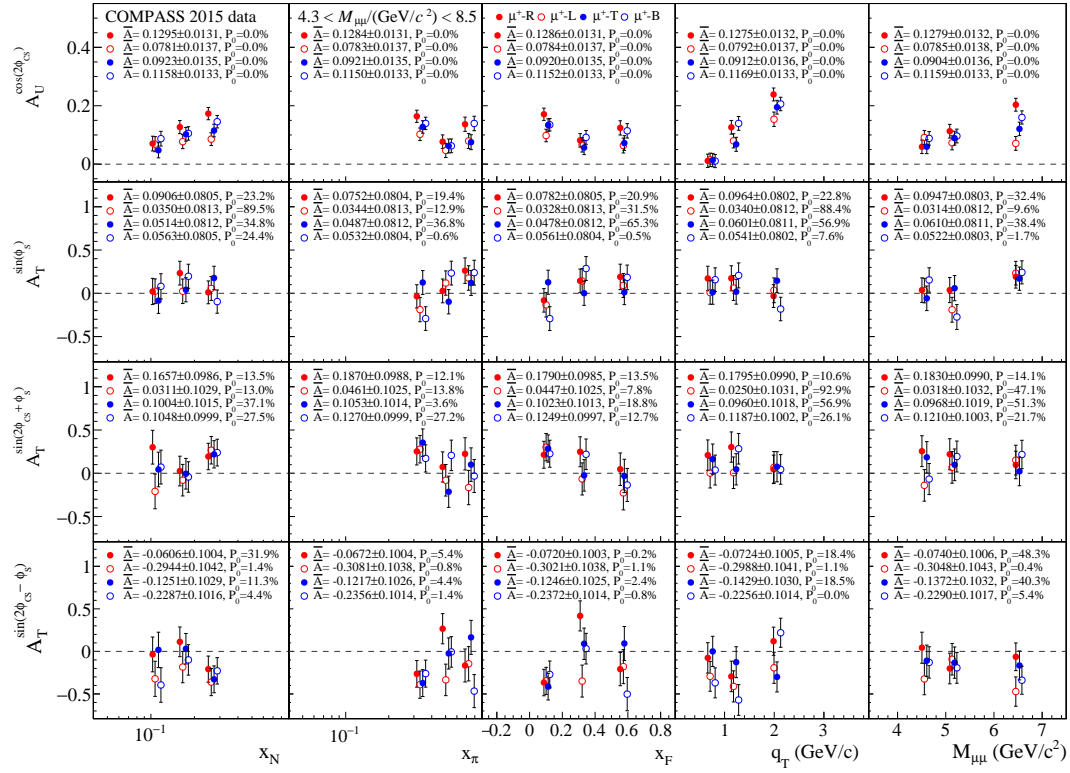
Figure 5.31: Asymmetries at the leading-twist extracted from each segment. The filled and open red points correspond to asymmetry whose μ^+ is in the right and the left segments, respectively. The filled and open blue points correspond to the same as the red points for the top and the bottom segments, respectively.
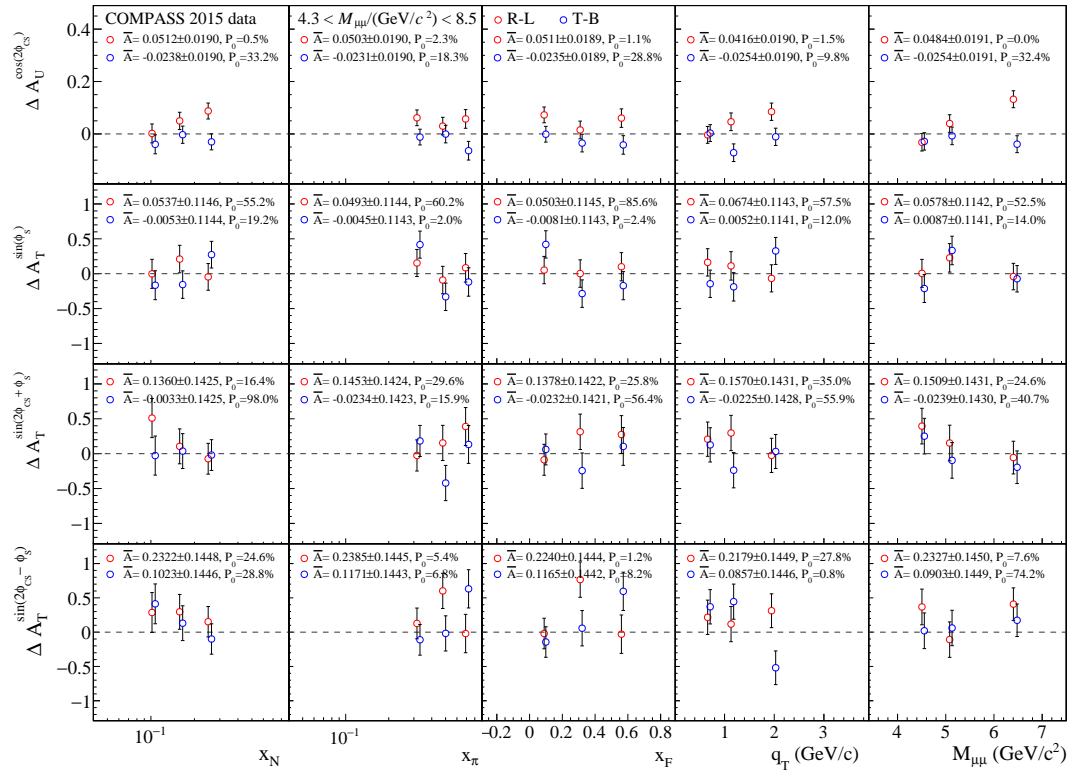
Figure 5.32: Asymmetry differences of top-bottom or left-right segments. The dashed lines indicate zero difference.

Fig. 5.33 shows results of the extraction from the first type. The systematic uncertainties are estimated from the asymmetry extractions from the fake-dataset. The systematic uncertainty for all TSAs are found to be 0.6 at maximum in units of the statistical uncertainty.

The systematic uncertainties estimated in Sec. 5.11.7 are found to be 0.5 to 0.6 in units of the statistical uncertainties (σ_{stat}), and the ones from the false asymmetries are $0.6\,\sigma_{\text{stat}}$. Since correlations are found between them, treating them equally can introduce a double-counting. Therefore the largest estimation of the two is used. All uncorrelated uncertainties that are estimated in the above systematic studies are taken into account for the evaluation of the final systematic uncertainty of the asymmetry. It includes the additive systematic errors of $0.6\,\sigma_{\text{stat}}$ from the TBLR and the false asymmetry tests and $0.4\,\sigma_{\text{stat}}$ from other tests. Therefore the systematic uncertainty of $0.7\,\sigma_{\text{stat}}$ is given from the quadrature.
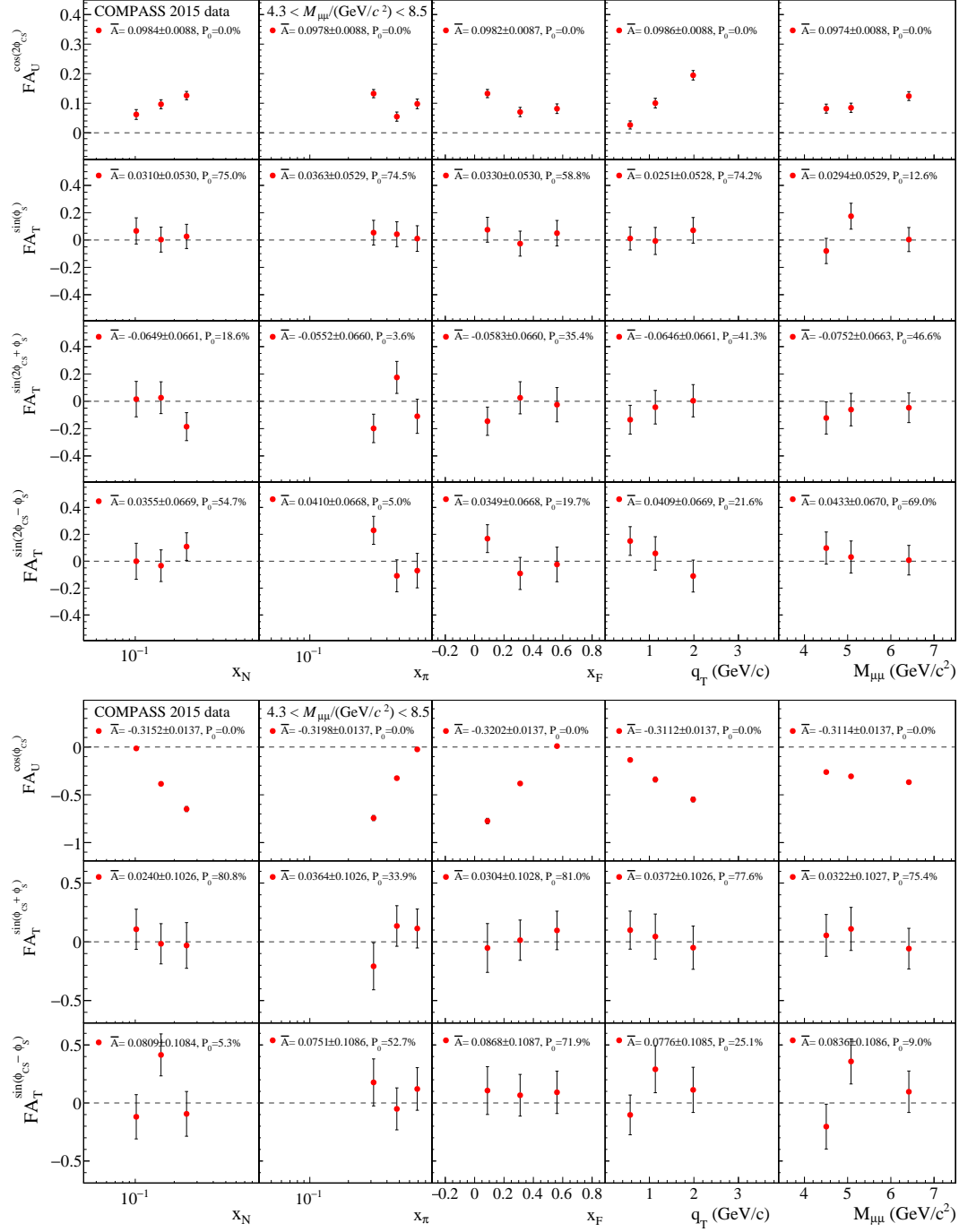
Figure 5.33: The false asymmetries extracted from 1 in Sec. 5.11.8. The asymmetries $A_U^{\cos\phi_{CS}}$ and $A_U^{\cos 2\phi_{CS}}$ are not affected by forming the fake-dataset since they are independent from polarisation of the target.

Results

The asymmetries defined in Eq. (2.15) were extracted as introduced in Sec. 5.9 in each kinematic bin of x_N, x_π, x_F, q_T and $M_{\mu\mu}$ (Fig. 5.16). The asymmetries integrated over all kinematic variables are shown in Fig. 5.17. The black bars correspond to statistical uncertainty. Systematic uncertainties shown as the red bars in the plots are about 0.7 times the statistical uncertainties as discussed in Sec. 5.11.8. Since a correction of the azimuthal acceptance is not applied, asymmetries independent from the target polarisation cannot be treated as physics results. Because of a large uncertainty, no clear trend is found in Fig. 5.16.

In the Fig. 5.17, the average of $A_T^{\sin\phi_S}$ which is related to the Sivers distribution of a nucleon and the number density of a pion is above zero at approximately one standard deviation of the total uncertainty. Fig. 6.1 shows a comparison of the averaged $A_T^{\sin\phi_S}$ to theoretical predictions based on different Q^2 evolution approaches. The red point and its error bar represent the average of $A_T^{\sin\phi_S}$ and its total uncertainty. The theoretical predictions are shown with The bands with darker colour shows the theoretical predictions. The labels "DGLAP", "TMD-1", and "TMD-2" correspond to [44], [43], and [42]. A positive sign of the asymmetry in the predictions are obtained with the sign reversal assumption, their values are extracted from SIDIS measurements. In the case of no sign change, bands with lighter colour are given. The obtained asymmetry is compatible with the sign reversal prediction although a determination of the value is difficult due to large uncertainty.

The average of $A_T^{\sin(2\phi_{CS}-\phi_S)}$ is measured to be below zero with a significance of about two standard deviations. The result agrees the model calculations performed in [117]. The result can be used to study the universality of the transversity distribution of a nucleon. The average of $A_T^{\sin(2\phi_{CS}+\phi_S)}$ which is related to the pretzelosity of a nucleon and the Boer-Mulders distribution of a pion is found to be above zero with a significance of approximately one standard deviation.
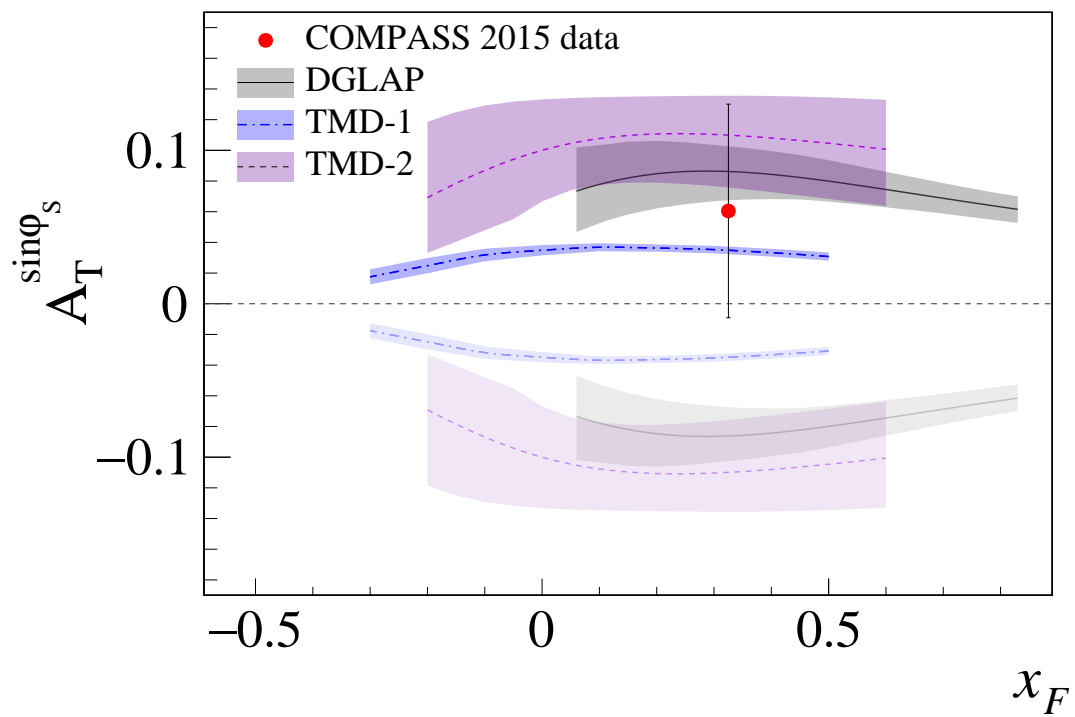
Figure 6.1: $A_T^{\sin \phi_S}$ with statistical and systematic uncertainty. A red dot shows $A_T^{\sin \phi_S}$ value and its error bar includes both the statistical and systematic uncertinties. Three bands are theoretical predictions for different Q^2 evolution schemes.

Chapter 7

Conclusion

Eight PDFs describe the nucleon structure entirely at the leading-twist. The pion-induced polarised DY process enables us to extract the Sivers, the Boer-Mulders, the Transversity, the Pretzelosity distributions of a nucleon. Although a confirmation of the sign change prediction for the Sivers and the Boer-Mulders distributions obtained via SIDIS and DY is a crucial test of the TMD approach based on QCD to the nucleon structure, a measurement via the DY process had not been performed due to technical difficulties.

The COMPASS collaboration performed the pion-induced polarised DY experiment for a study of the TMD-PDFs with a negatively charged hadron beam provided by CERN SPS with a momentum of $190\,\mathrm{GeV}/c$ and a transversely polarised proton target by polarising protons in solid ammonia. Since a high occupancy of detectors because of a large number of secondary particles as a result of a high-intensity hadron beam was the most serious issue for the measurement, the hadron absorber introduced in Sec. 3.3 was newly installed.

Solid ammonia contained in the two target cells with $55\,\mathrm{cm}$ long and $4\,\mathrm{cm}$ in diameter were longitudinally aligned on the beamline with a separation of $20\,\mathrm{cm}$. Protons in solid ammonia were polarised by DNP technique in $2.5\,\mathrm{T}$ solenoid magnetic field with a microwave of about $70\,\mathrm{GHz}$. The cells are polarised in different directions at the same time to measure the DY process with both polarities of targets at the same time. Polarisation reached about $80\,\%$ after $24\,\mathrm{h}$ polarisation build-up. Transverse polarisation was obtained by rotating magnetic field with the solenoid and the dipole magnets. The PT system was operated in the frozen spin mode with $0.6\,\mathrm{T}$ dipole magnetic field during physics data taking. The relaxation time of the upstream and the downstream cells were about $1000\,\mathrm{h}$. The downstream cell tended to give shorter relaxation time than the upstream cell due to effect by the beam. Final polarisation was determined as the Zig-Zag function and averaged value over a period was used for the physics analysis. On average, polarisation was about $73\,\%$ during the data taking.

The data taking was performed in 2015 for about six months. The stability checks were performed by monitoring the parameters listed in Tables 5.2 and 5.3 to find "bad" spills and runs. DY candidates were selected by applying the selection criteria defined in Sec. 5.3. MC simulation revealed that the DY process is dominant in the dimuon mass range from $4.3\,\mathrm{GeV}/c^2$ to $8.5\,\mathrm{GeV}/c^2$. The asymmetry extractions were performed with the WE-UML method introduced in Sec. 5.9. The asymmetries defined in Eq. (2.15) are extracted from the dimuon events with the dimuon mass range from $4.3\,\mathrm{GeV}/c^2$ to $8.5\,\mathrm{GeV}/c^2$ in each kinematic bin of x_N, x_π, x_F, q_T and $M_{\mu\mu}$. The asymmetries integrated over all kinematic variables are also calculated. The average of $A_T^{\sin\phi_S}$ was found to be above zero at approximately one standard deviation of the total uncertainty and was compatible with the sign reversal predictions [42–44]. The average of $A_T^{\sin(2\phi_{CS}-\phi_S)}$ was to be below zero with a significance of about two standard deviations and agreed the model calculations performed in [117]. The average of $A_T^{\sin(2\phi_{CS}+\phi_S)}$ was measured found to be above zero with a significance of approximately one standard deviation.

Bibliography

[1] John Collins. *Foundations of Perturbative QCD*. Cambridge Monographs on Particle Physics, Nuclear Physics and Cosmology. Cambridge University Press, 2011. doi: `10.1017/CBO9780511975592` (cit. on p. 1).

[2] David J. Gross and Frank Wilczek. "Ultraviolet Behavior of Non-Abelian Gauge Theories". In: *Phys. Rev. Lett.* 30 (26 1973), pp. 1343–1346. doi: `10.1103/PhysRevLett.30.1343`. url: `https://link.aps.org/doi/10.1103/PhysRevLett.30.1343` (cit. on p. 1).

[3] H. David Politzer. "Reliable Perturbative Results for Strong Interactions?" In: *Phys. Rev. Lett.* 30 (26 1973), pp. 1346–1349. doi: `10.1103/PhysRevLett.30.1346`. url: `https://link.aps.org/doi/10.1103/PhysRevLett.30.1346` (cit. on p. 1).

[4] J. D. Bjorken and E. A. Paschos. "Inelastic Electron-Proton and γ-Proton Scattering and the Structure of the Nucleon". In: *Phys. Rev.* 185 (5 1969), pp. 1975–1982. doi: `10.1103/PhysRev.185.1975`. url: `https://link.aps.org/doi/10.1103/PhysRev.185.1975` (cit. on p. 2).

[5] Richard P. Feynman. "The Behavior of Hadron Collisions at Extreme Energies". In: *High Energy Collisions: Third International Conference*. 1969. isbn: 978-0-677-13950-0 (cit. on p. 2).

[6] M. Breidenbach et al. "Observed Behavior of Highly Inelastic Electron-Proton Scattering". In: *Phys. Rev. Lett.* 23 (16 1969), pp. 935–939. doi: `10.1103/PhysRevLett.23.935`. url: `https://link.aps.org/doi/10.1103/PhysRevLett.23.935` (cit. on p. 3).

[7] J. D. Bjorken. "Asymptotic Sum Rules at Infinite Momentum". In: *Phys. Rev.* 179 (5 1969), pp. 1547–1553. doi: `10.1103/PhysRev.179.1547`. url: `https://link.aps.org/doi/10.1103/PhysRev.179.1547` (cit. on p. 3).

[8] C. G. Callan and David J. Gross. "High-Energy Electroproduction and the Constitution of the Electric Current". In: *Phys. Rev. Lett.* 22 (4 1969), pp. 156–159. doi: `10.1103/PhysRevLett.22.156`. url: `https://link.aps.org/doi/10.1103/PhysRevLett.22.156` (cit. on p. 3).

[9] V. N. Gribov and L. N. Lipatov. "Deep inelastic e p scattering in perturbation theory". In: *Sov. J. Nucl. Phys.* 15 (1972). [Yad. Fiz.15,781(1972)], pp. 438–450 (cit. on p. 3).

[10] G. Altarelli and G. Parisi. "Asymptotic freedom in parton language". In: *Nuclear Physics B* 126.2 (1977), pp. 298 –318. issn: 0550-3213. doi: `10.1016/0550-3213(77)90384-4`. url: `http://www.sciencedirect.com/science/article/pii/0550321377903844` (cit. on p. 3).

[11] Yuri L. Dokshitzer. "Calculation of the Structure Functions for Deep Inelastic Scattering and e+ e- Annihilation by Perturbation Theory in Quantum Chromodynamics." In: *Sov. Phys. JETP* 46 (1977). [Zh. Eksp. Teor. Fiz.73,1216(1977)], pp. 641–653 (cit. on p. 3).

[12] Guido Altarelli. "Partons in quantum chromodynamics". In: *Physics Reports* 81.1 (1982), pp. 1 –129. issn: 0370-1573. doi: 10.1016/0370-1573(82)90127-2. url: http://www.sciencedirect.com/science/article/pii/0370157382901272 (cit. on p. 3).

[13] C. Patrignani and Particle Data Group. "Review of Particle Physics". In: *Chinese Physics C* 40.10 (2016), p. 100001. url: http://stacks.iop.org/1674-1137/40/i=10/a=100001 (cit. on p. 4).

[14] A. D. Martin et al. "Parton distributions for the LHC". In: *The European Physical Journal C* 63.2 (2009), pp. 189–285. issn: 1434-6052. doi: 10.1140/epjc/s10052-009-1072-5. url: https://doi.org/10.1140/epjc/s10052-009-1072-5 (cit. on p. 5).

[15] R.L. Jaffe and Aneesh Manohar. "The g1 problem: Deep inelastic electron scattering and the spin of the proton". In: *Nuclear Physics B* 337.3 (1990), pp. 509 –546. issn: 0550-3213. doi: 10.1016/0550-3213(90)90506-9. url: http://www.sciencedirect.com/science/article/pii/0550321390905069 (cit. on p. 4).

[16] D. Boer and P. J. Mulders. "Time-reversal odd distribution functions in leptoproduction". In: *Phys. Rev. D* 57 (9 1998), pp. 5780–5786. doi: 10.1103/PhysRevD.57.5780. url: http://link.aps.org/doi/10.1103/PhysRevD.57.5780 (cit. on pp. 5, 10).

[17] M. J. Alguard *et al.* "Deep Inelastic Scattering of Polarized Electrons by Polarized Protons". In: *Physical Review Letters* 37.19 (Nov. 1976), pp. 1261–1265. issn: 0031-9007. doi: 10.1103/PhysRevLett.37.1261. url: http://link.aps.org/doi/10.1103/PhysRevLett.37.1261 (cit. on p. 6).

[18] G. Baum *et al.* "New Measurement of Deep-Inelastic e-p Asymmetries". In: *Physical Review Letters* 51.13 (Sept. 1983), pp. 1135–1138. issn: 0031-9007. doi: 10.1103/PhysRevLett.51.1135. url: http://link.aps.org/doi/10.1103/PhysRevLett.51.1135 (cit. on p. 6).

[19] J. Ashman *et al.* "A measurement of the spin asymmetry and determination of the structure function g1 in deep inelastic muon-proton scattering". In: *Physics Letters B* 206.2 (1988), pp. 364–370. issn: 0370-2693. doi: 10.1016/0370-2693(88)91523-7. url: http://www.sciencedirect.com/science/article/pii/0370269388915237 (cit. on p. 6).

[20] E. Leader and M. Anselmino. "A crisis in the parton model: where, oh where is the proton's spin?" In: *Zeitschrift für Physik C Particles and Fields* 41.2 (1988), pp. 239–246. issn: 1431-5858. doi: 10.1007/BF01566922. url: https://doi.org/10.1007/BF01566922 (cit. on p. 6).

[21] B. Adeva *et al.* "Polarisation of valence and non-strange sea quarks in the nucleon from semi-inclusive spin asymmetries". In: *Physics Letters B* 369.1 (1996), pp. 93 –100. issn: 0370-2693. doi: 10.1016/0370-2693(95)01584-1. url: http://www.sciencedirect.com/science/article/pii/0370269395015841 (cit. on p. 6).

[22] B. Adeva *et al.* "Polarised quark distributions in the nucleon from semi-inclusive spin asymmetries". In: *Physics Letters B* 420.1 (1998), pp. 180 –190. issn: 0370-2693. doi: 10.1016/S0370-2693(97)01546-3. url: http://www.sciencedirect.com/science/article/pii/S0370269397015463 (cit. on p. 6).

[23] A. Airapetian *et al.* "Precise determination of the spin structure function g_1 of the proton, deuteron, and neutron". In: *Phys. Rev. D* 75 (1 2007), p. 012007. doi: 10.1103/PhysRevD.75.012007. url: https://link.aps.org/doi/10.1103/PhysRevD.75.012007 (cit. on p. 6).

[24] A. Airapetian *et al.* "Measurement of parton distributions of strange quarks in the nucleon from charged-kaon production in deep-inelastic scattering on the deuteron". In: *Physics Letters B* 666.5 (2008), pp. 446 –450. issn: 0370-2693. doi: `10.1016/j.physletb.2008.07.090`. url: `http://www.sciencedirect.com/science/article/pii/S0370269308009386` (cit. on p. 6).

[25] V.Yu. Alexakhin *et al.* "The deuteron spin-dependent structure function g1d and its first moment". In: *Physics Letters B* 647.1 (2007), pp. 8 –17. issn: 0370-2693. doi: `10.1016/j.physletb.2006.12.076`. url: `http://www.sciencedirect.com/science/article/pii/S037026930700113X` (cit. on p. 6).

[26] M.G. Alekseev *et al.* "The spin-dependent structure function of the proton g1p and a test of the Bjorken sum rule". In: *Physics Letters B* 690.5 (2010), pp. 466 –472. issn: 0370-2693. doi: `10.1016/j.physletb.2010.05.069`. url: `http://www.sciencedirect.com/science/article/pii/S0370269310006726` (cit. on p. 6).

[27] M.G. Alekseev *et al.* "Quark helicity distributions from longitudinal spin asymmetries in muon-proton and muon-deuteron scattering". In: *Physics Letters B* 693.3 (2010), pp. 227 –235. issn: 0370-2693. doi: `10.1016/j.physletb.2010.08.034`. url: `http://www.sciencedirect.com/science/article/pii/S0370269310009810` (cit. on p. 6).

[28] X. Zheng *et al.* "Precision Measurement of the Neutron Spin Asymmetry A_1^n and Spin-Flavor Decomposition in the Valence Quark Region". In: *Phys. Rev. Lett.* 92 (1 2004), p. 012004. doi: `10.1103/PhysRevLett.92.012004`. url: `https://link.aps.org/doi/10.1103/PhysRevLett.92.012004` (cit. on p. 6).

[29] K.V. Dharmawardane *et al.* "Measurement of the x- and Q2-dependence of the asymmetry A1 on the nucleon". In: *Physics Letters B* 641.1 (2006), pp. 11 –17. issn: 0370-2693. doi: `10.1016/j.physletb.2006.08.011`. url: `http://www.sciencedirect.com/science/article/pii/S0370269306009890` (cit. on p. 6).

[30] F. Taghavi-Shahri et al. "Next-to-next-to-leading order QCD analysis of spin-dependent parton distribution functions and their uncertainties: Jacobi polynomials approach". In: *Phys. Rev. D* 93 (11 2016), p. 114024. doi: `10.1103/PhysRevD.93.114024`. url: `https://link.aps.org/doi/10.1103/PhysRevD.93.114024` (cit. on p. 6).

[31] John P. Ralston and Davidson E. Soper. "Production of dimuons from high-energy polarized proton-proton collisions". In: *Nuclear Physics B* 152.1 (1979), pp. 109 –124. issn: 0550-3213. doi: `10.1016/0550-3213(79)90082-8`. url: `http://www.sciencedirect.com/science/article/pii/0550321379900828` (cit. on p. 7).

[32] Alessandro Bacchetta, A. Courtoy, and Marco Radici. "First extraction of valence transversities in a collinear framework". In: *Journal of High Energy Physics* 2013.3 (2013), p. 119. issn: 1029-8479. doi: `10.1007/JHEP03(2013)119`. url: `https://doi.org/10.1007/JHEP03(2013)119` (cit. on p. 7).

[33] Dennis Sivers. "Single-spin production asymmetries from the hard scattering of point-like constituents". In: *Phys. Rev. D* 41 (1 1990), pp. 83–90. doi: `10.1103/PhysRevD.41.83`. url: `http://link.aps.org/doi/10.1103/PhysRevD.41.83` (cit. on p. 8).

[34] R. D. Klem *et al.* "Measurement of Asymmetries of Inclusive Pion Production in Proton-Proton Interactions at 6 and 11.8 GeV/c". In: *Phys. Rev. Lett.* 36 (16 1976), pp. 929–931. doi: `10.1103/PhysRevLett.36.929`. url: `https://link.aps.org/doi/10.1103/PhysRevLett.36.929` (cit. on p. 8).

[35] W. H. Dragoset *et al.* "Asymmetries in inclusive proton-nucleon scattering at 11.75 GeV/c". In: *Phys. Rev. D* 18 (11 1978), pp. 3939–3954. doi: `10.1103/PhysRevD.18.3939`. url: `https://link.aps.org/doi/10.1103/PhysRevD.18.3939` (cit. on p. 8).

[36] John Collins. "Fragmentation of transversely polarized quarks probed in transverse momentum distributions". In: *Nuclear Physics B* 396.1 (1993), pp. 161 –182. issn: 0550-3213. doi: `10.1016/0550-3213(93)90262-N`. url: `http://www.sciencedirect.com/science/article/pii/055032139390262N` (cit. on p. 9).

[37] John C. Collins. "Leading-twist single-transverse-spin asymmetries: Drell-Yan and deep-inelastic scattering". In: *Phys. Lett. B* 536.1-2 (2002), pp. 43 –48. issn: 0370-2693. doi: `http://dx.doi.org/10.1016/S0370-2693(02)01819-1`. url: `http://www.sciencedirect.com/science/article/pii/S0370269302018191` (cit. on p. 9).

[38] C. Adolph *et al.* "Collins and Sivers asymmetries in muonproduction of pions and kaons off transversely polarised protons". In: *Physics Letters B* 744.Supplement C (2015), pp. 250 –259. issn: 0370-2693. doi: `10.1016/j.physletb.2015.03.056`. url: `http://www.sciencedirect.com/science/article/pii/S0370269315002312` (cit. on p. 9).

[39] A. Airapetian *et al.* "Observation of the Naive-T-Odd Sivers Effect in Deep-Inelastic Scattering". In: *Phys. Rev. Lett.* 103 (15 2009), p. 152002. doi: `10.1103/PhysRevLett.103.152002`. url: `http://link.aps.org/doi/10.1103/PhysRevLett.103.152002` (cit. on p. 9).

[40] X. Qian *et al.* "Single Spin Asymmetries in Charged Pion Production from Semi-Inclusive Deep Inelastic Scattering on a Transversely Polarized ^{3}He Target at $Q^2 = 1.4 - 2.7\,\mathrm{GeV}^2$". In: *Phys. Rev. Lett.* 107 (7 2011), p. 072003. doi: `10.1103/PhysRevLett.107.072003`. url: `https://link.aps.org/doi/10.1103/PhysRevLett.107.072003` (cit. on p. 9).

[41] Zhong-Bo Kang and Alexei Prokudin. "Global fitting of single spin asymmetry: An attempt". In: *Phys. Rev. D* 85 (7 2012), p. 074008. doi: `10.1103/PhysRevD.85.074008`. url: `https://link.aps.org/doi/10.1103/PhysRevD.85.074008` (cit. on p. 9).

[42] Peng Sun and Feng Yuan. "Transverse momentum dependent evolution: Matching semi-inclusive deep inelastic scattering processes to Drell-Yan and W/Z boson production". In: *Phys. Rev. D* 88 (11 2013), p. 114012. doi: `10.1103/PhysRevD.88.114012`. url: `http://link.aps.org/doi/10.1103/PhysRevD.88.114012` (cit. on pp. 9, 97, 99).

[43] Miguel G. Echevarria et al. "QCD evolution of the Sivers asymmetry". In: *Phys. Rev. D* 89 (7 2014), p. 074013. doi: `10.1103/PhysRevD.89.074013`. url: `http://link.aps.org/doi/10.1103/PhysRevD.89.074013` (cit. on pp. 9, 97, 99).

[44] M. Anselmino et al. "Study of the sign change of the Sivers function from STAR collaboration W/Z production data". In: *Journal of High Energy Physics* 2017.4 (2017), p. 46. issn: 1029-8479. doi: `10.1007/JHEP04(2017)046`. url: `https://doi.org/10.1007/JHEP04(2017)046` (cit. on pp. 9, 10, 97, 99).

[45] D. Boer. *Boer-Mulders function*. `http://www.physics4all.nl/BoerMulders.html`. url: `http://www.physics4all.nl/BoerMulders.html` (visited on 12/2017–0017) (cit. on p. 10).

[46] Bing Zhang et al. "Extracting Boer-Mulders functions from $p + D$ Drell-Yan processes". In: *Phys. Rev. D* 77 (5 2008), p. 054011. doi: `10.1103/PhysRevD.77.054011`. url: `https://link.aps.org/doi/10.1103/PhysRevD.77.054011` (cit. on p. 10).

[47] Zhun Lu and Ivan Schmidt. "Updating Boer-Mulders functions from unpolarized *pd* and *pp* Drell-Yan data". In: *Phys. Rev. D* 81 (3 2010), p. 034023. doi: `10.1103/PhysRevD.81.034023`. url: `https://link.aps.org/doi/10.1103/PhysRevD.81.034023` (cit. on pp. 10, 11).

[48] L. Y. Zhu et al. "Measurement of Angular Distributions of Drell-Yan Dimuons in $p + d$ Interactions at 800 GeV/c". In: *Phys. Rev. Lett.* 99 (8 2007), p. 082301. doi: `10.1103/PhysRevLett.99.082301`. url: `https://link.aps.org/doi/10.1103/PhysRevLett.99.082301` (cit. on pp. 10, 14, 15).

[49] L. Y. Zhu et al. "Measurement of Angular Distributions of Drell-Yan Dimuons in $p + p$ Interactions at 800 GeV/c". In: *Phys. Rev. Lett.* 102 (18 2009), p. 182001. doi: `10.1103/PhysRevLett.102.182001`. url: `http://link.aps.org/doi/10.1103/PhysRevLett.102.182001` (cit. on pp. 10, 14, 15).

[50] Vincenzo Barone, Stefano Melis, and Alexei Prokudin. "Boer-Mulders effect in unpolarized SIDIS: An analysis of the COMPASS and HERMES data on the cos2ϕ asymmetry". In: *Phys. Rev. D* 81 (11 2010), p. 114026. doi: `10.1103/PhysRevD.81.114026`. url: `https://link.aps.org/doi/10.1103/PhysRevD.81.114026` (cit. on p. 11).

[51] Robert N. Cahn. "Critique of parton-model calculations of azimuthal dependence in leptoproduction". In: *Phys. Rev. D* 40 (9 1989), pp. 3107–3110. doi: `10.1103/PhysRevD.40.3107`. url: `https://link.aps.org/doi/10.1103/PhysRevD.40.3107` (cit. on p. 11).

[52] M. Anselmino et al. "Role of Cahn and Sivers effects in deep inelastic scattering". In: *Phys. Rev. D* 71 (7 2005), p. 074006. doi: `10.1103/PhysRevD.71.074006`. url: `https://link.aps.org/doi/10.1103/PhysRevD.71.074006` (cit. on p. 11).

[53] Sidney D. Drell and Tung-Mow Yan. "Massive Lepton-Pair Production in Hadron-Hadron Collisions at High Energies". In: *Phys. Rev. Lett.* 25 (5 1970), pp. 316–320. doi: `10.1103/PhysRevLett.25.316`. url: `http://link.aps.org/doi/10.1103/PhysRevLett.25.316` (cit. on p. 11).

[54] J. H. Christenson et al. "Observation of Massive Muon Pairs in Hadron Collisions". In: *Phys. Rev. Lett.* 25 (21 1970), pp. 1523–1526. doi: `10.1103/PhysRevLett.25.1523`. url: `http://link.aps.org/doi/10.1103/PhysRevLett.25.1523` (cit. on p. 11).

[55] John C. Collins and Davison E. Soper. "Angular distribution of dileptons in high-energy hadron collisions". In: *Phys. Rev. D* 16 (7 1977), pp. 2219–2225. doi: `10.1103/PhysRevD.16.2219`. url: `http://link.aps.org/doi/10.1103/PhysRevD.16.2219` (cit. on p. 11).

[56] C. S. Lam and Wu-Ki Tung. "Systematic approach to inclusive lepton pair production in hadronic collisions". In: *Phys. Rev. D* 18 (7 1978), pp. 2447–2461. doi: `10.1103/PhysRevD.18.2447`. url: `http://link.aps.org/doi/10.1103/PhysRevD.18.2447` (cit. on p. 13).

[57] Oleg Teryaev. "Positivity constraints for quarkonia polarization". In: *Nuclear Physics B - Proceedings Supplements* 214.1 (2011), pp. 118 –119. issn: 0920-5632. doi: `10.1016/j.nuclphysbps.2011.03.070`. url: `http://www.sciencedirect.com/science/article/pii/S0920563211001381` (cit. on p. 14).

[58] M. Guanziroli et al. "Angular distributions of muon pairs produced by negative pions on deuterium and tungsten". In: *Zeitschrift für Physik C Particles and Fields* 37.4 (1988), pp. 545–556. issn: 1431-5858. doi: `10.1007/BF01549713`. url: `http://dx.doi.org/10.1007/BF01549713` (cit. on pp. 14, 15).

[59] T. Aaltonen et al. "First Measurement of the Angular Coefficients of Drell-Yan e^+e^- Pairs in the Z Mass Region from $p\overline{p}$ Collisions at $\sqrt{s} = 1.96$ TeV". In: *Phys. Rev. Lett.* 106 (24 2011), p. 241801. doi: 10.1103/PhysRevLett.106.241801. url: https://link.aps.org/doi/10.1103/PhysRevLett.106.241801 (cit. on pp. 14, 15).

[60] V. Khachatryan *et al.* "Angular coefficients of Z bosons produced in pp collisions at and decaying to as a function of transverse momentum and rapidity". In: *Physics Letters B* 750 (2015), pp. 154 −175. issn: 0370-2693. doi: 10.1016/j.physletb.2015.08.061. url: http://www.sciencedirect.com/science/article/pii/S0370269315006620 (cit. on pp. 14, 15).

[61] G. Aad *et al.* "Measurement of the angular coefficients in Z-boson events using electron and muon pairs from data taken at $\sqrt{s} = 8$ TeV with the ATLAS detector". In: *Journal of High Energy Physics* 2016.8 (2016), p. 159. issn: 1029-8479. doi: 10.1007/JHEP08(2016)159. url: https://doi.org/10.1007/JHEP08(2016)159 (cit. on pp. 14, 15).

[62] Martin Lambertsen and Werner Vogelsang. "Drell-Yan lepton angular distributions in perturbative QCD". In: *Phys. Rev. D* 93 (11 2016), p. 114013. doi: 10.1103/PhysRevD.93.114013. url: https://link.aps.org/doi/10.1103/PhysRevD.93.114013 (cit. on p. 14).

[63] J. S. Conway et al. "Experimental study of muon pairs produced by 252-GeV pions on tungsten". In: *Phys. Rev. D* 39 (1 1989), pp. 92−122. doi: 10.1103/PhysRevD.39.92. url: http://link.aps.org/doi/10.1103/PhysRevD.39.92 (cit. on p. 15).

[64] L. Adamczyk et al. "Measurement of the Transverse Single-Spin Asymmetry in $p^\uparrow + p \rightarrow W^\pm/Z^0$ at RHIC". In: *Phys. Rev. Lett.* 116 (13 2016), p. 132301. doi: 10.1103/PhysRevLett.116.132301. url: http://link.aps.org/doi/10.1103/PhysRevLett.116.132301 (cit. on pp. 15, 17, 18).

[65] M. Aghasyan et al. "First Measurement of Transverse-Spin-Dependent Azimuthal Asymmetries in the Drell-Yan Process". In: *Phys. Rev. Lett.* 119 (11 2017), p. 112002. doi: 10.1103/PhysRevLett.119.112002. url: https://link.aps.org/doi/10.1103/PhysRevLett.119.112002 (cit. on p. 15).

[66] S. Arnold, A. Metz, and M. Schlegel. "Dilepton production from polarized hadron hadron collisions". In: *Phys. Rev. D* 79 (3 2009), p. 034005. doi: 10.1103/PhysRevD.79.034005. url: http://link.aps.org/doi/10.1103/PhysRevD.79.034005 (cit. on pp. 15, 16).

[67] F Gautheron et al. *COMPASS-II Proposal*. Tech. rep. CERN-SPSC-2010-014. SPSC-P-340. Geneva: CERN, 2010. url: https://cds.cern.ch/record/1265628 (cit. on pp. 19, 20).

[68] P. Abbon et al. "The COMPASS experiment at CERN". In: *Nuclear Instruments and Methods in Physics Research Section A: Accelerators, Spectrometers, Detectors and Associated Equipment* 577.3 (2007), pp. 455 −518. issn: 0168-9002. doi: http://dx.doi.org/10.1016/j.nima.2007.03.026. url: http://www.sciencedirect.com/science/article/pii/S0168900207005001 (cit. on pp. 19, 27−30, 32−35, 39).

[69] P. Abbon et al. "The COMPASS setup for physics with hadron beams". In: *Nuclear Instruments and Methods in Physics Research Section A: Accelerators, Spectrometers, Detectors and Associated Equipment* 779 (2015), pp. 69 −115. issn: 0168-9002. doi: http://dx.doi.org/10.1016/j.nima.2015.01.035. url: http://www.sciencedirect.com/science/article/pii/S0168900215000662 (cit. on pp. 19, 21, 24, 28, 30, 31, 34, 37).

[70]   Cinzia De Melis. "The CERN accelerator complex. Complexe des accélérateurs du CERN". In: (2016). General Photo. url: https://cds.cern.ch/record/2197559 (cit. on p. 23).

[71]   N. Doble et al. "The upgraded muon beam at the SPS". In: *Nuclear Instruments and Methods in Physics Research Section A: Accelerators, Spectrometers, Detectors and Associated Equipment* 343.2 (1994), pp. 351 –362. issn: 0168-9002. doi: https://doi.org/10.1016/0168-9002(94)90212-7. url: http://www.sciencedirect.com/science/article/pii/0168900294902127 (cit. on p. 23).

[72]   Claude Bovet et al. *The CEDAR counters for particle identification in the SPS secondary beams: a description and an operation manual*. CERN Yellow Reports: Monographs. Geneva: CERN, 1982. url: https://cds.cern.ch/record/142935 (cit. on p. 21).

[73]   K Kurek et al. "An algorithm for track reconstruction in the large angle spectrometer of the COMPASS experiment". In: *Nuclear Instruments and Methods in Physics Research Section A: Accelerators, Spectrometers, Detectors and Associated Equipment* 485.3 (2002), pp. 720 –738. issn: 0168-9002. doi: https://doi.org/10.1016/S0168-9002(01)02123-4. url: http://www.sciencedirect.com/science/article/pii/S0168900201021234 (cit. on p. 27).

[74]   D. Adams et al. "Spin structure of the proton from polarized inclusive deep-inelastic muon-proton scattering". In: *Phys. Rev. D* 56 (9 1997), pp. 5330–5358. doi: 10.1103/PhysRevD.56.5330. url: https://link.aps.org/doi/10.1103/PhysRevD.56.5330 (cit. on p. 27).

[75]   J Bisplinghoff et al. "A scintillating fibre hodoscope for high rate applications". In: *Nuclear Instruments and Methods in Physics Research Section A: Accelerators, Spectrometers, Detectors and Associated Equipment* 490.1 (2002), pp. 101 –111. issn: 0168-9002. doi: https://doi.org/10.1016/S0168-9002(02)01064-1. url: http://www.sciencedirect.com/science/article/pii/S0168900202010641 (cit. on p. 27).

[76]   S Horikawa et al. "Development of a scintillating-fibre detector with position-sensitive photomultipliers for high-rate experiments". In: *Nuclear Instruments and Methods in Physics Research Section A: Accelerators, Spectrometers, Detectors and Associated Equipment* 516.1 (2004), pp. 34 –49. issn: 0168-9002. doi: https://doi.org/10.1016/j.nima.2003.07.038. url: http://www.sciencedirect.com/science/article/pii/S0168900203024100 (cit. on p. 27).

[77]   V.N. Bychkov et al. "The large size straw drift chambers of the COMPASS experiment". In: *Nuclear Instruments and Methods in Physics Research Section A: Accelerators, Spectrometers, Detectors and Associated Equipment* 556.1 (2006), pp. 66 –79. issn: 0168-9002. doi: https://doi.org/10.1016/j.nima.2005.10.026. url: http://www.sciencedirect.com/science/article/pii/S0168900205019054 (cit. on pp. 30, 31).

[78]   D Thers et al. "Micromegas as a large microstrip detector for the COMPASS experiment". In: *Nuclear Instruments and Methods in Physics Research Section A: Accelerators, Spectrometers, Detectors and Associated Equipment* 469.2 (2001), pp. 133 –146. issn: 0168-9002. doi: https://doi.org/10.1016/S0168-9002(01)00769-0. url: http://www.sciencedirect.com/science/article/pii/S0168900201007690 (cit. on p. 32).

[79]   F. Kunn et al. "The gaseous microstrip detector micromegas for the COMPASS experiment at CERN". In: *Nuclear Physics A* 721.Supplement C (2003), pp. C1087 –C1090. issn: 0375-9474. doi: https://doi.org/10.1016/S0375-9474(03)01291-0. url:

http://www.sciencedirect.com/science/article/pii/S0375947403012910
(cit. on p. 32).

[80]   C. Bernet et al. "The 40 x 40cm2 gaseous microstrip detector Micromegas for the
        high-luminosity COMPASS experiment at CERN". In: *Nuclear Instruments and Meth-
        ods in Physics Research Section A: Accelerators, Spectrometers, Detectors and Associated Equipment*
        536.1 (2005), pp. 61 −69. issn: 0168-9002. doi: https://doi.org/10.1016/j.
        nima.2004.07.170. url: http://www.sciencedirect.com/science/article/
        pii/S0168900204017280 (cit. on p. 32).

[81]   F. Sauli. "GEM: A new concept for electron amplification in gas detectors". In: *Nuclear
        Instruments and Methods in Physics Research Section A: Accelerators, Spectrometers, Detectors and
        Associated Equipment* 386.2-3 (1997), pp. 531 −534. issn: 0168-9002. doi: http://dx.
        doi.org/10.1016/S0168-9002(96)01172-2. url: http://www.sciencedirect.
        com/science/article/pii/S0168900296011722 (cit. on p. 33).

[82]   Fabio Sauli. "The gas electron multiplier (GEM): Operating principles and applica-
        tions". In: *Nuclear Instruments and Methods in Physics Research Section A: Accelerators, Spec-
        trometers, Detectors and Associated Equipment* 805.Supplement C (2016). Special Issue in
        memory of Glenn F. Knoll, pp. 2 −24. issn: 0168-9002. doi: https://doi.org/10.
        1016/j.nima.2015.07.060. url: http://www.sciencedirect.com/science/
        article/pii/S0168900215008980 (cit. on p. 33).

[83]   Alexander Austregesilo et al. "First Results of the PixelGEM Central Tracking Sys-
        tem for COMPASS". In: *Nuclear Physics B - Proceedings Supplements* 197.1 (2009). 11th
        Topical Seminar on Innovative Particle and Radiation Detectors (IPRD08), pp. 113
        −116. issn: 0920-5632. doi: https://doi.org/10.1016/j.nuclphysbps.
        2009.10.046. url: http://www.sciencedirect.com/science/article/pii/
        S0920563209007671 (cit. on p. 34).

[84]   The muon trigger group. *Muon Trigger Documentation*. COMPASS, 2002. url: http://
        wwwcompass.cern.ch/compass/detector/trigger/muon-trigger/triggerdoc.
        pdf (cit. on p. 35).

[85]   C. Bernet et al. "The COMPASS trigger system for muon scattering". In: *Nuclear
        Instruments and Methods in Physics Research Section A: Accelerators, Spectrometers, Detectors and
        Associated Equipment* 550.1−2 (2005), pp. 217 −240. issn: 0168-9002. doi: http://dx.
        doi.org/10.1016/j.nima.2005.05.043. url: http://www.sciencedirect.com/
        science/article/pii/S0168900205012568 (cit. on pp. 35, 36).

[86]   *CORAL*. https://twiki.cern.ch/twiki/bin/view/Compass/DataReconstruction/
        CoralSoftware (cit. on p. 38).

[87]   R. Frühwirth. "Application of Kalman filtering to track and vertex fitting". In: *Nuclear
        Instruments and Methods in Physics Research Section A: Accelerators, Spectrometers, Detectors and
        Associated Equipment* 262.2 (1987), pp. 444 −450. issn: 0168-9002. doi: https://doi.
        org/10.1016/0168-9002(87)90887-4. url: http://www.sciencedirect.com/
        science/article/pii/0168900287908874 (cit. on p. 38).

[88]   *PHAST*. http://ges.web.cern.ch/ges/phast/ (cit. on p. 38).

[89]   C. D. Jeffries. "Polarization of Nuclei by Resonance Saturation in Paramagnetic Crys-
        tals". In: *Phys. Rev.* 106 (1 1957), pp. 164–165. doi: 10.1103/PhysRev.106.164. url:
        https://link.aps.org/doi/10.1103/PhysRev.106.164 (cit. on p. 41).

[90]   M. Abraham, R. W. Kedzie, and C. D. Jeffries. "γ-Ray Anisotropy of Co^{60} Nuclei Po-
        larized by Paramagnetic Resonance Saturation". In: *Phys. Rev.* 106 (1 1957), pp. 165–
        166. doi: 10.1103/PhysRev.106.165. url: https://link.aps.org/doi/10.1103/
        PhysRev.106.165 (cit. on p. 41).

[91]   C. D. Jeffries. "Dynamic Orientation of Nuclei by Forbidden Transitions in Para-
        magnetic Resonance". In: *Phys. Rev.* 117 (4 1960), pp. 1056–1069. doi: `10.1103/`
        `PhysRev.117.1056`. url: `https://link.aps.org/doi/10.1103/PhysRev.117.`
        `1056` (cit. on p. 41).

[92]   B. Adeva et al. "Measurement of proton and nitrogen polarization in ammonia and a
        test of equal spin temperature". In: *Nuclear Instruments and Methods in Physics Research Sec-
        tion A: Accelerators, Spectrometers, Detectors and Associated Equipment* 419.1 (1998), pp. 60 –82.
        issn: 0168-9002. doi: `http://dx.doi.org/10.1016/S0168-9002(98)00916-4`. url:
        `http://www.sciencedirect.com/science/article/pii/S0168900298009164`
        (cit. on pp. 41, 49).

[93]   Alexander Berlin. "Polarized solid ammonia targets for the COMPASS experiment
        at CERN". PhD thesis. Ruhr-University Bochum, Germany, 2016 (cit. on p. 42).

[94]   F Pobell. *Matter and Methods at Low Temperatures; 3rd ed.* Heidelberg: Springer, 2007. url:
        `https://cds.cern.ch/record/1019734` (cit. on p. 44).

[95]   H Preston-Thomas. "The International Temperature Scale of 1990 (ITS-90)". In:
        Metrologia 27.1 (1990), p. 3. url: `http://stacks.iop.org/0026-1394/27/i=1/a=`
        `002` (cit. on p. 44).

[96]   N. Doshita et al. "Performance of the COMPASS polarized target dilution refriger-
        ator". In: *Nuclear Instruments and Methods in Physics Research Section A: Accelerators, Spec-
        trometers, Detectors and Associated Equipment* 526.1 (2004). Proceedings of the ninth Inter-
        national Workshop on Polarized Solid Targets and Techniques, pp. 138 –143. issn:
        0168-9002. doi: `https://doi.org/10.1016/j.nima.2004.03.164`. url: `http:`
        `//www.sciencedirect.com/science/article/pii/S0168900204005753` (cit. on
        p. 45).

[97]   J. Koivuniemi *et al.* "Longitudinal polarization 2011". In: *COMPASS note* (2013). url:
        `http://wwwcompass.cern.ch/compass/notes/2013-7/2013-7.pdf` (cit. on
        p. 51).

[98]   D. Adams *et al.* "The polarized double cell target of the SMC". In: *Nucl. Instr. Meth.*
        Phys. Res. A 437.1 (1999), pp. 23 –67. issn: 0168-9002. doi: `http://dx.doi.org/10.`
        `1016/S0168-9002(99)00582-3`. url: `http://www.sciencedirect.com/science/`
        `article/pii/S0168900299005823` (cit. on p. 57).

[99]   N Doshita *et al.* "The COMPASS Polarized Target in 2006 and 2007". In: *AIP Con-*
        ference Proceedings 980.1 (2008), pp. 307–311. doi: `10.1063/1.2888101` (cit. on p. 57).

[100]   H. Matsuda. "Measurement of longitudial double spin asymmetries in the single-
        inclusive hadron quansi-real photoproduction at high-p_T by a muon beam for the
        study of gluon polarisation in nucleon". Ph.D. thesis. Yamagata University, Mar. 31,
        2016 (cit. on p. 59).

[101]   Susanne Koblitz. "Determination of the gluon polarisation from open charm pro-
        duction at COMPASS". PhD thesis. Mainz U., 2009. url: `http://ubm.opus.hbz-`
        `nrw.de/volltexte/2009/1943/` (cit. on p. 59).

[102]   Ilya Narsky and Frank C. Porter. Berlin: Wiley-VCH, 2013, p. 49. 459 pp. isbn: 978-
        3-527-41086-6. url: `http://www.hep.caltech.edu/~NarskyPorter/` (visited on
        12/18/2017) (cit. on p. 63).

[103]   B. Alessandro et al. "J/ψ and ψ' production and their normal nuclear absorption in
        proton-nucleus collisions at 400 GeV". In: *The European Physical Journal C - Particles and*
        Fields 48.2 (2006), pp. 329–341. issn: 1434-6052. doi: `10.1140/epjc/s10052-006-`
        `0079-4`. url: `https://doi.org/10.1140/epjc/s10052-006-0079-4` (cit. on
        pp. 66, 67).

[104]   Christopher Ralph Regali. "Exclusive event generation for the COMPASS-II experiment at CERN and improvements for the Monte-Carlo chain". PhD thesis. Albert-Ludwigs-Universität Freiburg, Physikalisches Institut, 2016 (cit. on p. 66).

[105]   Tobias Christian Szameitat. "New Geant4-based Monte Carlo Software for the COMPASS-II Experiment at CERN". PhD thesis. Albert-Ludwigs-Universität Freiburg, Physikalisches Institut, 2016 (cit. on p. 66).

[106]   S. Agostinelli et al. "GEANT4: A Simulation toolkit". In: *Nucl. Instrum. Meth.* A506 (2003), pp. 250–303. doi: `10.1016/S0168-9002(03)01368-8` (cit. on p. 66).

[107]   Torbjörn Sjöstrand, Stephen Mrenna, and Peter Skands. "PYTHIA 6.4 physics and manual". In: *Journal of High Energy Physics* 2006.05 (2006), p. 026. url: `http://stacks.iop.org/1126-6708/2006/i=05/a=026` (cit. on p. 66).

[108]   Torbjörn Sjöstrand, Stephen Mrenna, and Peter Skands. "A brief introduction to PYTHIA 8.1". In: *Computer Physics Communications* 178.11 (2008), pp. 852 –867. issn: 0010-4655. doi: `10.1016/j.cpc.2008.01.036`. url: `http://www.sciencedirect.com/science/article/pii/S0010465508000441` (cit. on p. 66).

[109]   Torbjörn Sjöstrand et al. "An introduction to PYTHIA 8.2". In: *Computer Physics Communications* 191.Supplement C (2015), pp. 159 –177. issn: 0010-4655. doi: `10.1016/j.cpc.2015.01.024`. url: `http://www.sciencedirect.com/science/article/pii/S0010465515000442` (cit. on p. 66).

[110]   M. R. Whalley, D. Bourilkov, and R. C. Group. "The Les Houches accord PDFs (LHAPDF) and LHAGLUE". In: *HERA and the LHC: A Workshop on the implications of HERA for LHC physics. Proceedings, Part B*. 2005, pp. 575–581. arXiv: `hep-ph/0508110 [hep-ph]` (cit. on p. 66).

[111]   M. R. Whalley, D. Bourilkov, and R. C. Group. *LHAPDF*. 2013. url: `http://lhapdf.hepforge.org` (visited on 10/19/2017) (cit. on p. 66).

[112]   M. Glück, E. Reya, and A. Vogt. "Pionic parton distributions". In: *Zeitschrift für Physik C Particles and Fields* 53.4 (1992), pp. 651–655. issn: 1431-5858. doi: `10.1007/BF01559743`. url: `https://doi.org/10.1007/BF01559743` (cit. on p. 70).

[113]   M. Glück, E. Reya, and A. Vogt. "Dynamical parton distributions revisited". In: *The European Physical Journal C - Particles and Fields* 5.3 (1998), pp. 461–470. issn: 1434-6052. doi: `10.1007/s100529800978`. url: `https://doi.org/10.1007/s100529800978` (cit. on p. 70).

[114]   Radja Boughezal et al. "Color-singlet production at NNLO in MCFM". In: *The European Physical Journal C* 77.1 (2016), p. 7. issn: 1434-6052. doi: `10.1140/epjc/s10052-016-4558-y`. url: `https://doi.org/10.1140/epjc/s10052-016-4558-y` (cit. on p. 77).

[115]   Roger Barlow. "Extended maximum likelihood". In: *Nuclear Instruments and Methods in Physics Research Section A: Accelerators, Spectrometers, Detectors and Associated Equipment* 297.3 (1990), pp. 496 –506. issn: 0168-9002. doi: `10.1016/0168-9002(90)91334-8`. url: `http://www.sciencedirect.com/science/article/pii/0168900290913348` (cit. on p. 78).

[116]   C. Adolph et al. "Transverse spin effects in hadron-pair production from semi-inclusive deep inelastic scattering". In: *Physics Letters B* 713.1 (2012), pp. 10 –16. issn: 0370-2693. doi: `10.1016/j.physletb.2012.05.015`. url: `https://www.sciencedirect.com/science/article/pii/S0370269312005321` (cit. on p. 78).

[117]   A. N. Sissakian et al. "Polarization effects in Drell-Yan processes". In: *Physics of Particles and Nuclei* 41.1 (2010), pp. 64–100. issn: 1531-8559. doi: 10.1134/S1063779610010041. url: https://doi.org/10.1134/S1063779610010041 (cit. on pp. 97, 99).

Acknowledgements

List of Figures

List of Tables